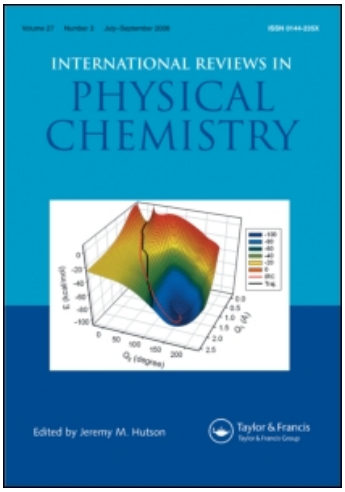

International Reviews in Physical Chemistry
Publication details, including instructions for authors and subscription information:
http://www.informaworld.com/smpp/title~content=t713724383

State-to-state dynamics of elementary chemical reactions using Rydberg H-atom translational spectroscopy

Xueming Yang[a]
[a] State Key Laboratory of Molecular Reaction Dynamics, Dalian Institute of Chemical Physics, Chinese Academy of Sciences, Dalian, P. R. China

To cite this Article Yang, Xueming(2005) 'State-to-state dynamics of elementary chemical reactions using Rydberg H-atom translational spectroscopy', International Reviews in Physical Chemistry, 24: 1, 37 — 98
To link to this Article: DOI: 10.1080/01442350500163806
URL: http://dx.doi.org/10.1080/01442350500163806

International Reviews in Physical Chemistry,
Vol. 24, No. 1, January–March 2005, 37–98

Taylor & Francis
Taylor & Francis Group

State-to-state dynamics of elementary chemical reactions using Rydberg H-atom translational spectroscopy

XUEMING YANG*

State Key Laboratory of Molecular Reaction Dynamics,
Dalian Institute of Chemical Physics, Chinese Academy of Sciences, Dalian, P. R. China

(*Received 10 February 2005; in final form 15 April 2005*)

In this review, a few examples of state-to-state dynamics studies of both unimolecular and bimolecular reactions using the H-atom Rydberg tagging TOF technique were presented. From the H_2O photodissociation at 157 nm, a direction dissociation example is provided, while photodissociation of H_2O at 121.6 has provided an excellent dynamical case of complicated, yet direct dissociation process through conical intersections. The studies of the $O(^1D) + H_2 \rightarrow OH + H$ reaction has also been reviewed here. A prototype example of state-to-state dynamics of pure insertion chemical reaction is provided. Effect of the reagent rotational excitation and the isotope effect on the dynamics of this reaction have also been investigated. The detailed mechanism for abstraction channel in this reaction has also been closely studied. The experimental investigations of the simplest chemical reaction, the H_3 system, have also been described here. Through extensive collaborations between theory and experiment, the mechanism for forward scattering product at high collision energies for the H + HD reaction was clarified, which is attributed to a slow down mechanism on the top of a quantized barrier transition state. Oscillations in the product quantum state resolved different cross sections have also been observed in the $H + D_2$ reaction, and were attributed to the interference of adiabatic transition state pathways from detailed theoretical analysis. The results reviewed here clearly show the significant advances we have made in the studies of the state-to-state molecular reaction dynamics.

Contents

*Email: xmyang@dicp.ac.cn

International Reviews in Physical Chemistry
ISSN 0144–235X print/ISSN 1366–591X online
http://www.tandf.co.uk/journals
DOI: 10.1080/01442350500163806

1. Introduction

Beam scattering techniques have been essential in the development of modern physics and chemistry. The modern atomic model developed by Rutherford based on alpha particle scattering experiments (figure 1) serves as an excellent example that beam scattering is a good tool to probe the structure and dynamics of the microscopic world. The development of the crossed beams scattering technique based on chemionization detection by Taylor and Datz half a century ago [1] opened the molecular beam era of chemistry research. The universal crossed molecular beams technique [2] developed in the 1960s by Lee, Herschbach *et al.* based on electron impact ionization have played a key role in crossed-beams scattering studies of the dynamics of fundamental chemical reactions. Important and fundamental information has been derived on primary reaction mechanisms, product angular distributions, partitioning of available energy in reactions between internal and translational energy of the product, as well as the dependence of the reaction cross-section on collision energy, impact parameter and reactant orientation [3–6]. Despite the success of universal electron impact ionization detection in studies of molecular reaction dynamics, the electron bombardment ionization technique does have serious disadvantages, such as its limited time-of-flight (TOF) resolution (~4% in time-of-flight) and its low detection sensitivity ($\sim 10^{-4}$).

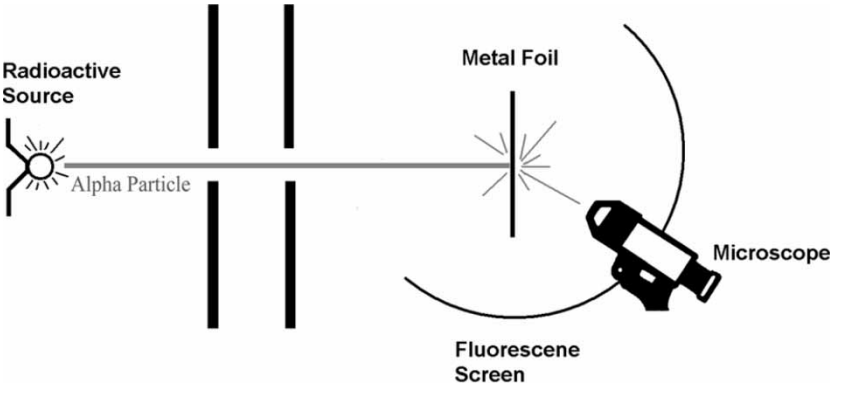

Figure 1. The alpha particle beam scattering experiment that led to the development of the modern atomic model by Rutherford.

These limitations prevent us from looking into the full quantum state-resolved scattering dynamics of many important elementary chemical reactions.

During the last decade or so, new experimental techniques, such as the ion-imaging technique [7, 8], the H-atom Rydberg tagging method [9] and the Doppler-selected time-of-flight method [10], for molecular beam scattering measurements, have allowed us to study the chemical reaction dynamics in unprecedented detail. Accurate measurements of the state-resolved scattering quantities for elementary chemical reactions are becoming feasible. The development of the Rydberg H-atom translational spectroscopy technique has provided us with an extremely powerful tool for measuring the state-resolved differential cross-sections for both unimolecular and bimolecular reactions with unprecedented translational energy resolution and extremely high sensitivity. This technique has been applied successfully to studies of the important benchmark reaction $H + D_2 \rightarrow HD + H$ recently [11] and many important unimolecular dissociation processes [12]. Recent studies in our laboratory on H_2O photochemistry [13], the $O(^1D) + H_2$ reaction [14] and the $OH + D_2$ reaction [15] using this technique have further demonstrated the power of this method in obtaining experimentally the most detailed dynamics of these benchmark systems. These state-of-the-art experimental studies, coupled with the recent advances in theoretical state-to-state dynamics studies, can now provide an in-depth physical understanding of elementary chemical reactions that could not be imagined before.

In this article, we will review the most recent advances made in our laboratory on the unimolecular dissociation of the important H_2O molecule as well as the bimolecular reactions, $O(^1D) + H_2 \rightarrow OH + H$ and $H + HD \rightarrow H_2 + D$, using the Rydberg H-atom translational spectroscopy technique.

2. The Rydberg H-Atom translational spectroscopy technique

The Rydberg H-atom translational spectroscopy technique was developed in the early 1990s by Welge and coworkers [9]. This technique has been successfully applied to investigate photodissociation dynamics of many important species [12],

as well as the simplest chemical reaction, $H + D_2 \rightarrow HD + H$ [11]. The key element of this technique is the two-step efficient excitation (see figure 2) of the H-atom from its ground state to its high Rydberg levels ($n = 35 \sim 90$) without ionizing the H-atom product directly as in the $(1 + 1')$ multiphoton ionization scheme used earlier. Figure 3 shows the spectrum of Rydberg transitions of the H atom from the $n = 2$ level. These high-Rydberg H-atoms are known to be long-lived on millisecond time-scales in a small electric field ($\sim$20 V/cm). The enhancement of Rydberg H-atom lifetime in a small electric field is likely caused by the mixing of the l quantum number in the Rydberg H-atom [16, 17]. These long-lived neutral H atoms allow us to measure the time-of-flight spectrum of the neutral H-atom chemical product with extremely high translational energy resolution (as high as 0.1% in translational energy has been achieved in our laboratory). The neutral Rydberg H-atoms are easy to detect using field ionization. The extremely high

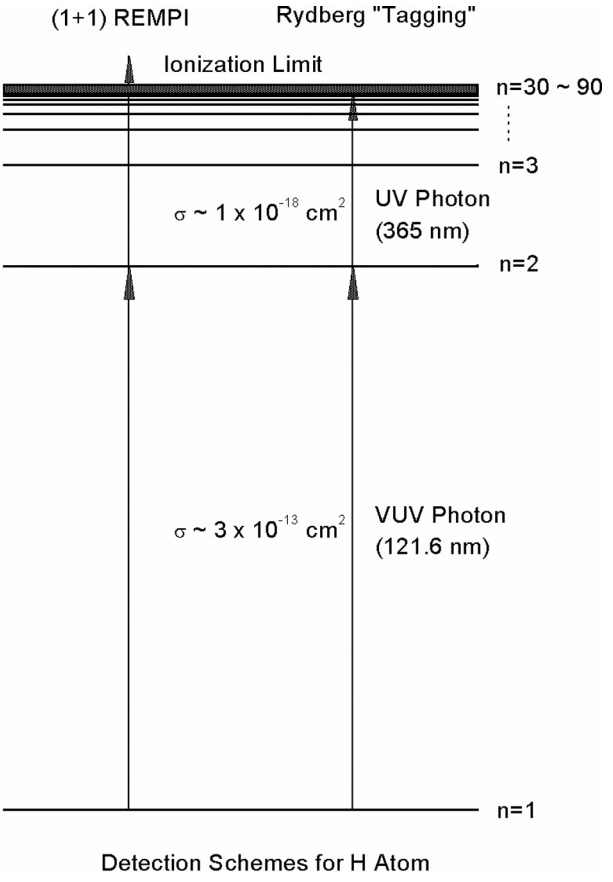

Figure 2. Detection schemes for H atoms. Rydberg 'tagging' technique is slightly different from the $(1 + 1')$ REMPI detection scheme in which H atom is directly ionized, while Rydberg 'tagging' only pumps the H atom to a high Rydberg state.

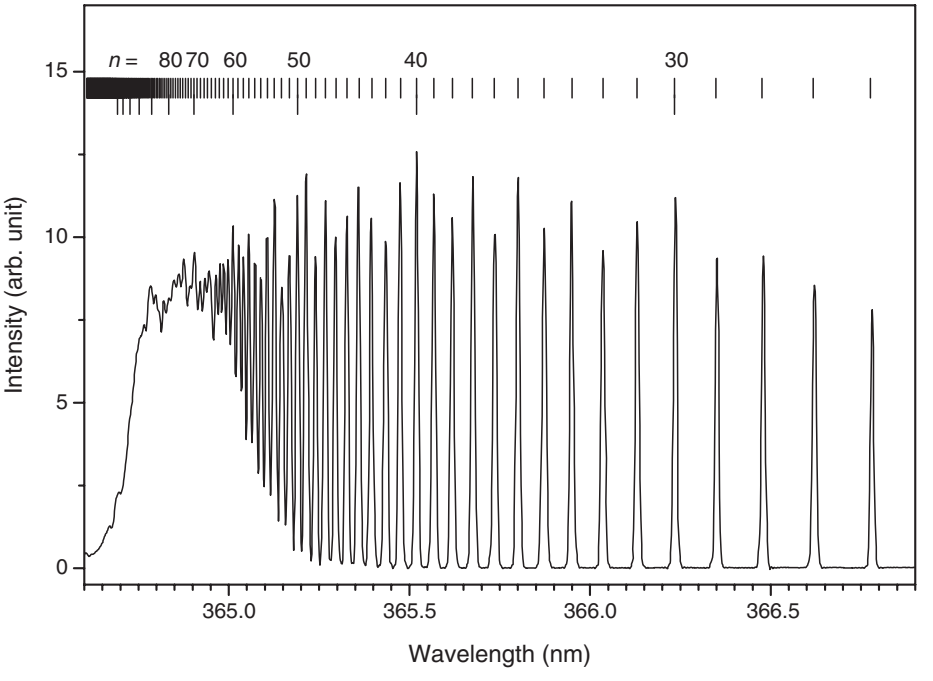

Figure 3. The H-atom Rydberg transition spectrum from the $n=2$ level to the higher n states.

translational energy resolution can be achieved by minimizing the physical sizes of the tagging region and the field ionization region.

The excitation of the ground state H-atom product ($n=1$) is made by the following two-step excitation scheme:

$$\mathrm{H}(n=1) + h\nu\ (121.6\,\mathrm{nm}) \rightarrow \mathrm{H}(n=2)$$

and

$$\mathrm{H}(n=2) + h\nu\ (365\,\mathrm{nm}) \rightarrow \mathrm{H}^{*}(n \sim 50)$$

The 121.6 nm VUV light used in the first step excitation is generated using a two-photon resonant ($2\omega_1 - \omega_2$) four wave mixing scheme in the Kr gas cell. $2\omega_1$ (212.5 nm) is resonant with the Kr (4p–5p) transition [18]. ω_1 is generated by doubling a dye laser pumped by a Nd:YAG (355 nm) laser, while ω_2 (845 nm) is the direct output of a dye laser pumped by the second harmonic of the same YAG laser. During the experiment, a few mJ of 212.5 and 845 nm laser light are generally used. By generating about 50 μJ of the 121.6 nm laser light, the first step can be easily saturated since this transition has a huge excitation cross-section ($3.0 \times 10^{-13}\,\mathrm{cm}^2$). Following the first step VUV excitation, the H-atom product is then sequentially excited to a high Rydberg state with $n \approx 50$ using 365 nm light in near saturation, which is generated by doubling a dye laser pumped by the same

YAG laser. This excitation scheme allows us to pump the H atom to a high Rydberg state in nearly unit efficiency. These two excitation laser pulses have to be overlapped exactly both in space and time. The neutral Rydberg H atom then flies a certain TOF distance to reach a multi-channel plate (MCP) detector with a fine metal grid (grounded) in the front. After passing through the grid, the Rydberg tagged H-atom products are then immediately field-ionized by the electric field applied between the front plate of the Z-stack MCP detector and the fine metal grid. The signal detected by the MCP is then amplified by a fast pre-amplifier, and counted by a multichannel scaler.

Two types of experiments, photodissociation (H_2O) and crossed beam bimolecular reactions ($O(^1D) + H_2(HD, D_2) \rightarrow OH(OD) + H(D)$ and $H + HD(D_2) \rightarrow H_2$ $(HD) + D$), have been carried out using the experimental technique described above in our laboratory. In the following sections, we will review the results on these systems.

3. Photochemistry of H_2O: direct dynamics versus conical intersection dynamics

Photodissociation of the water molecule is a model system for both experimental and theoretical studies. Extensive experimental and theoretical studies have been carried on this system during the last few decades. Excitation in its longest wavelength ultraviolet absorption band around 150–200 nm leads to the lowest excited singlet state ($\tilde{A}^1B_1$). Dissociation from this state proceeds on a single potential energy surface leading to an H atom and a ground state $OH(X^2\Pi)$ molecular product with little internal excitation [19]. This is a prototypical example of direct dissociation. In contrast, three electronic states of the water molecule are implicated in its photochemistry at the Lyman-α wavelength (121.6 nm) [20–22]. The initial excitation of H_2O at the Lyman-α wavelength is to the third singlet electronic state ($\tilde{B}^1A_1$), which correlates adiabatically with an H atom and an excited electronic state of the OH partner ($A^2\Sigma^+$). However, although OH radicals in the A-state are produced [23], the dominant dissociation leads to an H atom plus a rovibrationally excited ground state OH molecule via non-adiabatic crossing from the $\tilde{B}^1A_1$ state to the potential energy surfaces of either the $\tilde{A}$ state or the ground state of water ($\tilde{X}^1A_1$). Even though extensive information on photodissociation through the $\tilde{B}^1A_1$ state has been obtained through these studies [24, 25], a quantitative picture of H_2O dissociation from this surface is still lacking.

Conical intersections of potential energy surfaces have been recognized as playing an important role in the dynamics of excited electronic state photochemistry and chemical reactions. H_2O $\tilde{B}^1A_1$ state photochemistry is a well-known example. One of the notable observations from previous experimental studies is the extremely high rotational excitation of the OH product. This is attributed to a conical intersection at a collinear (H–O–H) geometry. Dynamical calculations have shown that the high average rotational angular momentum of the OH product is a consequence of the high torque acting in the vicinity of this conical intersection of the excited and ground state potential energy surfaces. This conical intersection arises because a linear approach of H to OH on the repulsive potential curve from $H + OH(X^2\Pi)$ can

cross an attractive potential curve from $H + OH(A^2\Sigma^+)$, whereas there is an avoided crossing of these curves in the lower symmetry of a bent geometry.

In addition to this well-known conical intersection for the H–O–H geometry, there is a second symmetry-determined conical intersection on the $\tilde{B}^1A_1$ state for the collinear O–H–H geometry. The importance of this second conical intersection in the $O(^1D, ^3P) + H_2$ reaction system has been noted before [26]. However, only very recently has its possible influence on the photodissociation of H_2O been seriously addressed. Mordaunt *et al.* pointed out [27], in a recent wavepacket calculation, that a small part of the dissociative flux on the $\tilde{B}^1A_1$ surface goes toward the second conical intersection (O–H–H), thus indicating that this second intersection might also play a role in the $\tilde{B}$-state photodissociation. Following various improvements in the experiments, many features of the photofragment translational spectra have been more clearly revealed in an even more fine tuned experimental investigation of the H_2O photodissociation at 121.6 nm in our laboratory.

In the photodissociation experiments described here, dissociation dynamics of H_2O at two photolysis wavelengths (157 nm and 121.6 nm) were studied. At 157 nm excitation, H_2O is excited to the $\tilde{A}^1B_1$ surface; while at 121.6 nm, H_2O is excited to the $\tilde{B}^1A_1$ surface. The experimental set-up used to study the H_2O photodissociation is described by the simple schematic shown in figure 4. A fluorine laser (Lambda Physik) is used as the photolysis laser source for the photodissociation of H_2O at 157 nm; while the same laser to pump the H-atom Lyman-α transition is also used as the photolysis laser for the 121.6 nm photodissociation. The 157 nm laser light is unpolarized, while the 121.6 nm laser light is polarized. The polarization direction of the 121.6 nm photolysis light can be changed by rotating the polarization of the 845 nm laser using a rotatable half-waveplate for product angular anisotropy measurement. In the H_2O photodissociation, a molecular beam of H_2O was generated by expanding a mixture of H_2O and Ar (~3%) at a stagnation pressure of 600 torr through a 0.5 mm diameter pulsed nozzle. The mixture of H_2O and Ar was made by bubbling Ar through the water sample at room temperature. The rotational temperature of the H_2O molecules in the molecular beam is about ~10 K. The detector in the photodissociation experiment is fixed in the perpendicular direction of the molecular beam. The molecular beam and the photolysis laser beam are all perpendicular to each other.

In this section, we will describe the results of our recent study of the water photo dissociation at both 157 and 121.6 nm in our laboratory, providing further insights into the detailed dynamics of this interesting and fundamentally important system.

3.1. *H_2O photochemistry via the $\tilde{A}\,^1B_1$ surface: direct dissociation*

Photodissociation of H_2O on the $\tilde{A}^1B_1$ surface has recently been studied at 157 nm using the HRTOF technique described above in our laboratory [28]. The time-of-flight spectrum of the H-atom product from the H_2O photodissociation at 157 nm was measured. The experimental TOF spectrum is then converted into the total product translational distribution of the photodissociation products. Figure 5 shows the total product translational energy spectrum of H_2O photodissociation at 157.6 nm in the molecular beam (with rotational temperature 10 K or less). Five vibrational features

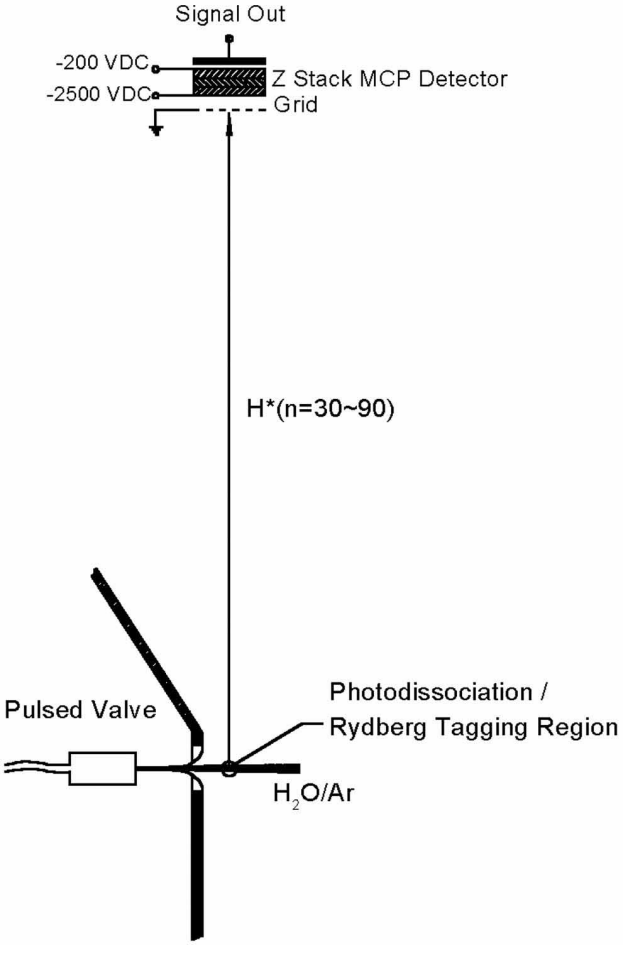

Figure 4. Experimental set-up for H_2O photodissociation.

have been observed in this spectrum, which can be easily assigned to the vibrational excited OH ($v = 0, 1, 2, 3, 4$) products from the photodissociation of H_2O at 157.6 nm. In the experiment under molecular beam conditions, rotational structure with larger N quantum numbers are partially resolved. By integrating the whole area of each vibrational manifold, the OH vibrational state distribution from the H_2O sample at 10 K can be obtained. In order to get an estimate of the rotational excitation of the OH product, the product translational energy distribution is simulated using fixed parameters. The translational energy distribution for H_2O photodissociation in figure 5 has been simulated. From the simulation, it is clear that the rotational excitation of the OH products in the $v = 0$, 1, 2, 3 states is quite cold, with an estimated rotational temperature of about 340 K. Interestingly, the rotational temperature of the OH products in the $v = 4$ state is notably higher than that in the lower vibrational states. The estimated rotational temperature for OH ($v = 4$) is about 650 K. These results are similar to that obtained by Andresen *et al.* [29] using the laser induced fluorescence (LIF) technique.

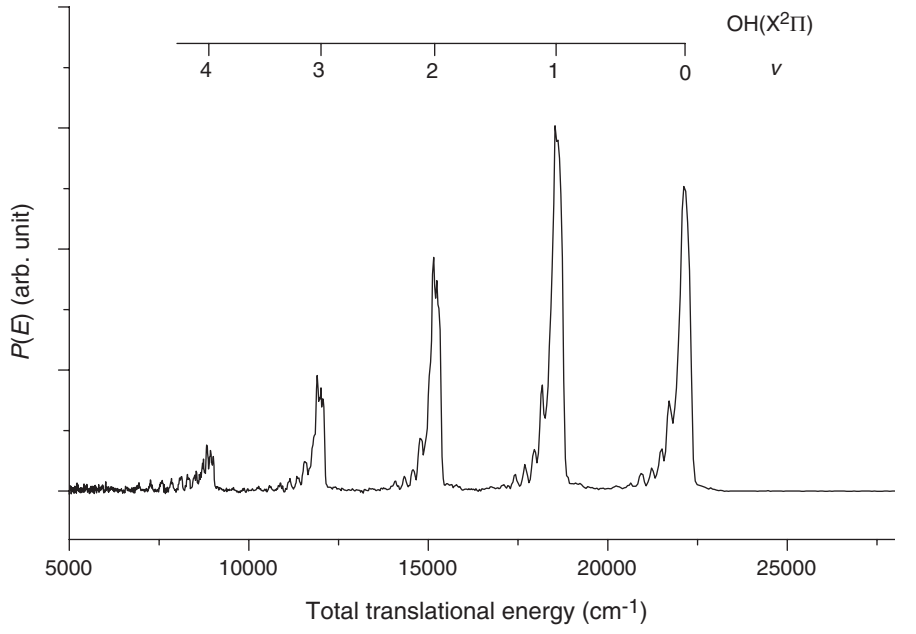

Figure 5. The total translational energy distribution of H_2O photodissociation at 157 nm. The peaks correspond to the different rovibrationally excited OH products.

In order to see the effect of the rotational excitation of the parent H_2O molecules on the OH vibrational state distribution, the experimental TOF spectrum of the H-atom from photodissociation of a room temperature vapour H_2O sample has also been measured with longer flight distance (~78 cm). By integrating each individual peak in the translational energy spectrum, the OH product vibrational distribution from H_2O photodissociation at room temperature can be determined.

The OH product vibrational state distributions obtained from the above experimental studies are listed in table 1. From the results obtained under the two extreme conditions (molecular beam and room temperature vapour) in this work, it is clear that the rotational excitation of the parent molecule has a negligible effect on the product vibrational state distribution of the OH product from H_2O photodissociation at 157.6 nm excitation. Previous experimental and theoretical results are also shown in table 1.

From table 1, it is quite obvious that the OH product vibrational state distribution obtained in our laboratory is significantly different from that measured using the LIF method [29, 30] especially in the higher vibrational states. This implies that the vibrational distribution of OH obtained by previous LIF measurements may have serious errors. This conclusion may have a significant impact since LIF has been widely used in measuring the product OH vibrational state distribution in studies of many important chemical reactions. The vibrational distributions obtained here for high vibrational states are as much as 50 times larger than that obtained by the LIF technique. These results indicate that one must be very careful when using LIF to measure vibrational distributions of the OH product. Generally speaking, LIF is a sensitive

Table 1. Vibrational state distribution of OH/OD from H_2O/D_2O/DOH photodissociation at 157.6 nm.

	v							
Species	0	1	2	3	4	5	6	Remark
H_2O	1.0	1.11	0.61	0.30	0.15	0	0	Beam[a]
H_2O	1.0	1.06	0.56	0.24	0.11	0	0	Vapour[a]
H_2O	1.0	1.03	0.57	0.27	0.11	0	0	EI [b]
H_2O	1.0	0.96	0.15	–	–	–	–	Exp. [29]
H_2O	1.0	0.56	0.10	0.02	0.003	$< 3 \times 10^{-4}$	–	Exp. [30]
H_2O	1.0	0.89	0.63	0.41	0.28	0.24	–	Theory [31]
H_2O	1.0	0.81	0.53	0.34	0.18	0.10	–	Theory [32]
H_2O	1.0	1.06	0.59	0.27	0.13	0.01	0.00	Theory [33]
D_2O	1.0	1.49	1.09	0.67	0.39	0.16	0.03	Beam[a]
D_2O	1.0	1.39	1.00	0.49	0.29	0.14	0.01	Theory [33]
DOH/OH	1.0	1.56	1.02	0.60	0.13	0	0	Beam[a]
DOH/OH	1.0	1.18	0.73	0.46	0.09	0	0	Theory [33]
DOH/OD	1.0	1.19	0.76	0.45	0.29	0.16	0.09	Beam[a]
DOH/OD	1.0	1.08	0.56	0.29	0.15	0.09	0.03	Theory [33]

[a] These results are obtained in this work using the H-atom Rydberg tagging TOF technique.
[b] These results are obtained in this work using a universal electron impact ionization detector.

detection technique for molecular species. However, there are a few problems involved when one uses this technique to measure relative product vibrational populations. Firstly, in order to determine the relative population distributions in many vibrational states, one normally could not cover all vibrational states within the tuning range of one laser dye. This would likely cause propagation errors in measuring the relative LIF signals from different OH vibrational states. Secondly, saturation effects may also cause significant errors when one calculates relative populations using relative LIF intensities. When converting relative LIF intensities to relative populations, one usually needs information that is not readily available, such as transition dipole moments, etc. If one uses transitions with small off-diagonal Franck–Condon (FC) factors, by which many previous LIF measurements of OH were carried out, errors in the calibration might originate from the inaccuracy of the small off-diagonal FC factors which are harder to calculate accurately. Furthermore the inaccuracy of the vibrational overlap integrals will also make the estimation of the transition dipole much more difficult since an accurate r-centroid is even harder to obtain for each transition. Predissociation of OH in the excited electronic state in the LIF scheme can also cause serious problems; and it is well known that OH predissociates in the $A^2\Sigma$ state. This could also be a major source of errors in measuring the vibrational distribution of OH because the effect of predissociation is hard to account for quantitatively in many cases.

From table 1, it is clear that vibrational state distributions of the OH product obtained here under the two experimental conditions in our work are in rather good agreement with the theoretical results, indicating that the overall accuracy of the theoretical calculations is fairly good for the $v \leq 4$ levels. There is, however, a large discrepancy between the previous theoretical results [31, 32] and our experimental measurement at $v = 5$. In fact, no signal has been observed for the OH products

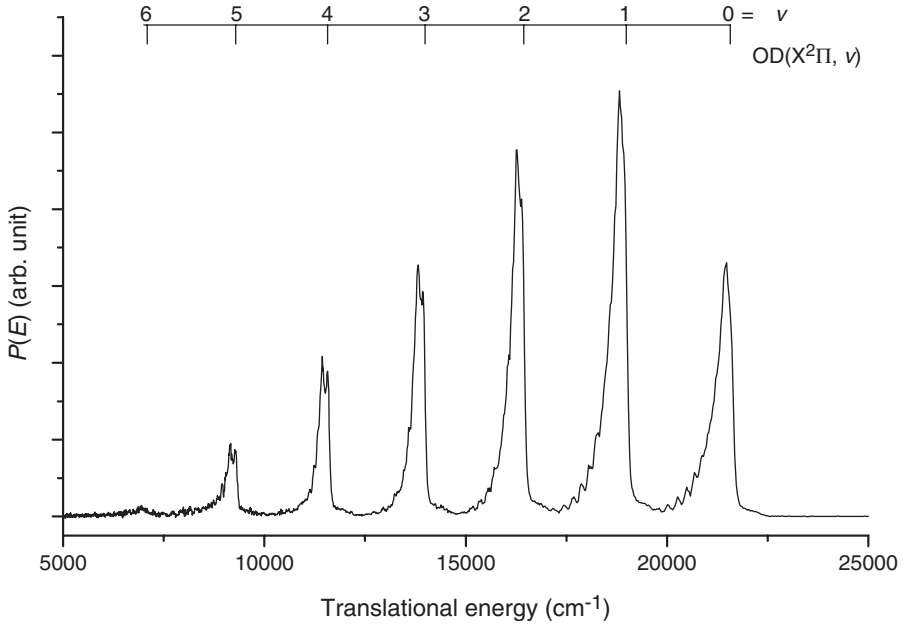

Figure 6. The total translational energy distribution of D_2O photodissociation at 157 nm. The peaks correspond to the different rovibrationally excited OD products.

at $v = 5$ in our experiment. Since detection efficiencies for H-atoms with different velocities are uniform using the Rydberg tagging technique as we have demonstrated in the photodissociation of H_2O at 121.6 nm [34], the discrepancies between theory and experiment should come from the inaccuracies of the H_2O $\tilde{A}$ state potential energy surface on which all previous theoretical calculations are based. Improvement on the theoretical calculations should also be possible using a more accurate $\tilde{A}$ state potential energy surface. Recent theoretical studies based on an improved potential energy surface (PES) [33] have shown that this is truly the case. The agreement between theory and experiment is much improved for H_2O with the improved PES. This improved $\tilde{A}$ state potential energy surface is now believed to be one of the most accurate model potentials for direct dissociation processes in tri-atom molecules.

Photodissociation of D_2O on the $\tilde{A}$ surface at 157 nm has also been investigated. The time-of-flight spectrum of the D atom product from the D_2O photodissociation was measured using the Rydberg tagging TOF technique. The experimental TOF spectrum is then converted into the total translational distribution of the photodissociation products. Figure 6 shows the total product translational energy spectrum of D_2O photodissociation at 157.6 nm in a molecular beam. Seven vibrational features have been observed in the spectrum. These features can be easily assigned to the vibrational excited OD products for $v = 0$–6 from the photodissociation of D_2O at 157.6 nm. Because of the smaller OD rotational constant, the rotational structures are not as well resolved as in the H_2O case. By integrating the whole area of each vibrational manifold, the OD vibrational state distribution from a D_2O beam sample at 10 K

can be obtained. The relative distribution obtained is also listed in table 1 with the HOD photodissociation results. It is quite clear that the rotational excitation of the OD products is also quite cold for different OD vibrationally excited products. It is interesting to point out that even though more vibrational states of the OD product in the D_2O photodissociation are populated in comparison with the OH product from H_2O photodissociation, the vibrational energy deposited into the OD product is quite similar to the OH product. The averaged vibrational energy deposited in the OH product from H_2O is about 4170 cm^{-1}, while that deposited in the OD product from D_2O is about 4310 cm^{-1}.

Photodissociation of HOD on the $\tilde{A}^1B_1$ surface at 157 nm in the molecular beam has also been studied using the Rydberg tagging technique. Since a pure sample of HOD could not be obtained practically because of the fast H/D exchange rate, a sample of 1 : 1 mixture of H_2O and D_2O is prepared in order to obtain the HOD sample. Due to the fast exchange of the H and D atoms in this water sample, the final mixed ratio of the three isotopomers, H_2O, HOD and D_2O, should be 1 : 2 : 1, respectively, after reaching equilibrium. Therefore, in the photodissociation of this mixed sample, there will be two different sources for the H-atom: one from the H_2O molecule, and the other from the HOD molecule. Similarly, there will also be two different sources for the D-atom: one from the D_2O molecule, and the other from the HOD molecule. The time-of-flight spectrum of both H-atom product (with OD partner product) and D-atom product (with OH partner product) from the mixed water sample has to be measured in order to acquire the whole picture of the HOD photodissociation. Figure 7(a) shows this translational energy distribution for the H detection from the mixed sample. In order to show the contribution from the H_2O photodissociation, figure 7(b) presents the translational energy distribution for pure H_2O photodissociation converted from the H-atom TOF spectrum using a mass ratio of 1 : 18. From this figure, one can see immediately the contribution from HOD photodissociation (H-atom product). It is quite obvious that a total of seven vibrational states ($v = 0$–6) in the OD product from the HOD photodissociation have been observed. By integrating each individual peak and subtracting the contribution from H_2O, the OD product vibrational state distribution from HOD photodissociation can be determined. The results obtained are listed in table 1.

Similarly, the TOF spectrum of the D-atom product from the mixed sample has also been measured. Figure 8(a) shows the translational energy distribution for D product from the mixed sample. In order to show the contribution from the D_2O photodissociation, figure 8(b) also shows the translational energy distribution for the photodissociation of the pure D_2O sample converted from the D-atom TOF spectrum using a mass ratio of 2 : 17. A total of five vibrational states ($v = 0$–4) in the OH product from HOD photodissociation have been observed. By integrating each individual peak and subtracting the contribution from D_2O, the OH product vibrational state distribution for the HOD photodissociation can be experimentally determined. The results obtained are listed in table 1.

The OD vibrational distribution from the HOD photodissociation resembles that from the D_2O photodissociation. Similarly, the OH vibrational distribution from the HOD photodissociation is similar to that from the H_2O photodissociation. There are, however, notable differences for the OD products from HOD and D_2O, similarly

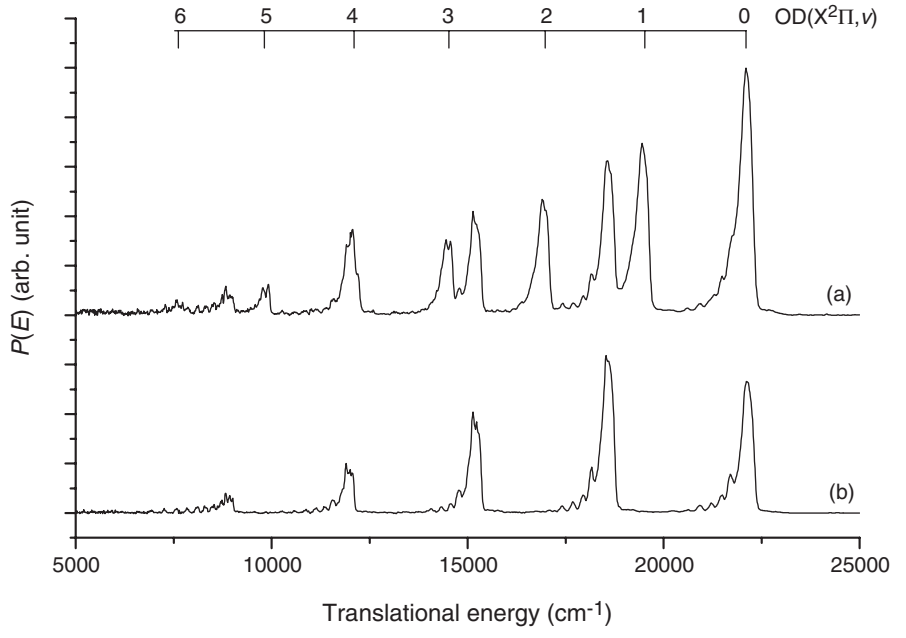

Figure 7. (a) The total translational energy distribution of the H atom product from the mixed sample using 1 : 18 mass ratio. (b) The total translational energy distribution of the H atom product from pure H_2O sample using 1 : 18 mass ratio.

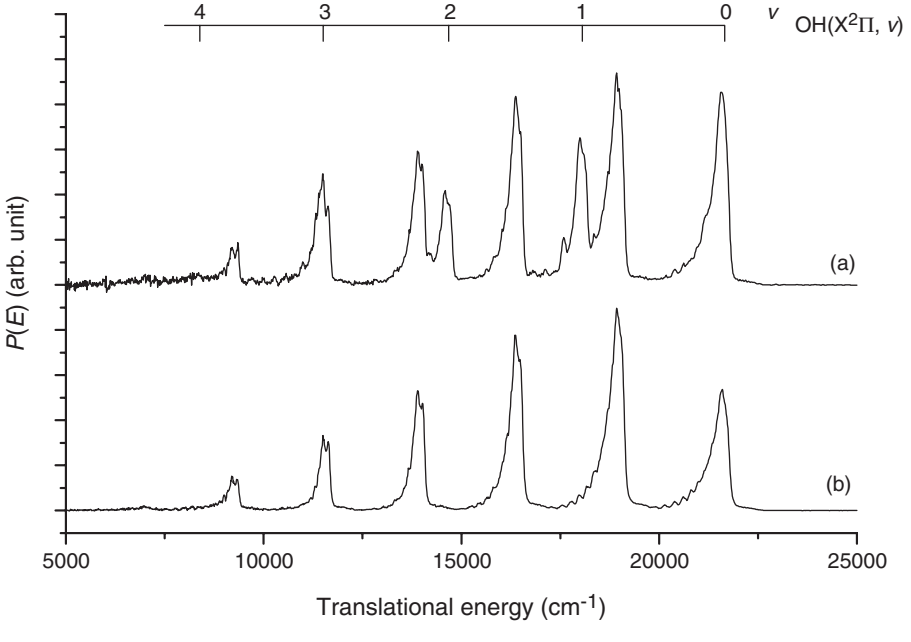

Figure 8. (a) The total translational energy distribution of the D-atom product channel from the mixed sample using 2 : 17 mass ratio. (b) The total translational energy distribution of the H-atom product from pure D_2O sample using 2 : 17 mass ratio.

for the OH products from HOD and H_2O. It is also clear that rotational temperatures are all quite cold for all OH (OD) products. From the above experimental results, the branching ratio of the H and D product channels from the HOD photodissociation can be estimated. The mixed sample of H_2O and D_2O with 1 : 1 ratio is known to go through isotope exchange quickly and reach its equilibrium with an exact ratio of H_2O, HOD and D_2O of 1 : 2 : 1. Because the absorption spectrum of H_2O at 157 nm is a broadband transition, we can reasonably assume that the absorption cross-sections are the same for the three water isotopomer molecules. It is also quite obvious that the quantum yield of these molecules at 157 nm excitation should be unity since the $\tilde{A}^1B_1$ surface is purely repulsive and is not coupled to any other electronic surfaces. From the above measurement of the H products from the mixed sample, the ratio of the H-atom products from HOD and H_2O is determined to be 1.27. If we assume the quantum yield for H_2O at 157 is unity, the quantum yield for the H production should be 0.64 (1.27 divided by 2) since the HOD concentration is twice that of H_2O in the mixed sample. Similarly, from the above measurement of the D-atom product from the mixed sample, we can actually determine the ratio of the D-atom products from HOD and D_2O to be 0.52. Using the same assumption that the quantum yield of the D_2O photodissociation at 157 nm is unity, the quantum yield of the D-atom production from the HOD photodissociation at 157 nm is determined to be 0.26. Therefore the total quantum yield for the H and D products from HOD is $0.64 + 0.26 = 0.90$. This is a little bit smaller ($\sim$10%) than 1 since the total quantum yield of the H and D productions from the HOD photodissociation should be unity because no other dissociation channel is present for the HOD photodissociation other than the H- and D-atom elimination processes. There are a few sources of error, however, in this estimation: (a) the assumption that the absorption cross-sections of all three water isotopomers at 157 nm are exactly the same, and (b) the accuracy of the volume mixture in the H_2O and D_2O mixed sample used in the experiment. For the absorption cross-sections, there are probably some small differences among the three isotopomers in reality. Nevertheless, this estimate should be quite reasonable. The estimated branching ratios of the H and D productions from HOD at 157 nm excitation should be 2.46 with about $\pm$15% estimated error bar. More accurate measurement on the branching ratio should be possible with the experimentally measured cross-section values for H_2O and D_2O.

3.2. *H_2O photochemistry via the $\tilde{B}^1A_1$ surface: conical intersection dynamics*

While dissociation of H_2O on the $\tilde{A}$ surface is clearly a prototypical direct dissociation process, dissociation of H_2O on the $\tilde{B}^1A_1$ surface is much more complicated. Three electronic states are involved in the photochemistry of H_2O at 121.6 nm. The initial excitation is to the third singlet state, $\tilde{B}^1A_1$, which correlates adiabatically with an H-atom and an excited electronic state of the OH partner (OH, $A^2\Sigma^+$). However, the dominant dissociation, to an H atom plus a ground state OH molecule (OH, $X^2\Pi$), is brought about by non-adiabatic crossings from the $\tilde{B}^1A_1$ state to the potential energy surfaces of either the $\tilde{A}^1B_1$ state or the $\tilde{X}^1A_1$ ground state of water. These are mediated respectively by electronic Coriolis interactions, and through conical intersections of the $\tilde{B}^1A_1$ and $\tilde{X}^1A_1$ surfaces.

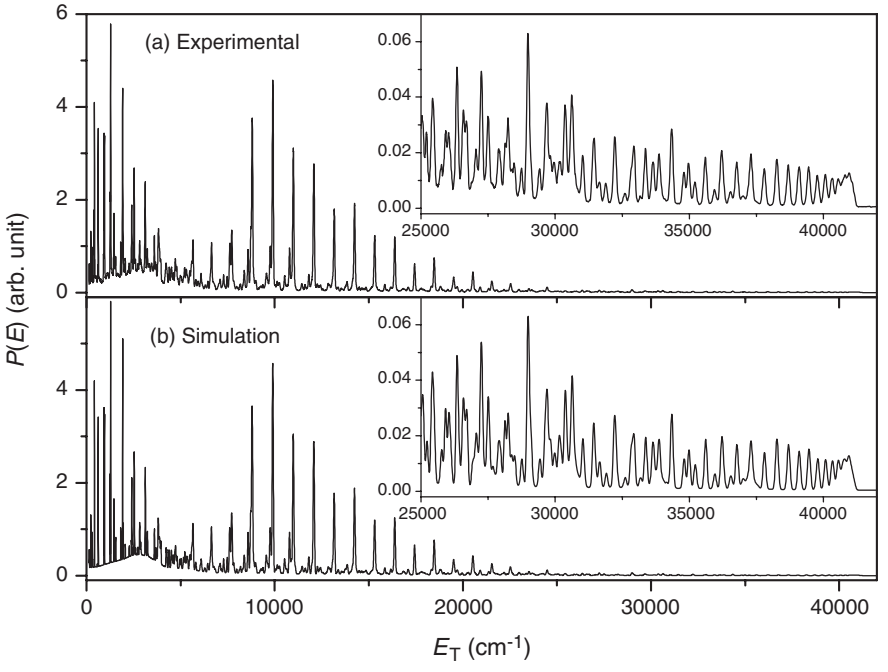

Figure 9. The translational energy distributions of H_2O photodissociation at 121 nm obtained with photolysis laser polarization parallel to the detection direction. (a) The upper trace was acquired experimentally. (b) The lower trace is the simulated distribution.

Experimentally, photodissociation of H_2O at 121.6 nm has been investigated [35] using the same experimental method used at 157 nm above except that the 157 nm laser is absent. Two TOF spectra were obtained with the photolysis laser polarization parallel and perpendicular to the detection axis. The two TOF spectra have been converted to the total translational energy distribution of the photodissociation process using a computer program that includes allowance for the velocity of the molecular beam. Figure 9(a) shows the experimental product translational energy distribution in the parallel direction, while figure 10(a) shows the experimental product translational energy distribution in the perpendicular directions.

From the translational energy distributions obtained above, the quantum state distributions and the quantum state-specific anisotropy parameters can be determined. In a molecular photodissociation process, the photodissociation product detected at an angle in the centre-of-mass frame of θ_{cm} relative to the photolysis laser polarization can be represented by the following formula:

$$\psi(E_T, \theta_{cm}) = \varphi(E_T)\,[1 + \beta(E_T)P_2(\cos\theta_{cm})] \tag{1}$$

where $\varphi(E_T)$ is the product translational energy distribution and $\beta(E_T)$ is the energy dependent anisotropy parameter. In order to determine both $\varphi(E_T)$ and $\beta(E_T)$ in the experiment, translational energy distributions at two polarizations (parallel and perpendicular to the detection axis) in the laboratory frame have to be measured.

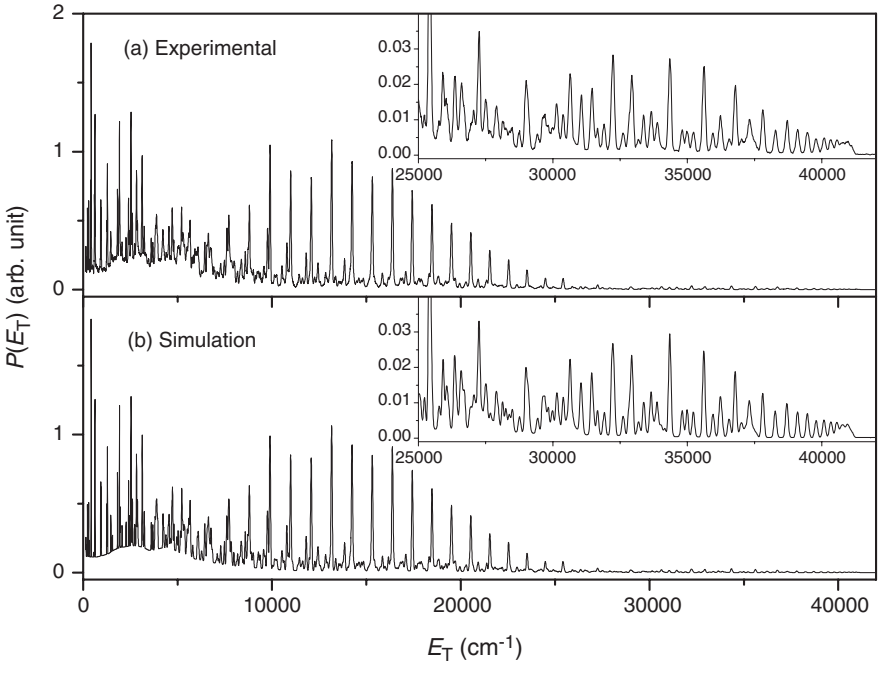

Figure 10. The translational energy distributions of H_2O photodissociation at 121 nm obtained with photolysis laser polarization perpendicular to the detection direction. (a) The upper trace was acquired experimentally. (b) The lower trace is the simulated distribution.

θ_{cm} is dependent on E_T, but can be calculated from θ_{lab} provided the beam velocity is known. $\sigma(E_T)$ and $\beta(E_T)$ can therefore be calculated by solving the following two equations, in which the angles for $\psi^{\perp}(E_T, \theta^{\perp}_{cm})$ and $\psi^{||}(E_T, \theta^{||}_{cm})$ have first been derived using a laboratory to centre-of-mass transformation,

$$\psi^{\perp}(E_T, \theta^{\perp}_{cm}) = \sigma(E_T)\,[1 + \beta(E_T)P_2(\cos\theta^{\perp}_{cm})] \tag{2}$$

$$\psi^{||}(E_T, \theta^{||}_{cm}) = \sigma(E_T)\,[1 + \beta(E_T)P_2(\cos\theta^{||}_{cm})] \tag{3}$$

Extensive sharp structures in the product translational energy distributions (figures 9a and 10a) have been observed. Since the H-atom product has no internal excitation, these sharp features all correspond to the electronically and rovibrationally excited OH products. OH quantum state distributions have been determined from the simulations of the product translational energy distributions obtained above for the two polarizations. Figures 9(b) and 10(b) show the simulated product translational energy distributions for the two corresponding polarizations (parallel and perpendicular). The energy resolution in the experiment varies with the translational energy of the H-atom product, so that the line-width of each peak in the simulation is a function of the translational energy. In addition to the OH(X) and OH(A) products, a broad underlying peak has also been observed at low translational energy. This underlying peak is also simulated using a broad energy distribution.

From the above simulations, rovibrational state distributions have been determined for both the OH(X) and OH(A) products.

3.2.1. OH product quantum state distributions. Assignments have been made for almost all the peaks in the translational energy spectra using the complete set of bound states of OH in its X and A states. In total, 10 vibrational states ($v = 0$–9) of OH(X) have been included in the fitting of the translational distributions. From the simulations, it is clear that the most important pathway leads to the OH ground electronic state products in the $v = 0$ state. Figure 11 shows the rotational distributions of the OH(X, $v = 0$) product obtained from the simulations. It is apparent that most of the OH(X, $v = 0$) products are extremely rotationally excited with a peak at $N = 45$, corresponding to about 32 000 cm^{-1} rotational excitation. This is an extreme case that almost 75% of the available energy is deposited into purely rotational excitation. It is also interesting to point out that the rotational distribution shows a clear oscillation around $N = 40$, with the odd N levels having enhanced population with respect to the neighbouring even N levels. There is also another oscillation in the weaker peaks of the rotational distribution near $N = 18$. Such oscillations have been traced to the dynamical interference arising from two conical intersection pathways on the excited surface [36].

Rotational state distributions for the OH(X) products for $v = 1$–4 have also been determined. These products are also highly rotationally excited, indicating that they are probably produced through the same dynamical pathway as the OH(X) $v = 0$ product. OH(X) products for $v = 5$–9 have also been observed. However, the

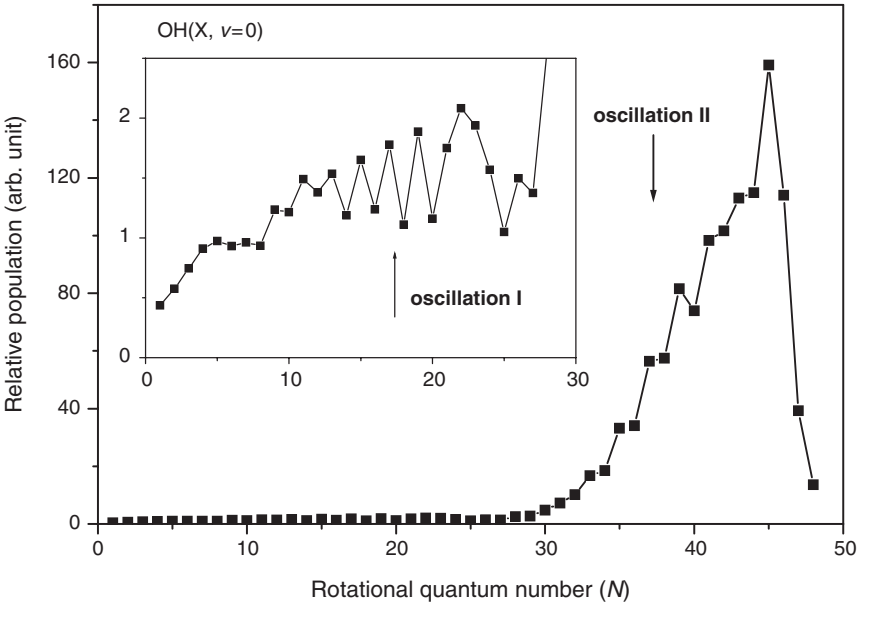

Figure 11. The rotational distribution of the OH(X, $v = 0$) products from H_2O photodissociation at 121.6 nm.

increasing density of rovibronic states leads to severe overlapping of the rotational manifolds for these higher vibrational levels. Figure 12(a) shows the vibrational state distribution of the OH(X) product. While the OH(X) $v=0$ product is by far the most important single channel, vibrationally excited OH products comprise approximately half the total OH(X) population for vibrational states up to $v=11$. A significant population of the vibrationally excited OH(X) products is required in order to account for the complicated structures in the translational energy spectrum between 4000 and 10 000 cm^{-1}.

Rotational state distributions of the OH(A) product for $v=0$–3 have also been determined. For highly rotationally excited OH(A), $v=0$, 1 products are dominant as in the ground state, indicating that the angular anisotropy of the potential is also very important to the production of these product states on the H_2O $\tilde{B}^1A_1$ state surface. The vibrational distribution for the OH(A) product has been obtained by integrating the rotational distributions for each vibrational level. Figure 12(b) shows this vibrational state distribution. The population for the OH(A) product decreases almost linearly as the vibrational energy increases. The relative branching ratio of the OH(X) product versus the OH(A) product is well determined to be about 5 : 1.

Early dynamical calculations using time-dependent wavepackets were able to reproduce the general form of the OH rotational population distribution for the $OH(X^2\Pi, v=0)$ level [27]. This was based on the rather limited *ab initio* surfaces of Theodorakopoulos *et al.* [37]. The branching fraction for the $\tilde{B}^1A_1 \rightarrow \tilde{A}^1B_1$ route to the ground state OH radical relative to the $\tilde{B}^1A_1 \rightarrow \tilde{X}^1A_1$ route was shown to increase with *a*-axis rotational excitation of the parent molecule, whilst

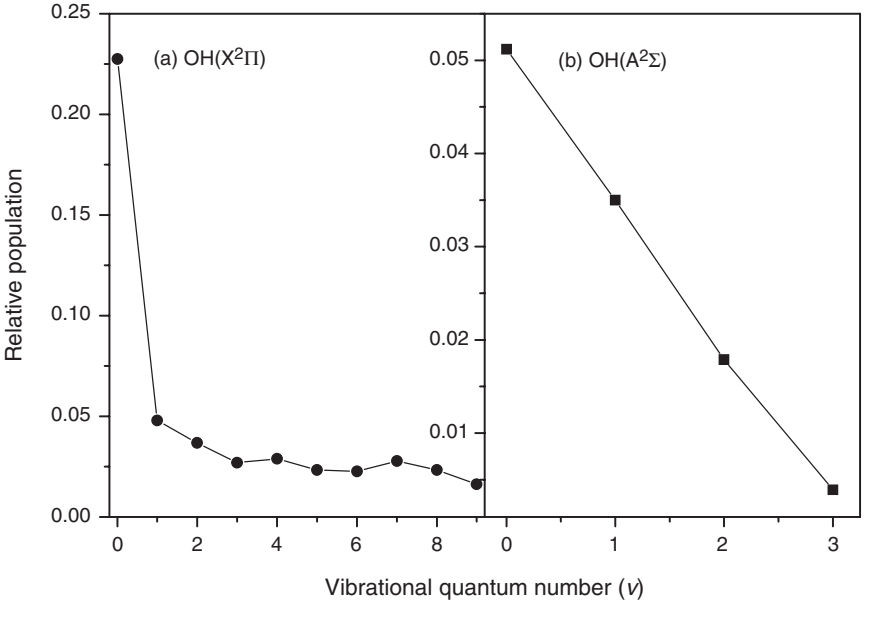

Figure 12. (a) Vibrational state distributions of $OH(X^2\Pi)$ product; (b) vibrational state distribution of $OH(A^2\Sigma)$ product.

the second of these routes is associated with higher angular acceleration of the OH on the final surface than for the first route. Recently, van Harrevelt and van Hemert have used their new potential energy surfaces for water to carry out a complete three-dimensional quantum mechanical description of its photodissociation at a number of energies following $\tilde{B} \leftarrow \tilde{X}$ excitation from the rotational ground state [38]. Diabatic electronic surfaces were constructed from the adiabatic electronic states and matrix elements of the electronic angular momentum operators, following a well-defined procedure [39]. The dynamics were studied using wavepacket methods, and the evolution of the time-dependent wavefunction discussed in detail. These calculations show that both the absorption spectrum and the product state distributions are strongly influenced by transient resonances on the adiabatic $\tilde{B}^1A_1$ state surface, which probably involve both stretching and bending motions [40]. In consequence the branching ratios between dissociation channels and the vibrational and rotational distributions are strongly energy dependent. These theoretical results agree at least qualitatively with the available experimental data. It is also shown that molecular rotation plays an important role in the photofragmentation process. Three-dimensional trajectory calculations have also been performed on this system recently. Further insights into the dynamics of dissociation processes were provided in these investigations. The essential dynamical features in the trajectory studies also agree well with the quantum calculations by van Harrevelt and van Hemert [38]. Of particular note, it was concluded that the highly vibrationally excited OH products are produced by indirect trajectories, whereas the $v=0$ OH products are mainly due to direct dissociation.

3.2.2. Rovibrational dependent anisotropy parameters. The distributions of the angular anisotropy parameter have also been determined for the different rovibrational levels of the OH product. Figure 13 shows the $\beta(N)$ distribution for the OH(X) product in the $v=0$ state. This distribution shows a marked variation in the β parameter over the observed range of N values. For N less than 10, for N between 23 and 28, and for N greater than 42, the β parameter is of the order of $+1$. In between these ranges there are two regions of local oscillation in β. Starting from $N=10$ to 22, the β parameter alternates with higher β at even N and lower β at odd N. However, for the second local oscillation (from $N=29$ to 40), the β parameter alternates in an opposite way with higher β at odd N and lower β at even N. Note that these two regions of oscillation in β are the same as the two regions of oscillation in the rotational population (figure 11). These observed oscillations are very intriguing and indicate that there could be more than one dissociation mechanism leading to the ground state OH. More careful inspection reveals that in the lower N range the population alternation is much more prominent in perpendicular polarization than in parallel polarization, whereas the reverse is true in the higher N range. The source of these oscillations for the most important OH(X, $v=0$) channel is discussed below.

Anisotropy parameters have also been determined for the OH(X) product from $v=1$ to 4 in the same way. These distributions are significantly different from each other. β again varies widely with N, but the distributions are very different from that for the OH(X, $v=0$) product, indicating the complex nature of H_2O photodissociation

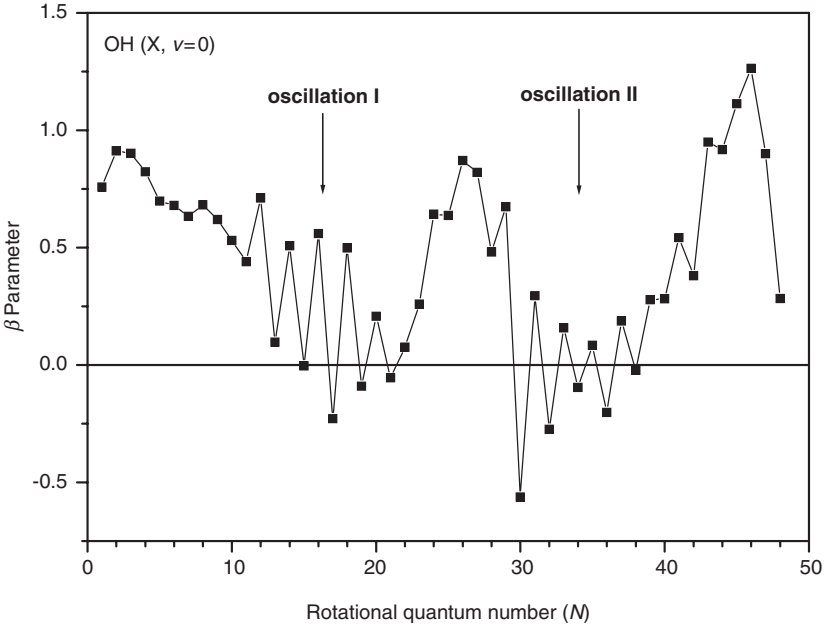

Figure 13. The anisotropy parameters for the OH(X, $v=0$, N) products. The two oscillation sites correspond exactly to the population oscillations exhibited in figure 11.

at 121.6 nm. For higher vibrational levels the β parameters cannot be determined accurately because of significant correlations through overlapping lines. The anisotropy parameters have also been determined for the OH(A) product for $v=0$ to 3. The variations in β are again quite different from each other. Except for $v=3$, the anisotropy parameter oscillates as the N quantum number increases. There are also some general features for these distributions. Near the energetic limit, the anisotropy parameter is normally higher than for the lower N states. This probably arises because the generation of high N products requires the experience of large angular forces during the dissociation.

3.2.3. Effect of parent rotational excitation on the OH product state and angular distribution. The rotational temperature of the H_2O sample in the molecular beam was quite low, about 10 K. As in the hydrogen molecule, the water molecule has *para* and *ortho* rotational levels with nuclear spin-statistics of 1 : 3, respectively. Since the *para* and *ortho* rotational levels have different nuclear spin wavefunctions, the conversion between the *para* and *ortho* levels is essentially forbidden, as in the hydrogen molecule. In H_2O, the nuclear spin-statistics for the lowest rotational levels are as follows:

Level	Energy (cm^{-1})	Nuclear spin statistics
0_{00}	0.00	1
1_{01}	23.80	3
1_{11}	37.16	1
1_{10}	42.39	3

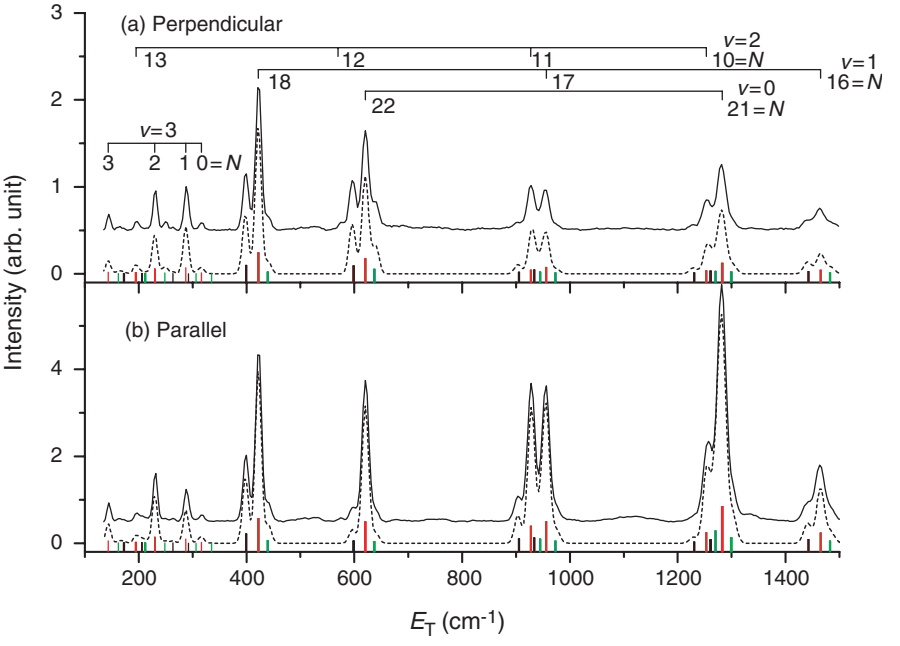

Figure 14. The product translational energy distributions at very low translational energy region. The solid lines are the experimental results while the dotted lines are the simulated distributions. (a) The photolysis laser polarization is perpendicular to the detection axis; (b) the photolysis laser polarization is parallel to the detection axis.

Consequently, even at the lowest rotational temperature both the 0_{00} and 1_{01} levels will be populated, with a ratio of 1 : 3, respectively. The spacing between these different rotational levels of H_2O is such that the parent rotational levels are not well resolved in the product translational energy distribution for the high translational energy region because of the limited translational energy resolution. In the very low translational energy region associated with the OH product in the A state, however, peaks from the same OH(A) product from different parent rotational states can be resolved because of their different available energies and the higher translational energy resolution. Figure 14 shows an expanded plot of the product translational energy distributions (figures 9a and 10a) in the very low translational energy region (from 100 to 1500 cm^{-1}). Each product rotational level is associated with multiple peaks (see the peak labelled with $v = 1$, $N = 18$). These multiplets arise from the different parent rotational levels of H_2O, 0_{00}, 1_{01} and 1_{11} from low to high energy. From this figure we can investigate the effect of the parent rotational excitation. By simulating the translational energy distributions, relative dissociation cross-sections can be derived for different parent rotational levels. The dashed curves in figure 14 are the simulated distributions including the different parent rotational levels. An interesting observation from these distributions is that the shape of the multiplet peak corresponding to each OH(A) rotational level for the perpendicular polarization is not necessarily the same as that for the parallel polarization; see for example the peak labelled as $v = 0$, $N = 22$. From the simulations, relative populations are determined for the

OH(A) product in the low translational energy region from H_2O in different rotational levels for both polarizations. The anisotropy parameters for the OH product from different parent rotational levels are determined. Experimental results indicate that the β parameters for the OH(A) product from the three parent H_2O levels, 0_{00}, 1_{01}, 1_{11}, are quite different from each other. Most notably, for the OH(A, $v=0, N=22$) product the β parameter from the 1_{01} H_2O level is positive while the β parameters from the 0_{00} and 1_{11} levelsare negative, indicating that the parent molecule rotation has a remarkable effect on the product anisotropy distributions of the OH(A) product. The state-to-state cross-sections have also been determined, which are also different for dissociation from different rotational levels of H_2O.

3.2.4. Bond energy beyond chemical accuracy for H_2O. The term values for all the available OH(A) rovibrational levels have been determined accurately from spectroscopic data. From the simulation of the translational energy distributions shown in figure 14, including the parent rotational levels, the translational energy release for each OH(A) level can be calculated with high precision. The Lyman-α transition energy is known accurately to be 82 259.1 cm^{-1}, while the total available energy of dissociation from the 0_{00} level of H_2O to produce the lowest quantum level of OH($X^2\Pi_{3/2}$, $v=0, N=1$) derived from the simulation is 41 108.0 cm^{-1}. The dissociation energy D_0^0, defined as from the lowest H_2O state to the lowest OH level, is therefore determined to be 41 151.1 cm^{-1}. The error bar on D_0^0 is estimated to be 5 cm^{-1} and should have a confidence level of at least 95%. The new value provides the most accurate bond dissociation energy for the water molecule thus far.

3.2.5. Population alternations and quantum interference. Recently, two-dimensional quantum dynamical calculations using *ab initio* surfaces from Murrell and co-workers [41, 42] which span the regions that include O–H–H conical intersections of the $\tilde{B}^1A_1$ and $\tilde{X}^1A_1$ surfaces as well as those with H–O–H geometry, shows that the even/odd intensity alternation in the OH($v=0$) rotational distribution could arise through quantum interference between components of the wavefunction emanating on the $\tilde{X}^1A_1$ surface from these two type conical intersections [36]. However, for both these sets of calculations one OH bond length was fixed, so that vibrational excitation of an OH fragment, or three-body dissociation, could not occur. This explanation was questioned by van Harrevelt and van Hemert on the grounds that their calculations yielded even–odd oscillations, not only for OH(X) but also for OH(A) [38]. Although there are rapid fluctuations with N in the rotational populations and anisotropy parameters of most vibrational states of both OH(X) and OH(A), a clear even/odd alternation sustained over more than 10 consecutive N-values is observed only for OH(X) $v=0$. Furthermore, the two spectra recorded in limiting polarizations differ in that the high N alternation ($N\sim40$) is most prominent in parallel polarization, whereas the lower N alternation ($N\sim15$) is most prominent in perpendicular polarization. This contrasting behaviour is not apparent from the summed populations in figure 11. Further detailed three-dimensional wavepacket analysis, which uses attenuated waves near the second conical intersection (O–HH), shows that the population alternation is strongly related to the conical intersection pathways, indicating

strongly that the population alternations in the OH(X, $v = 0$) rotational distribution are caused by the dynamical interference between the two distinct conical intersections between the $\tilde{B}$ and $\tilde{X}$ surfaces.

3.2.6. Extremely rotationally excited OH from HOD dissociation through conical intersection. The substitution of hydrogen by deuterium often leads to significant changes in processes under dynamical control, particularly where non-adiabatic effects such as conical intersections are involved. Photodissociation of HOD has been recently studied in order to study such dynamical effects in our laboratory using the same method described above [43]. The experiment was carried out using a mixed sample of $H_2O/HOD/D_2O$. The contributions from D_2O were then subtracted from the results using the mixed sample. Figure 15 shows the resulting translational energy spectra for the D + OH products at 121.6 nm excitation for two polarizations (parallel and perpendicular to the detection axis). Since translational energy distributions were measured for both parallel and perpendicular polarizations, the angular dependent translational energy distribution $f(E, \theta)$ can be determined for any angle θ. The peaks of the distribution clearly shows that the main products recoil along the direction of the photolysis laser polarization, indicating that these ground state products are mainly produced by passage through the conical intersection between the $\tilde{B}$ and $\tilde{X}$ surfaces in a collinear geometry.

The sharp peaks in figure 15 arise from the rovibronic states of the OH product from the HOD photodissociation at the D-Lyman α wavelength. Most of these peaks can be

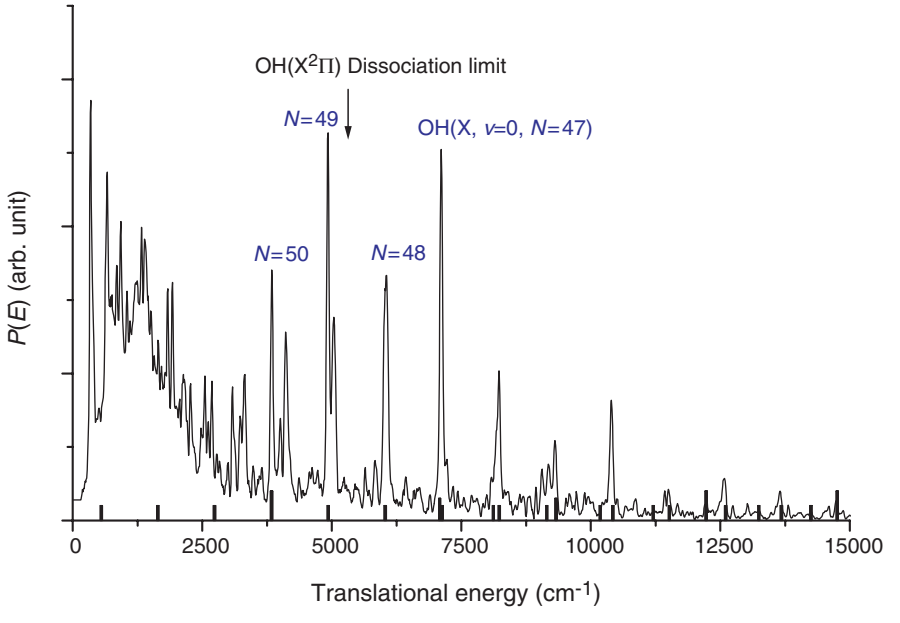

Figure 15. The product translational energy distributions for the OH + D channel from the HOD photodissociation at 121.6 nm with the photolysis laser polarization parallel as well as perpendicular to the detection direction.

assigned to the highly rotationally excited levels of $v=0$–5 of OH($X^2\Pi$) and those of $v=0$ of OH($A^2\Sigma$). The strongest peaks are due to the ground OH products with $v=0$ and 1. The highest peak in the product translational energy spectrum of figure 15 below the dissociation limit is due mainly to the $N=47$ level of OH($X^2\Pi, v=0$), which has a rotational energy of 33400 cm^{-1}, already 94% of the bond dissociation energy of the OH molecule (35426 cm^{-1}). Through careful assignments based on calculated energy levels, higher levels still ($N=48$–50) have been clearly observed. The strongest peak above the dissociation limit is due to $N=49$. Rotational levels of vibrationally excited OH states that lie above the OH dissociation limit have also been observed.

In comparison with H_2O, the rotational excitation of the OH(X) product from HOD photodissociation is noticeably higher than that from H_2O, in which the highest observed rotational level of OH(X, $v=0$) is $N=46$. This can be directly attributed to the kinetic consequences of the difference in product masses. In H_2O, or in D_2O, as the two H (or D)-atoms start to accelerate away from the symmetrical Franck–Condon configuration, the developing kinetic energy will tend initially to be equally shared between them. One of these atoms will dissociate, while the motion of the other will become the internal energy of the OH (or OD) product. Thus the internal energy distribution of OH from H_2O is very similar to that of OD from D_2O, given the almost identical available energies at 121.6 nm [44]. In contrast, this sharing will tend to be 2/3 to the H atom and 1/3 to the D atom for HOD. Thus if the H atom dissociates, its partner OD will tend to have a lower internal energy distribution than OD from D_2O. Conversely, if the D atom dissociates its partner OH will tend to have a higher rotational energy distribution than OH from H_2O, as observed. It is unusual to generate such an extreme rotational excitation.

These extremely rotationally excited levels, lying above the dissociation limit, are only quasi-bound through the support of a centrifugal barriers. Rotational levels that are only slightly above the dissociation limit have substantial centrifugal barriers to dissociation, therefore the tunnelling probability is expected to be extremely small. However, as rotational excitation further increases, the centrifugal barrier is significantly reduced and thus the tunnelling probability through the centrifugal barrier is dramatically increased. Figure 16 shows the tunnelling lifetimes of these extremely OH rotationally excited levels that are above its dissociation limit, calculated using the semiclassical phase integral method [45]. It is interesting to point out that even though the $N=50$ pure rotational level of OH($X^2\Pi, v=0$) is already more than 1000 cm^{-1} above its dissociation limit, the tunnelling lifetime of this state through the centrifugal barrier is much longer than the age of the universe, about 13.4 billion years [46]. This indicates that the first few super-rotationally excited levels above the dissociation limit are essentially stable quantum states. However, as the rotational energy increases, the tunnelling lifetime drops very rapidly. For the $N=53$ rotational level of OH($X^2\Pi, v=0$), which is $\sim$0.5 eV above the dissociation limit, the tunnelling lifetime is about 1 day, and at $N=60$ it is already in the femtosecond time-scale, indicating that this rotational level is only stable for a few vibrational periods. From these theoretical predictions, no quasi-bound levels

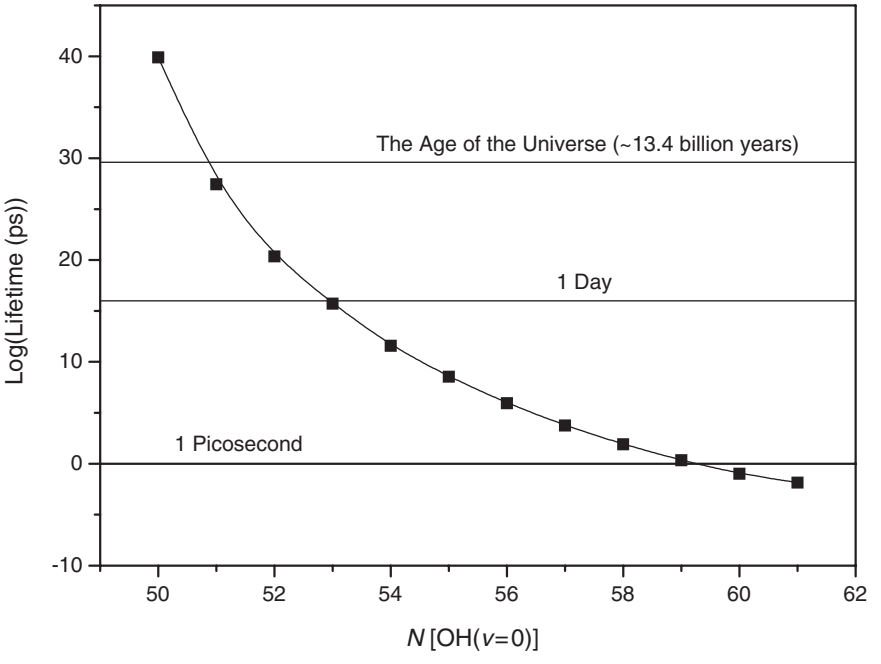

Figure 16. Tunnelling lifetimes of the super rotationally excited OH molecules.

of OH($X^2\Pi, v=0$) should exist above $N=62$. These highly excited OH molecules are substantially stretched by centrifugal force. For example, the mean bond length for $N=47$ is about 34% longer than for the rotationless OH molecule, while that of $N=50$ is about 43% longer. Since these rotationally excited molecules are significantly stretched like highly vibrationally excited molecules, it would be interesting to compare the physical and chemical properties of these two extremely different excited species.

3.2.7. The single N propensity in the HOD + $h\nu \rightarrow$ OD + H dissociation process. Recently, the photodissociation process, $HOD + h\nu \rightarrow OD + H$, has also been studied at 121.6 nm using the experimental technique described above. Contributions from H_2O were then subtracted from the results of the mixed sample. The experimental TOF spectra of the H atom from HOD were then converted into translational energy spectra in the centre-of-mass frame. Figure 17 shows the translational energy spectra of the H-atom products at 121.6 nm excitation using two different polarization schemes (parallel and perpendicular to the detection axis). The spectra were taken at a total stagnation pressure of 600 torr of a sample of 3% $H_2O/HOD/D_2O$ in Ar. Based on previous spectroscopic data on the OD molecule, all sharp features in the translational energy spectra shown in figure 17 can be clearly assigned. The OD products with translational energy above 8000 cm^{-1} are all in the ground electronic state ($X^2\Pi$), while the sharp structures below 5000 cm^{-1} are mostly attributed

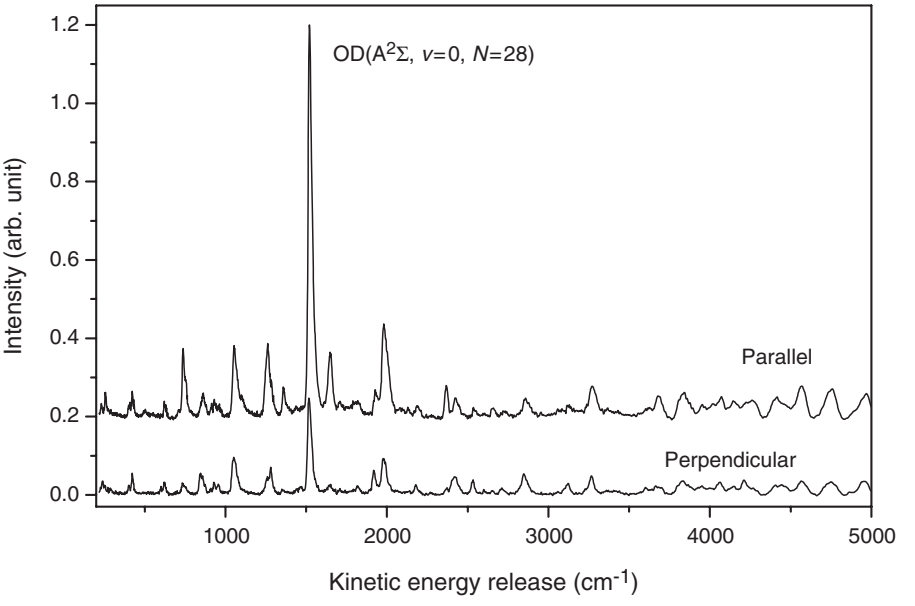

Figure 17. The product translational energy distributions for the OD + H channel from the HOD photodissociation at 121.6 nm with the photolysis laser polarization parallel as well as perpendicular to the detection direction.

to the OD products in the electronic excited $A^2\Sigma$ state. From the translational energy distribution, it is obvious that most of the OD($A^2\Sigma$) products are in the $v=0$ state. The rotational state distribution shows that the population of the OD($A^2\Sigma$) product at $v=0$ and $N=28$ is much larger than that of OD in other rotational states. This is a very interesting phenomenon since only the population of a single rotational state OD product ($v=0, N=28$) is significantly enhanced. It is also interesting to note that the anisotropy parameter for the $N=28$ OD($A^2\Sigma$) is also significantly larger than the rest of the OD products in other rotational levels, indicating that some interesting mechanism lies behind this single J enhancement. This type of phenomenon was not observed in the photodissociation of other similar systems such as H_2O, D_2O and HOD with D detection at the Lyman-α wavelength excitation. Based on theoretical analysis, this single rotational state product propensity is attributed to a dynamically constrained threshold effect in the HOD photodissociation process [47].

4. The $O(^1D) + H_2$ reaction: insertion versus abstraction

The reaction of $O(^1D) + H_2$ plays a significant role in atmospheric [48] and combustion chemistry [49]. This reaction is also a well-known benchmark system for an insertion type chemical reaction at low collision energies. Extensive experimental and theoretical studies have been carried out in order to elucidate the dynamics of this reaction (and isotope variants) [50–71]. A more complete review of the studies on the $O(^1D) + H_2$ reaction during the last decade or so can be found in a very recent review article by Casavecchia [4]. Previous experimental studies found that this reaction

is dominated by the insertion reaction mechanism. Very recently, Liu and co-workers [67–71] have measured the excitation function and the differential cross-sections at different energies for the $O(^1D) + HD$ reaction using Doppler-selected time-of-flight methods. Their experimental results show that at low collision energies (<1.8 kcal/mol), the reaction is mainly through the insertion pathway that shows roughly a forward–backward symmetric product angular distribution. At higher collision energies (>1.8 kcal/mol), however, an additional abstraction channel becomes important. This abstraction reaction mechanism is likely caused by the excited state reactive surfaces [70, 71], even though not all experimental results point in this direction. Due to the limited resolution of the above experiments, quantum state-specific information on the radical products (OH) has not been derived for this reaction in their experimental studies.

In this section, we will describe detailed experimental results on the $O(^1D) + H_2(HD, D_2)$ reactions at different collision energies to probe the fine dynamics in this interesting system. In the first two parts, we will first describe the study of the $O(^1D) + p\text{–}H_2$ reaction at 1.3 kcal, to show an example of the state-to-state dynamics of a barrierless insertion reaction, and then the single rotational excitation effect on the dynamics of this reaction. In the third part of this section, we will describe the experimental results of the $O(^1D) + D_2$ reaction at two different collison energies to provide clear experimental evidence of the appearance of the collinear abstraction mechanism at higher collision energies in this reaction. In the last part of this section, an interesting isotope effect will also be discussed in the $O(^1D) + HD$ reaction.

4.1. *The $O(^1D) + p\text{-}H_2 \rightarrow OH(X^2\Pi, v, N) + H$ reaction at 1.3 kcal/mol: state-to-state dynamics of a barrierless insertion reaction*

The $O(^1D) + H_2 \rightarrow OH + H$ reaction were studied at the collision energy of 1.3 kcal/mol, which is significantly below the 1.8 kcal/mol barrier for the abstraction channel inferred from previous experimental studies [69]. This allows us to look at the reaction dynamics of a pure insertion chemical reaction at the state-to-state level. The set-up used for the studying the $O(^1D) + H_2 \rightarrow OH + H$ reaction is basically the same apparatus used in the H_2O photodissociation studies but slightly modified. The experimental scheme for this reaction is shown in figure 18. The detection scheme used in the crossed beam experiment is almost exactly the same as the photodissociation experiment described above, except that a rotating MCP detector is used here instead of a fixed angle detector. Two parallel molecular beams (*para*-H_2 and O_2) were generated with similar pulsed valves in this experiment. The $O(^1D)$ atom beam was produced by the 157 nm photolysis of the O_2 molecule via the Schumann–Runge band. The 157 nm laser light is produced by a F_2 laser (Lambda Physik LPX 210I). The $O(^1D)$ beam was then crossed at 90° with the H_2 molecular beam. The *para*-H_2 molecular beam is generated by expanding the H_2 sample through a pulsed nozzle, which is cooled to liquid nitrogen temperature. This is to reduce the uncertainties of the collision energy by minimizing the beam velocity spread. A small aperture is used to define the $O(^1D)$ beam between the O_2 and H_2 beams. The H-atom products were detected using the technique described above with a rotatable MCP detector. The velocity of the $O(^1D)$ beam has been measured to be 2050 m/s with a very narrow velocity

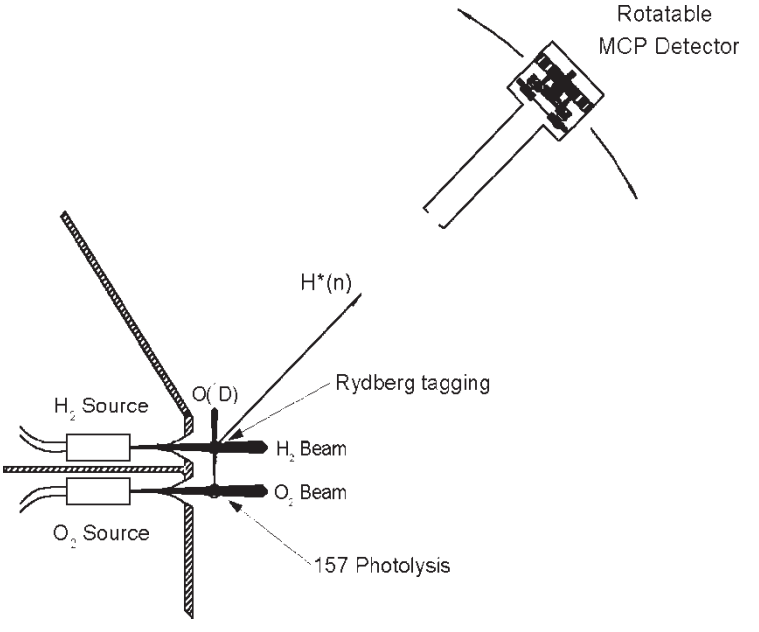

Figure 18. The schematic of the experimental set-up for studying the crossed beam $O(^1D) + H_2 \rightarrow OH + H$ reaction.

distribution ($v/\delta v > 50$), while the velocity of the liquid nitrogen cooled *para*-H_2 beam is 1384 m/s with a speed ratio ($v/\delta v$) of about 15. Since *para*-H_2 is expanded at liquid nitrogen temperature, H_2 molecules in the beam should be all in the $j = 0$ state [11]. In order to understand the kinematics of reactive scattering, figure 19 shows the Newton diagram for this reaction investigated using the above experimental conditions.

Time of flight spectra of the H-atom products have been measured at 18 laboratory angles (from 117.5° to −50° at about 10° intervals). Figure 20 shows a typical TOF spectrum at the laboratory (LAB) angle of −50° (forward direction). By definition, the forward direction of the OH product is defined here relative to the $O(^1D)$ beam. The TOF spectrum in figure 20 consists of a lot of sharp structures. All these sharp structures clearly correspond to individual rotational states of the OH product, indicating that these TOF spectra have indeed achieved rotational state resolution for the $O(^1D) + H_2 \rightarrow OH + H$ reaction. By converting these TOF spectra from the laboratory (LAB) frame to the centre-of-mass (CM) frame using a standard Jacobian transformation, the product translational energy distributions obtained at different LAB angles for the title reaction can be obtained. Figure 21 shows the total product translational energy distribution at the LAB angle of −50°. All the peaks in the distribution can be assigned to the OH products at different spin–orbit rovibrational levels. In this reaction, the total available energy is about 45 kcal/mol, which can produce OH products up to $v = 4$ in the ground electronic state.

By integrating the total intensity of the translational energy distribution at each LAB angle, the total product angular distribution can be determined, which is shown

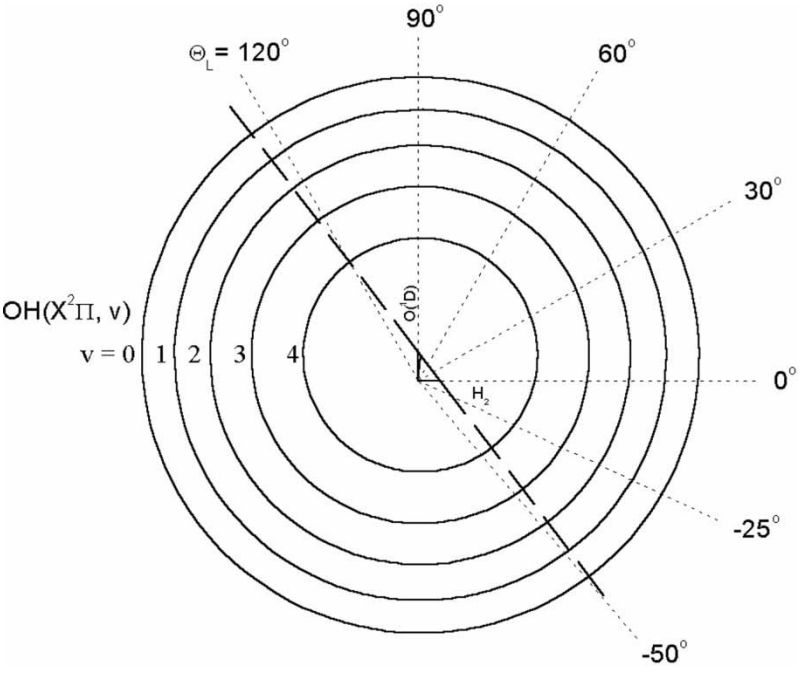

Figure 19. The Newton diagram for the $O(^1D) + H_2 \rightarrow OH + H$ reaction.

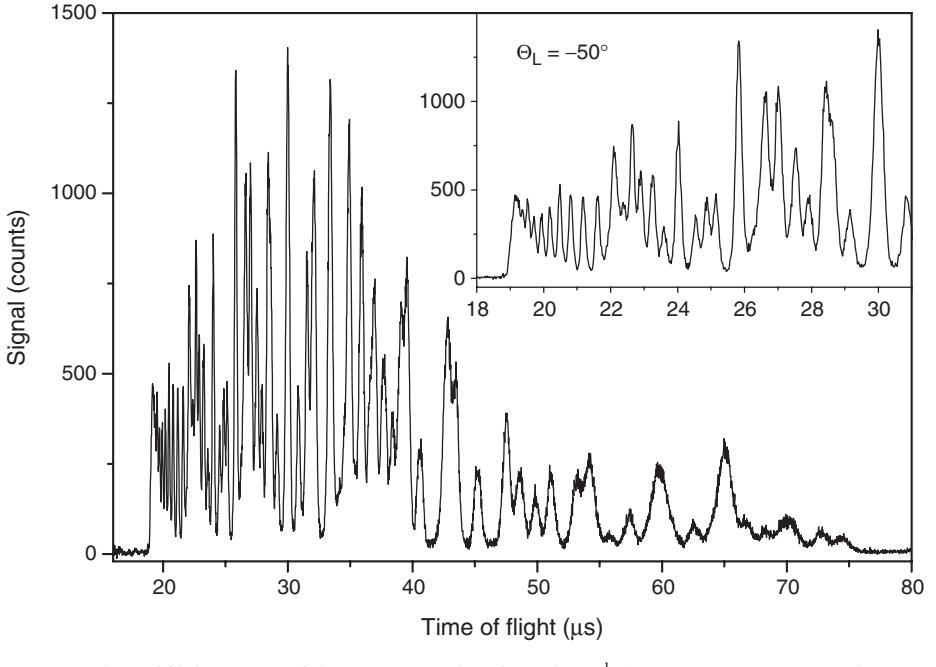

Figure 20. Time of flight spectra of the H atom product from the $O(^1D) + p\text{-}H_2 \rightarrow OH + H$ reaction at -50° laboratory scattering angle at the collision energy of 1.3 kcal/mol.

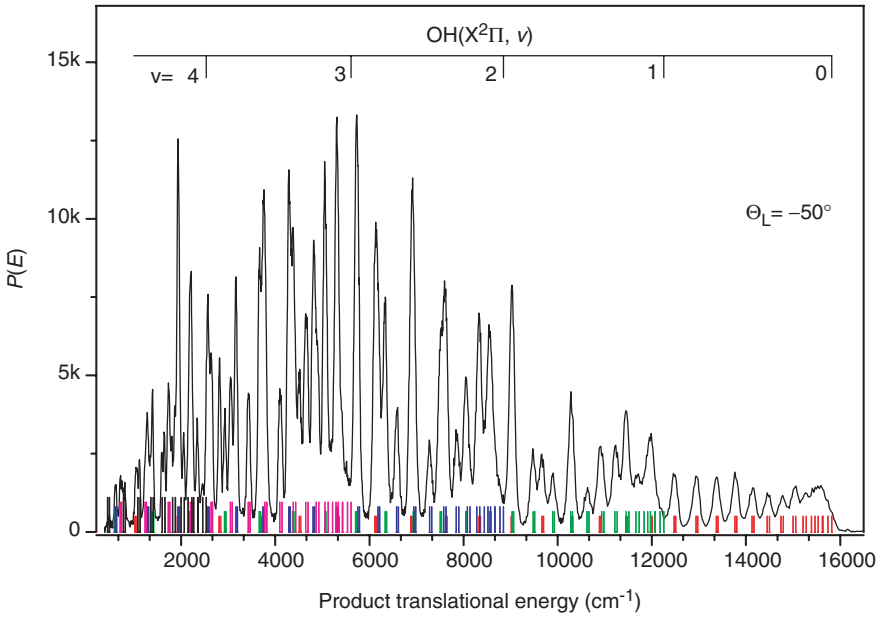

Figure 21. The CM product translational energy distributions at the laboratory angle of -50° from $O(^1D) + p\text{-}H_2 \rightarrow OH + H$ reaction.

in figure 22. From this distribution, it is apparent that the total H product is essentially forward and backward symmetrically scattered with regard to the H_2 beam direction. This result is quite consistent with previous experimental studies [65, 68, 69]. The forward and backward symmetry of the total H product is a clear signature of the dominant role of the insertion mechanism in this reaction. Since the CM angles are not constant for a certain laboratory angle at different product (H) velocities, a translational energy distribution obtained from the direct conversion of the TOF spectra contains scattering information in a range of CM angles. In analysing these experimental data, all rovibrational states ($v \leq 4$) of the OH product are included in fitting each translational energy distribution obtained. From the simulations, relative population distributions of each rovibrational state of the OH product were determined at 18 different LAB angles. From these results, quantum state distributions of the OH product in the CM frame ($\Theta_{cm} = 0^\circ$ to 180° at 10° steps) can then be determined using polynomial interpolations of the above results. Thus, rotational state-resolved differential cross-sections are determined. From these typical distributions, detailed dynamical features have been revealed. As we have pointed out above, the total product angular distribution is roughly forward and backward symmetric. For an individual quantum state OH product, however, the angular distribution is not necessarily symmetric as shown in figure 23. From figure 23, the difference between the translational energy distribution at $\Theta_{cm} = 0^\circ$ or 180° and that at 90° is even more remarkable. From the quantum state distributions, it is clear that the main difference between the side scattering and the forward or backward scattering is the low rotationally excited OH product relative to the $O(^1D)$ beam direction. For forward and backward scatterings, significant amounts of the OH products are populated

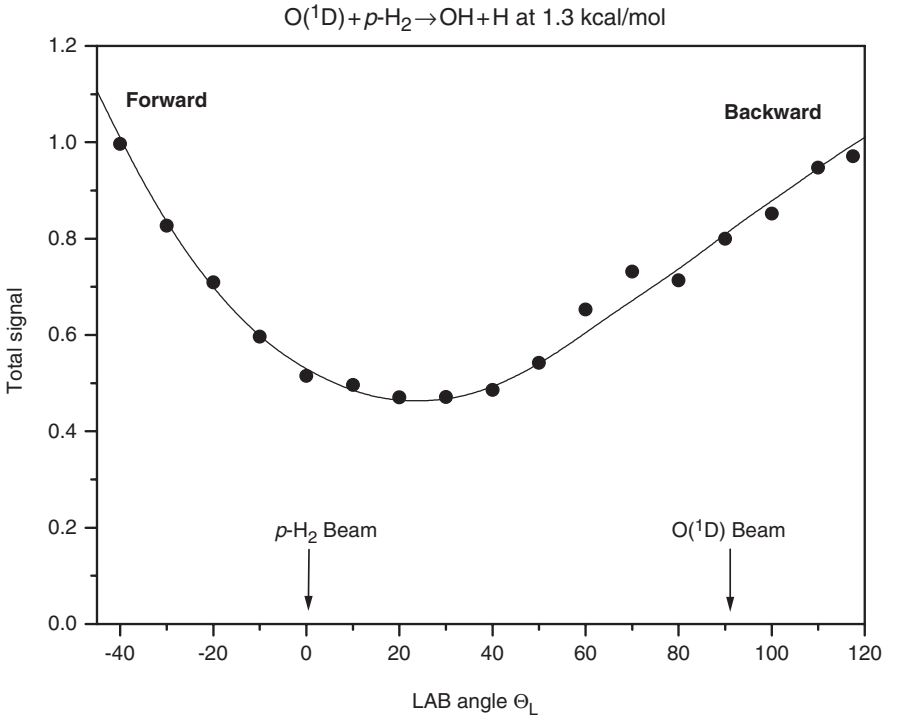

Figure 22. The H atom product angular distribution in the laboratory frame for the $O(^1D) + p\text{-}H_2 \rightarrow OH + H$ reaction at 1.3 kcal/mol.

in lower rotationally excited states of different vibrational states. This is quite obvious from the translational energy distributions shown in figure 23 in which lower rotationally excited OH products (near each vibrational state energy limit) are much more pronounced in the forward/backward directions than in the sideways scattering. The highly rotationally excited OH products, however, are more isotropic in their angular distributions, and sometimes even strongly sideways scattered. These results are easily understandable. In the $O(^1D)$ insertion reaction with the H_2 molecule, significant numbers of trajectories should have low impact parameters. The OH product in the forward/backward directions should carry small angular momentum because of angular momentum conservation in these low impact collisions. For higher rotationally excited OH products, however, angular distributions should not be as simple.

By incorporating all translational energy distributions in the CM frame, a three-dimensional contour plot of the differential cross-sections in terms of angle and translational energy can be constructed, as shown in figure 24. As a whole distribution, it is clear that for higher translational energies (or lower internal excitation for OH), the products are more forward/backward scattering than sideways scattering relative to the $O(^1D)$ beam direction. At lower translational energies (or higher OH internal excitation), however, the OH product scattering is more complicated with strong side scattering in certain regions. Figure 25 shows the angular distribution of different vibrational excited OH products, in which the angular distribution for each vibrational state

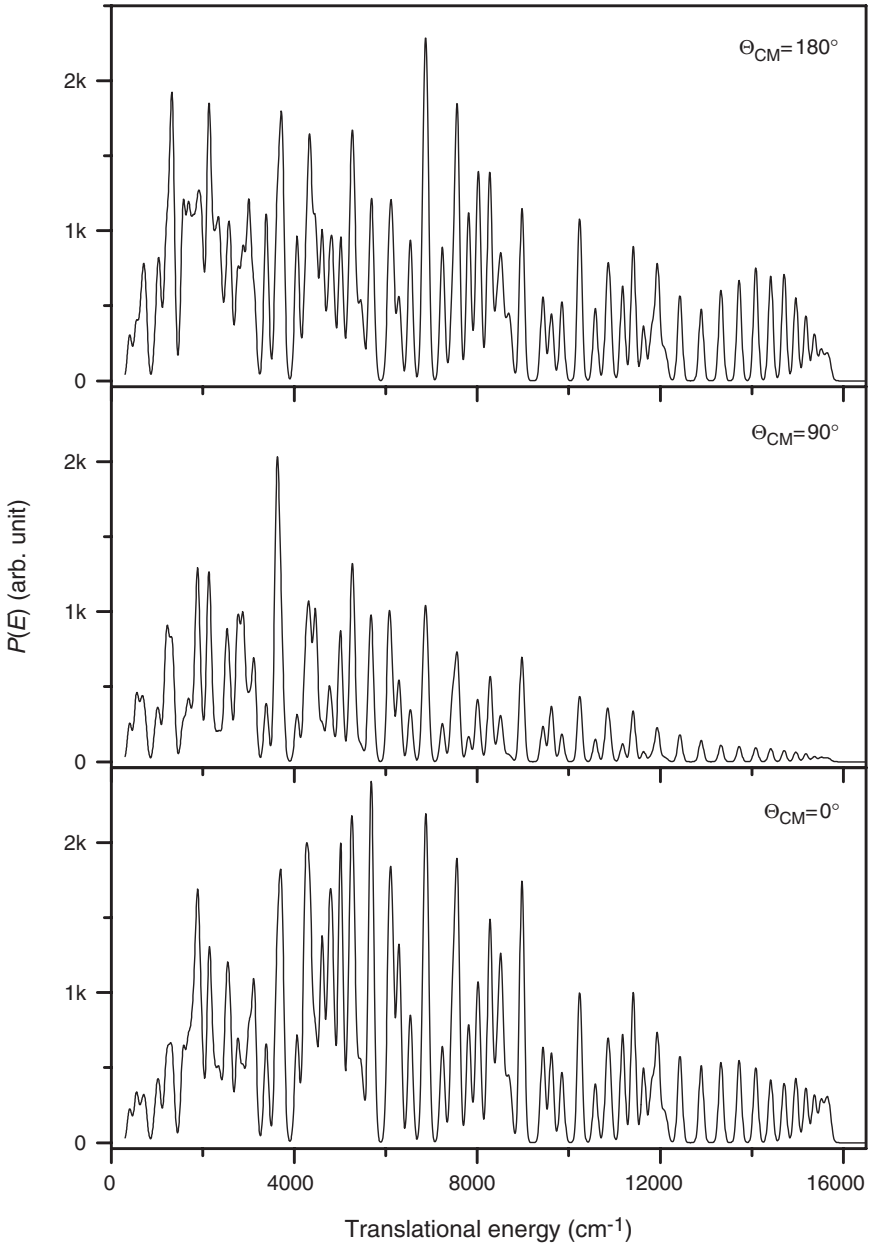

Figure 23. The CM translational energy distributions at three different laboratory angles corresponding to forward (0°), sideway (90°) and backward (180°) scattering.

OH product are mostly forward–backward symmetric, except the $v=4$ OH product. This indicates that rotational product asymmetry in the angular distribution is not sustained in the rotationally summed OH(v) product. Since OH quantum state distributions have been determined at different CM scattering angles, total quantum

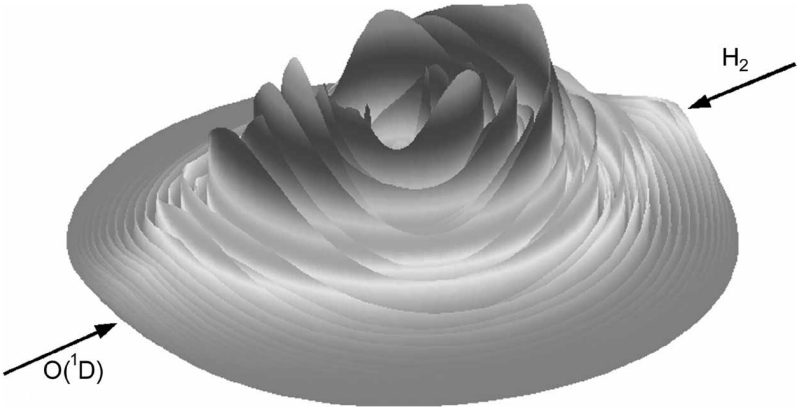

Figure 24. The three-dimensional plot of the product flux contour diagram for the $O(^1D) + H_2 \rightarrow OH + H$ reaction at the collision energy of 1.3 kcal/mol.

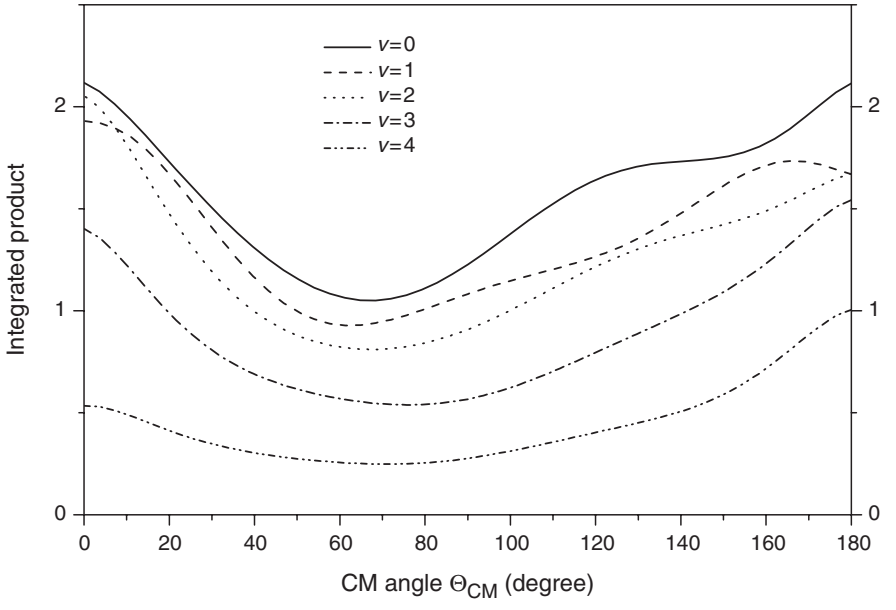

Figure 25. The angular distribution of different vibrational excited OH products for the $O(^1D) + H_2 \rightarrow OH + H$ reaction at the collision energy of 1.3 kcal/mol.

state distributions for this reaction can be easily determined by simply integrating these distributions over different CM angles. Figure 26 shows the full quantum state distributions obtained for the title reaction. Such measurements were not possible previously because of problems associated with the OH laser induced fluorescence (LIF) detection [72]. In the lower panel of this figure, OH rotational distributions for each vibrational state are presented. The distributions at different vibrational states are actually quite similar in which all distributions peak near their energetic limit, indicating that the majority of the OH products from this reaction are rotationally excited.

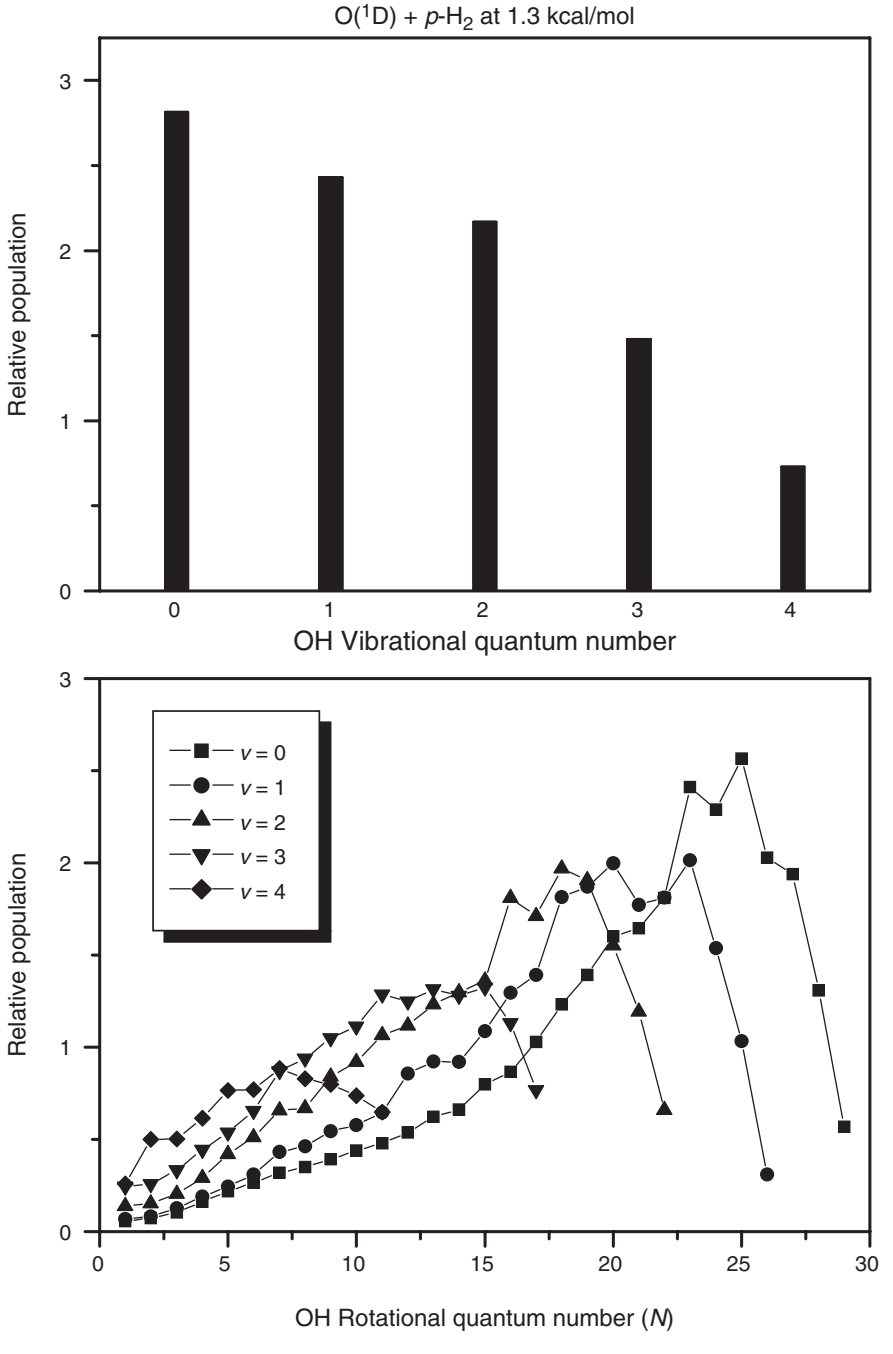

Figure 26. The total OH product vibrational and rovibrational state distributions for the $O(^1D) + H_2 \rightarrow OH + H$ reaction.

In the upper panel of figure 26, the total OH product vibrational state distribution is shown. The population in different vibrational states monotonically decreases as the vibrational energy increases. In this experiment, even though extremely high translational energy resolution has been achieved, it is still not sufficient to resolve the spin–orbit states of the OH product at $v=0$–3 and the lambda doublet states for all the vibrational states. For OH($v=4$) products, however, the spin–orbit components (F_1 and F_2) have been resolved. A clear propensity for the F_1 component OH($v=4$) product has been observed for this reaction.

In this part, we have shown an excellent example of quantum state-resolved reactive scattering studies on the important $O(^1D)+H_2\rightarrow OH+H$ reaction using the high resolution H-atom Rydberg 'tagging' TOF technique. Rotational state-resolved differential cross-sections have been measured for this reaction for the first time. A full analysis of the experimental results has revealed many interesting dynamics for this prototype system. The experimental results obtained in this work should be able to provide an excellent test ground for theoretical studies of this benchmark insertion reaction.

4.2. *Effect of a single quantum rotational excitation on state-to-state dynamics of the $O(^1D) + H_2 \rightarrow OH + H$ reaction*

The effect of the reagent rotational and vibrational excitation on the reactivity is an interesting issue. In the above experiment, the study was performed for the $O(^1D)$ reaction with the H_2 molecule purely in the $v=0$, $j=0$ level using cooled *para*-H_2 beam. Clearly the H_2 reagent in this experiment is without any rotation. In this part, we would like to describe the results of a sophisticated experimental study of the $O(^1D)$ reaction H_2 with the H_2 reagent in the $j=0$ and $j=1$ level to look at the effect of a single rotational quantum reagent excitation on the dynamics of this reaction. The experiment was carried in exactly the same way as described in the last part, except that two H_2 samples, *para* and *normal*, were used for exact comparisons. In this experiment, *para*-H_2 is purely in the $j=0$ level in the cooled beam, while normal H_2 has one part in $j=0$ and three parts in $j=1$. In this experiment, TOF spectra at eight LAB scattering angles were measured for both H_2 samples with exactly the same experimental conditions. These spectra were measured by switching the two H_2 samples back and forth many times to reduce the systematic errors in the measurements. Since the numbers of density of the two H_2 samples in the beam were controlled to be exactly the same, the TOF spectra (TOFS) of the H-atom products from the $O(^1D)$ reactions with H_2 at both $j=0$ and 1 can be obtained from these two samples using simple arithmetic. Since normal H_2 has two components: $j=0$ (1) and $j=1$ (3), the TOF spectra observed for the *p*-H_2 and *n*-H_2 reactions can be described in terms of that from H_2 at $j=0$ and $j=1$,

$$\text{TOFS}\ (p\text{-}H_2) = \text{TOFS}\ (j=0) \tag{4}$$

$$\text{TOFS}\ (n\text{-}H_2) = 0.75\times\text{TOFS}\ (j=1) + 0.25\times\text{TOFS}\ (j=0) \tag{5}$$

Therefore, the TOF spectra, TOFS, for the H_2 reactions for the pure $j=0$ and 1 levels can be determined from the experimentally measured TOFS for the p-H_2 and n-H_2 reactions,

$$\text{TOFS}\ (j=0) = \text{TOFS}\ (p\text{-}H_2) \tag{6}$$

$$\text{TOFS}\ (j=1) = (\text{TOFS}\ (n\text{-}H_2) - 0.25 \times \text{TOFS}\ (p\text{-}H_2)) \times \frac{4}{3} \tag{7}$$

The TOF spectra were then converted into the product translational energy distributions. Figure 27 shows the product translational energy distributions at the LAB angles of 117°, 30° and −50° for the $O(^1D)$ reaction with H_2 in both $j=0$ and 1 rotational levels. These angles correspond dynamically to the backward, sideways and forward scattering directions for the OH product relative to the $O(^1D)$ atom beam direction or H-atom products relative to the H_2 beam direction. The relative distributions for the $O(^1D)$ reaction with H_2 in $j=0$ and $j=1$ were therefore determined at the eight scattering angles. The ratios of the total products from H_2 ($j=0$) and H_2 ($j=1$) at eight different LAB angles were also determined. By integrating the differences in all eight LAB angles including the $\sin\theta$ weighting factor for the spherical integration, the ratio between the total cross-sections of $O(^1D)$ reaction with H_2 at $j=0$ and $j=1$ are determined to be $\sigma\ (j=1)/\sigma\ (j=0) = 0.95 \pm 0.02$. This shows that the H_2 molecule in $j=0$ is slight more reactive than that in $j=1$, which agrees quite well with quantum theoretical calculations [73].

Clearly, the single quantum H_2 rotational excitation effect on the integral cross-section of the $O(^1D) + H_2$ reaction seems quite small though detectable. The more interesting question is how the single quantum rotational excitation of the H_2 reagent affects the OH product state-resolved differential cross-sections. From figure 27, the product translational energy distributions of the $O(^1D) + H_2$ ($j=1$) reaction are slightly shifted to higher energy with respect to that of the $O(^1D) + H_2$ ($j=0$) reaction. This is because the total energy of the $O(^1D) + H_2$ ($j=1$) reaction is slightly more than that of the $O(^1D) + H_2$ ($j=0$) reaction by $2B_{rot}(H_2)$, i.e. $120\,cm^{-1}$. If we shift the product translational energy distributions of the $O(^1D) + H_2$ ($j=1$) reaction by $120\,cm^{-1}$, all the peak positions in the distributions will be exactly aligned with those of the $O(^1D) + H_2$ ($j=0$) reaction.

From the translational energy distributions shown in figure 27, the distributions in the backward (117°) and forward (−50°) directions show some significant differences for the H_2 ($j=0$) and H_2 ($j=1$) reactions even though the distributions in the sideways scattering direction (30°) are very similar to each other for the two reactions [74]. Since the rovibrational states of the OH radical are well known through previous spectroscopic studies, the translational energy distributions observed can be simulated quite conveniently. From the simulations, state-specific differential cross-sections can be determined for the eight LAB angles measured. From the product state distributions in the backward scattering distribution shown in figure 28, it is clear that a single quantum rotational excitation in the H_2 reagent has a rather significant effect on the OH. The rotational excitation seems to have a rather irregular effect on a specific OH state product, indicating that whether a single rotational excitation would enhance or reduce the state-specific differential cross-sections for a specific state seems to be

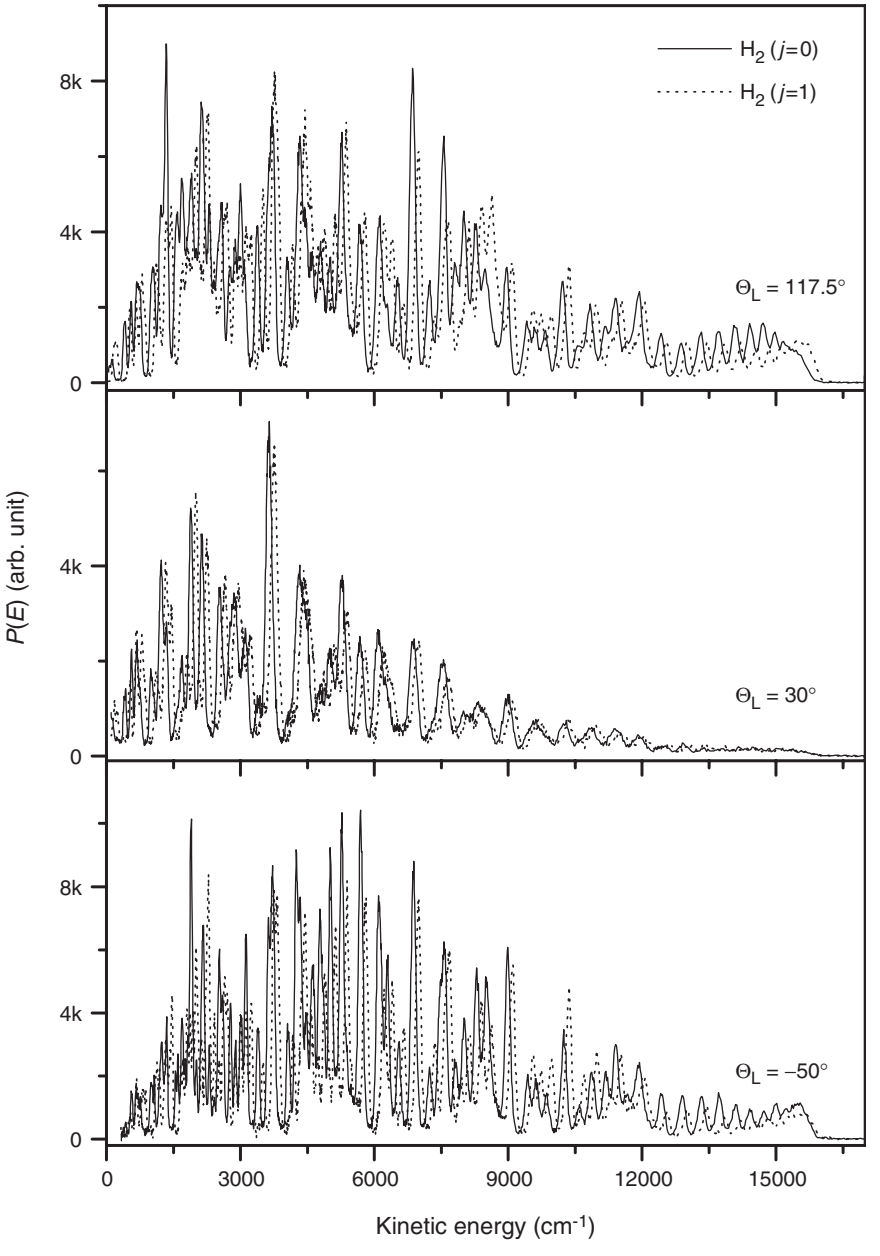

Figure 27. The translational energy distributions obtained for the $O(^1D) + H_2$ ($j = 0$) $\rightarrow$ OH + H and the $O(^1D) + H_2$ ($j = 1$) $\rightarrow$ OH + H reaction at the collision energy of 1.3 kcal/mol.

very unpredictable. These observations are also true for the forward scattering direction even though the effects are very quite different from that of the backward scattering direction. For the sideways scattering, however, the single quantum rotational excitation in H_2 seems to have a very limited effect on the OH-product state distributions,

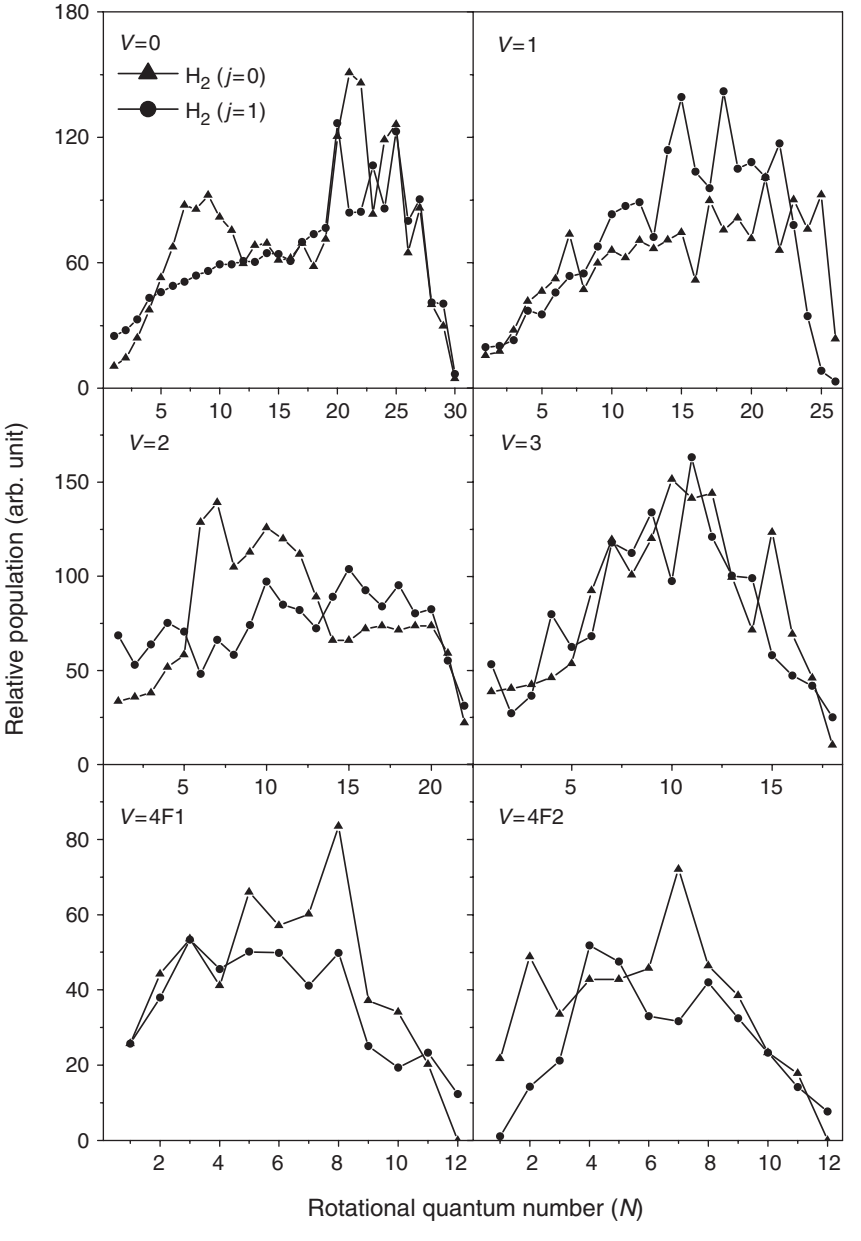

Figure 28. Comparisons of the rovibrational state distributions obtained from the $O(^1D)$ reaction with H_2 at the $j=0$ and $j=1$ levels at the backward scattering 117° laboratory angle.

though slightly noticeable. This is very different from that of the forward and backward scattering products.

Qualitatively, this phenomenon can be understood as the sideways scattering products are normally produced through larger impact parameter (b) collisions,

i.e. larger orbital angular momentum, $\boldsymbol{L} = \mu v b$, while forward/backward scattering products are produced via relative smaller impact parameter (b) collisions, i.e. smaller orbital angular momentum. Therefore, a single quantum rotational excitation ($\boldsymbol{j}$) in H_2 should have a larger effect at the forward and backward directions because the total angular momentum $\boldsymbol{J} = \boldsymbol{L} + \boldsymbol{j}$ for the small $\boldsymbol{L}$ collisions is significantly changed relatively with a single rotational quantum excitation in H_2. However, relatively speaking, the total angular momentum $\boldsymbol{J} = \boldsymbol{L} + \boldsymbol{j}$ is altered only slightly by a single rotational quantum excitation in H_2 for larger impact parameter (larger $\boldsymbol{L}$) collisions which is mostly responsible for the sideways scattering products. The specific effect of the single quantum rotational excitation on the differential cross-sections is also very interesting. The lack of specific patterns for the forward and backward directions in this effect is probably due to the nature of this insertion reaction, which has a large number of reaction resonances. Interestingly, in a similar experiment in our laboratory, it was found that a rotational quantum excitation in D_2 does not have any noticeable effect in the $O(^1D) + D_2$ reaction.

4.3. *Experimental evidence for a collinear abstraction mechanism in $O(^1D) + D_2 \rightarrow OD + D$*

The $O(^1D) + D_2$ reaction was also investigated using the Rydberg 'tagging' technique described above. As we have pointed out above, there is an abstraction mechanism present at higher collision energies, in addition to the insertion mechanism which is dominant for this reaction at low collision energies [67–71]. The nature of this abstraction reaction was, however, not very clear from previous experimental studies. The experiment designed here was intended to clarify the source of this abstraction mechanism. The experiment described here was carried out at collision energies of 2.0 kcal/mol and 3.2 kcal/mol, respectively. The 2.0 kcal/mol collision energy is only slightly above the inferred 1.8 kcal/mol abstraction barrier for the abstraction, which implies that the reaction at this collision energy is mainly due to the insertion mechanism, while the collision energy of 3.2 kcal/mol is significantly above the inferred 1.8 kcal/mol barrier for the possible abstraction channel, providing us with a good opportunity to probe the dynamics of this elusive abstraction channel.

Time-of-flight spectra of the D-atom products have been measured at many laboratory angles at both collision energies. Transtional energy distributions can be derived by direct conversion of these TOF spectra. For the experiment carried out at 2.0 kcal/mol, figure 29(a) shows the total product angular distribution from $\Theta_L = -60^\circ$ to 117.5°, which correspond to the forward (-60°), the sideways (30°) and the backward (117.5°) scattering directions. The direction of the D_2 beam is at $\Theta_L = 0^\circ$, while the direction of the $O(^1D)$ beam is at $\Theta_L = 90^\circ$. By definition, the forwardness and backwardness of the D-atom products are with respect to the D_2 beam direction, while those of the OD products are with respect to the $O(^1D)$ beam direction. From the angular distribution shown in figure 29(a), it is quite obvious that the angular distribution of the reaction product (D) is essentially forward and backward symmetric. That is not too surprising since 2.0 kcal/mol is only slightly above the barrier (1.8 kcal/mol) for the abstraction mechanism inferred from previous experimental studies. It is interesting that even though the total product distribution is forward and backward symmetric,

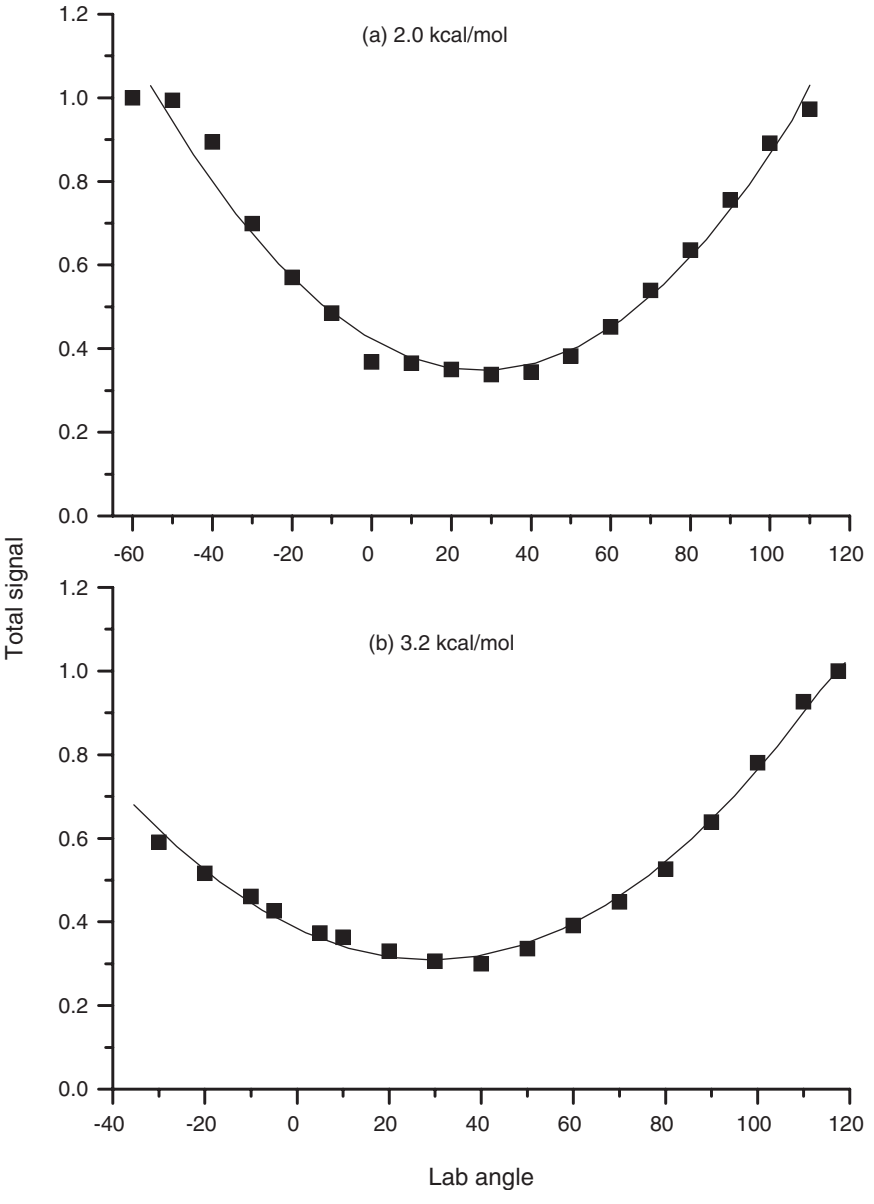

Figure 29. The D atom product angular distribution in the laboratory frame for the $O(^1D) + D_2 \rightarrow OD + D$ reaction at two collision energies: (a) 2.0 kcal/mol and (b) 3.2 kcal/mol.

the product translational energy distributions in the forward and backward directions in the CM frame are noticeably different. Figure 30(a) shows the product translational distributions at $\Theta_L = -60^\circ$ and 117.5° for the $O(^1D) + D_2$ reaction at 2.0 kcal/mol collision energy. Extensive sharp features are present in these translational energy distributions. These sharp structures correspond to the rovibrational structures

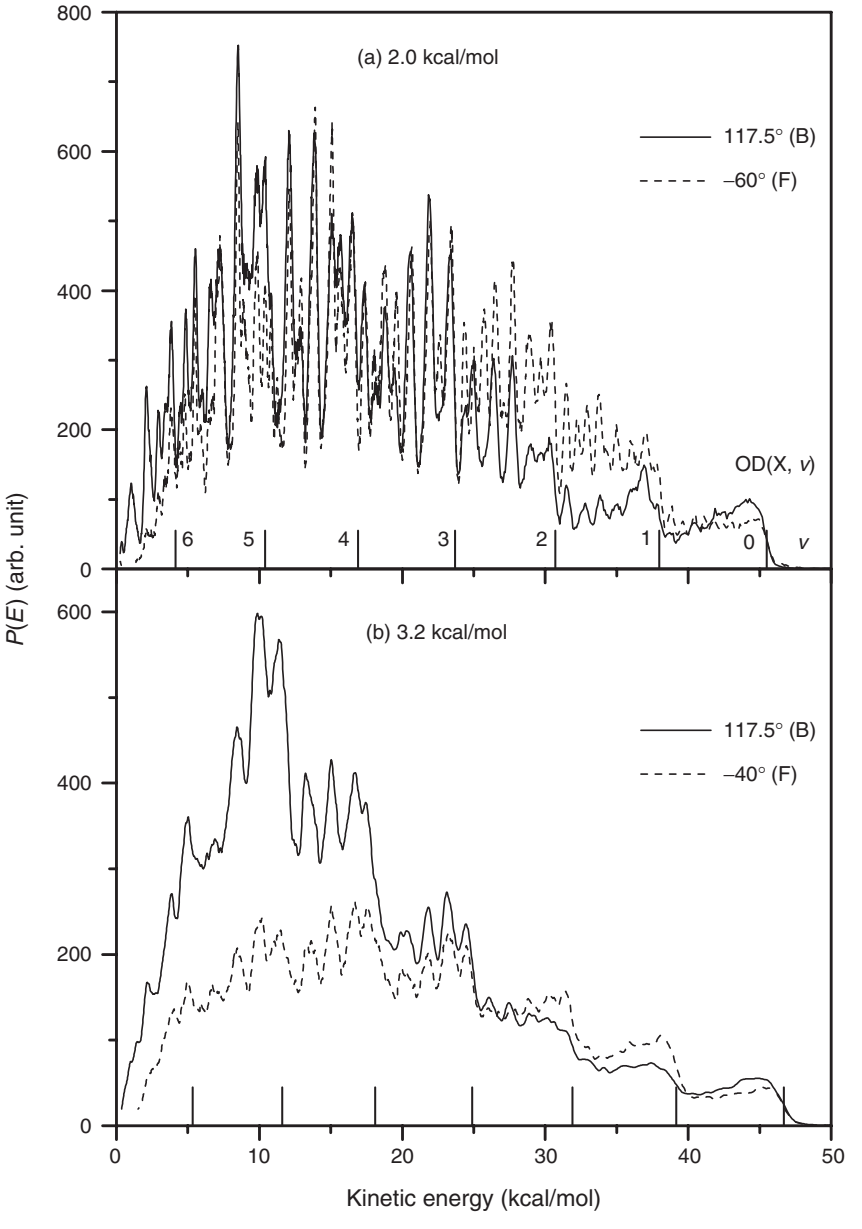

Figure 30. The CM product translational energy distributions at the forward and backward scattering direction for the $O(^1D) + D_2 \rightarrow OD + D$ reaction at two collision energies: (a) 2.0 kcal/mol and (b) 3.2 kcal/mol.

of the OD products since the D atom has no internal energy structure. Most of these structures are overlapped structures of different OD rovibrational states from $v = 0$ to 6. Spin–orbit states of the OD product are not resolved in these TOF spectra. Upon examining the translational energy distributions, it is clear that most of the

OD products are highly rotationally excited since the low rotational OD product at the onset of each vibrational state of OD is not significant in comparison with other regions. The two translational energy distributions possess similar shapes overall. However, the detailed structures of these two distributions are noticeably different, indicating that a state-specific OD product is clearly not exactly forward and backward symmetric. This result is quite similar to that of the $O(^1D) + H_2$ reaction. The overall symmetric OD product distribution at 2.0 kcal/mol is indicative of an insertion type mechanism.

The $O(^1D) + D_2$ reaction is also studied at a higher collision energy, 3.2 kcal/mol, with a room temperature D_2 beam, in order to better understand the reaction mechanisms involved at higher collision energies. When the collision energy of the reaction is increased from 2.0 to 3.2 kcal/mol, the total product angular distribution changes from a roughly forward-and-backward symmetric distribution to a more backward distribution. Figure 29(b) shows the total product angular distribution at 3.2 kcal/mol collision energy. The increase in the backward scattering signal is quite obvious in comparison with that at 2.0 kcal/mol. The nature of these backward scattered products is a very important issue, since that can provide important insight into the reaction mechanism responsible for these backward products. Figure 30(b) shows the two product translational energy distributions in the forward ($\Theta_L = -40^\circ$) and backward ($\Theta_L = 117.5^\circ$) directions in the CM frame at 3.2 kcal/mol collision energy. Clearly, the resolution of these translational energy distributions is worse than those at 2.0 kcal/mol, because the room temperature beam has a much larger beam velocity spread. Although the resolution is much lower at this collision energy, the basic information is not all lost in these translational energy distributions. By comparing the two distributions, it is quite obvious that the translational energy distribution in the backward direction is significantly different from that of the forward direction. At higher translational energy or lower OD internal energy, the distributions in the forward and backward directions are similar, which resembles the results at 2.0 kcal/mol. At lower translational energy or higher internal energy, the backward product is much more pronounced than that of the forward direction. These more backward products are likely the OD($v = 4$, 5, 6) products. Clearly, these backward products are not rotationally hot. These results are quite different from that at the collision energy of 2.0 kcal/mol, in which the translational energy distributions in the forward and backward directions are overall similar. From the above analysis, it is not difficult to draw the conclusion that the extra backward OD products appearing at higher collision energy are likely vibratioanlly hot ($v = 4$, 5, 6) and rotationally cold, which is typical of a collinear abstraction mechanism. This result indicates that the abstraction pathway for the $O(^1D) + H_2$ reaction at higher collision energies is clearly due to a collinear abstraction mechanism through the excited state surface [75].

4.4. *Quantum state specific dynamics for the $O(^1D) + HD \rightarrow OD + H$ reaction: isotope effects*

The $O(^1D) + HD$ reaction was also studied using the same Rydberg tagging TOF technique described above. The experiment was carried out at the collision energy of ~1.7 kcal/mol, which is below the 1.8 kcal/mol barrier inferred for the abstraction

mechanism from previous experimental studies [69]. The purpose of this experimental study is to investigate the isotope effect on this reaction [76].

Time-of-flight spectra of the H-atom products have been measured at many laboratory angles (from 117.5° to −60° at 10° intervals). The laboratory angles at which the TOF spectra are shown are indicative of forward (−60°), backward (117.5°) and sideways scattering (30°). The direction of the HD beam is $\Theta_L = 0°$, while the direction of the O(^{1}D) beam is $\Theta_L = 90°$. By definition in this work, the forwardness and backwardness for the H-atom products are with respect to the HD beam direction, while those for the OD products are with respect to the O(^{1}D) beam direction. From these TOF spectra, it is quite clear that these spectra consist of a lot of sharp structures. These sharp structures correspond to the rovibrational structures of the OD products. Most of these structures are overlapped structures by different OD rovibrational states. Spin–orbit states were not resolved in these TOF spectra. By directly converting these TOF spectra from the laboratory frame to the centre-of-mass frame (CM) including the standard Jacobian transformation, the product translational energy distributions at different CM scattering angles of the title reaction can be obtained. Figure 31 shows the translational energy distributions obtained from the experimentally measured TOF spectra. Since the centre-of-mass angles are not constant for a certain laboratory angle at different product (H) velocities, each of the translational energy distributions obtained from the three different laboratory angles contains information in a range of CM angles. However, the three translational energy distributions still carry the basic information on forward, backward and sideways scatterings.

The available energy of the title reaction is about 45 kcal/mol, which can produce OD radical product up to $v = 6$. From figure 31(a), the energetic limits of different vibrationally excited OD products are indicated. The peaks shown in the translational energy distribution in figure 31(a) at these energetic limits are rotationally cold OD products in different vibrationally excited states. In principle, angular distributions can be obtained for the OD product in different rovibrational states by careful simulations of the translational energy distributions at different laboratory angles. This type of analysis takes an enormous amount of time, and work in this direction is under way. Even though angular distributions for each rovibrational state are not available yet, important dynamical information on this reaction can still be derived from the translational energy distributions at typical scattering angles. From figure 31, one can see that the rotationally cold OD products are more pronounced in the forward and backward scattering directions than that in the sideways scattering direction with respect to the O(^{1}D) beam direction. While almost all OD products in the sideways scattering direction are rotationally hot, both cold and hot OD products are present in both the forward and backward directions even though hot OD products are still more important. Over all, it is not difficult to see that most of the OD products for the title reaction are rotationally hot, while a small number of OD products are rotationally cold and are mainly scattered in the forward and backward directions with respect to the O(^{1}D) beam direction.

The total product angular distribution of the H-atom product in this reaction is roughly forward–backward symmetric. The total products at the backward direction are slightly more pronounced than that at the forward direction, indicating that the forward–backward scattering for the $O(^1D) + HD \rightarrow OD + H$ might not be exactly

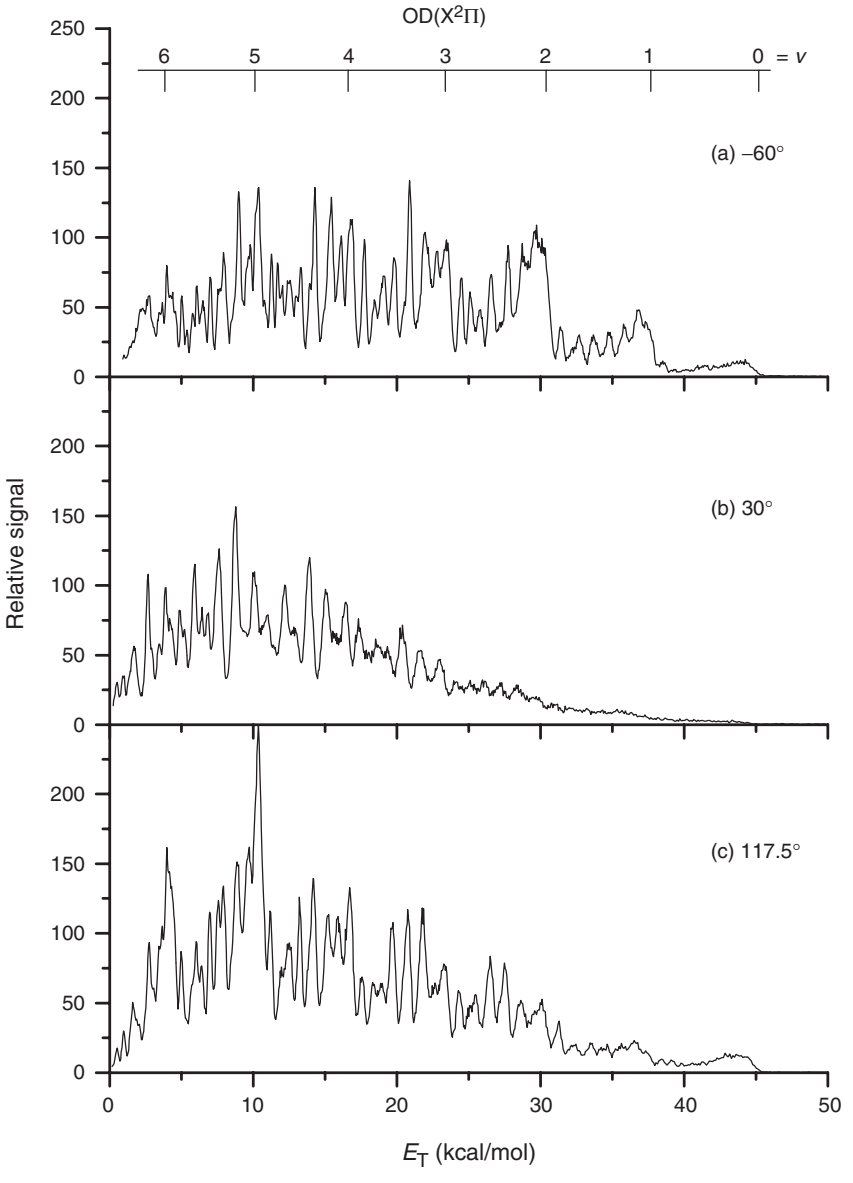

Figure 31. The CM product translational energy distributions at the (a) forward (−60°), (b) sideways (30°) and (c) backward (117.5°) scattering direction for the $O(^1D) + HD \rightarrow OD + H$ reaction at the collision energy of 1.7 kcal/mol.

symmetric even though the collision energy of this reaction is below the reaction barrier for the abstraction channel. This means that the insertion reaction does not necessarily produce forward–backward symmetric product angular distribution. In this reaction, since HD is not exactly symmetric, therefore the interaction with H and D might not be exactly the same. From the angular resolved translational energy distributions, it is

clear that the total translational energy distribution or the OD product state distribution is also not forward and backward symmetric. In reality, there are actually significant differences between the forward and backward translational energy distributions. Since exact simulation is not available yet, a full-fledged comparison between theory and experiment is not realistic at this time. From figure 30, it is obvious that the product state distribution for the rotationally cold OD product is quite asymmetric. For $v=0$ of OD, the rotationally cold peak in the forward direction (-60°) is roughly the same as that in the backward direction, indicating that the rotationally cold OD products for $v=0$ are roughly forward and backward symmetric. For rotationally cold OD($v=1$) products, the forward and backward scatterings are clearly not symmetric. With respect to the O(^{1}D) beam direction, the OD($v=1$) products in low rotational levels are clearly forward scattered, and the OD($v=2$) products in low rotational levels are even more forward scattered. For $v=3$, the OD products in low rotational levels are still forward scattered, but less so than the OD($v=2$) products. For $v=4$, the OD product peak height in low rotational levels is similar for forward and backward scattering directions, indicating the OD($v=4$) products in low rotational levels are roughly forward–backward symmetric. For $v=5$, however, the OD products in low rotational levels are clearly backward scattered with respect to the O(^{1}D) beam, in which the corresponding peak in the backward direction is significantly more than that in the forward scattering direction. Similarly, the $v=6$ OD products in low rotational excitation is also backward scattered. The above experimental observations are quite striking in which the OD rotationally cold products undergo forward-to-backward scattered angular distributions. The underlying dynamics responsible for these interesting experimental observations are not immediately clear for the O(^{1}D) + HD reaction since such phenomena have not been observed for the O(^{1}D) + H_2 reaction. Much theoretical work is needed to understand the nature of this interesting phenomenon.

5. The H + H_2 reaction: structure and dynamics of the quantized transition states

Extensive studies on the H + H_2 system have been performed both experimentally [9, 11, 77–79] and theoretically [80–86]. Even though this is the simplest chemical reaction in nature, many of the interesting and also important questions involved in this system have never been clearly answered. One of the most outstanding questions is the existence of the dynamical resonances in this reaction. Experimentally, a few attempts to observe the dynamical resonance effect in this reaction have largely failed. Theoretically, the existence and the nature of such resonances have never been clarified. In this work, the H + HD(D_2) → H_2(HD) + D reaction was studied experimentally in our laboratory using the Rydberg tagging technique, in close collaboration with the theoretical calculations by Skodje, with the hope of trying to answer some of these intriguing questions for this system.

The experimental apparatus employed in this study is the same as that used in the study of the O(^{1}D) + H_2 reaction in the last section [87, 88]. The only significant difference is the H beam source which is generated from HI photodissociation while the O(^{1}D) atom beam described in the previous section is generated from

O_2 photodissociation. Briefly, two parallel molecular beams (HI and HD or D_2) are generated with similar pulsed valves in this experiment. In the reaction of H + HD, the H-atom beam is produced by the photolysis of the HI molecule at 266 nm using Nd:YAG fourth-harmonic laser output. There are two different photolysis channels, corresponding to the two spin–orbit states of the iodine atom, which gives rise to two sharp peaks of the H-atom velocity distribution: a fast component at 17 470 m/s and a slow component at 11 230 m/s. The H beam is then crossed at 90° with the HD molecular beam. The HD beam was produced by an adiabatic expansion through a nozzle cooled to liquid nitrogen temperatures with almost all of the HD molecules in the $j=0$ level. Using the slow and fast H atoms separately in the reactive scattering experiment with HD, two collision energies are obtained, $E_c = 0.498$ and 1.200 eV, respectively. The experimental results obtained at these two collision energies are described in the following paragraphs. In the reaction of $H + D_2$ described below, a tunable wavelength photolysis laser is used to generate the H-atom beam with variable speed. This allows us to study the dynamics of this reaction at different collision energies.

5.1. *State-to-state dynamics of the H + HD reaction at E_{coll} = 0.498 eV and 1.200 eV*

Time of flight spectra of D atoms at different laboratory scattering angles were measured using the technique described above at the collision energy of 0.498 eV for the title reaction [89]. These TOF spectra were then converted to the product translational energy distributions using a home-written LAB–CM conversion program. Figure 32 shows four such typical distributions. There are many sharp structures in these distributions which can be assigned to different H_2-product rotational states from the H + HD reaction. From these distributions, relative rotational-state-resolved differential cross-sections can be determined. Experimental apparatus functions were used to correct the detection efficiency at different detection time-delays and laboratory angles. These corrections are essentially the same as the method used by Schnieder *et al.* [11] The experimental differential cross-sections for the H_2 ($v=0, j'$) product obtained are presented in figure 33(a) along with the theoretical values. All experimental results in figure 33(a) are scaled to the theoretical value using one scaling factor for all different product states. State-specific integral cross-sections (ICS) have also been determined by integrating the differential cross-section (DCS) data in figure 33(a), and are shown in figure 33(b). Clearly the experimental results show that all H_2 products are backward scattered relative to the H-atom beam direction. Another interesting observation is that the state-specific integral cross-sections of H_2 ($v=0, j'$) oscillate quite significantly. Clearly, this oscillation follows the $H_2(j')$-product nuclear spin statistics. Therefore, the H_2-product rotational-state distribution seems to be dramatically affected by the H-atom nuclear spin statistics. This result is similar to that of the H + HI reaction studied by Zare *et al.* [90]

The title reaction has also been investigated at the collision energy of 1.200 eV using the faster H-atom component generated by the HI photolysis at 266 nm. TOF spectra of the D-atom at many different laboratory scattering angles were measured using the technique described above at the collision energy of 1.200 eV. These TOF spectra can be converted to the product translational energy distributions using the same

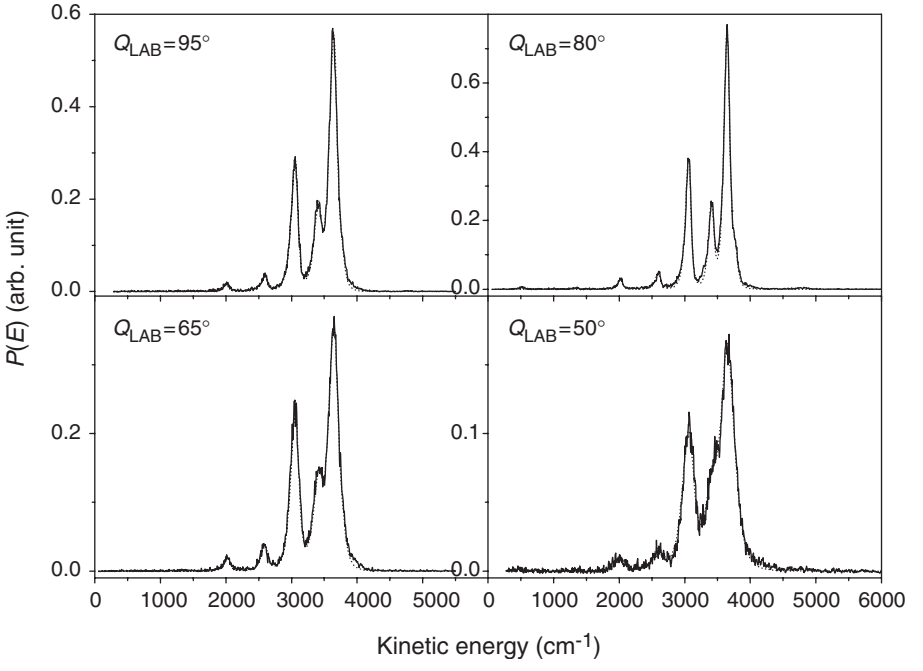

Figure 32. The product translational energy distributions measured at different laboratory angles for the $H + HD \rightarrow H_2 + D$ reaction at the collision energy of 0.5 eV.

LAB–CM conversion program. figure 34 shows six typical product translational energy distributions converted in the backward and sideways scattering directions. There are many sharp structures in these distributions which can be assigned to different H_2-product rovibrational states from the H + HD reaction. In addition to the backward and sideways scattering, we have also measured scattering products in the forward scattering direction, which is very hard to measure because of the unfavourable kinematics and also signal attenuation due to the HI beam. Nevertheless, great efforts have been devoted to forward scattering product detection. TOF spectra at several laboratory angles in the forward scattering direction have been measured. Figure 35 shows the D-atom TOF signal at -58° for the $v = 0$ H_2 product in the forward direction. From experimental results, relative quantum state-resolved differential cross-sections can be determined. Experimental apparatus functions on a realistic experimental model are used, as discussed above, to correct the detection at different detection time-delays and laboratory angles. The three-dimensional experimental differential cross-sections obtained for the H_2 ($v = 0, j'$) products are presented in figure 36 [91, 92]. All experimental results are scaled to the theoretical value using one scaling factor for all the different product states. Rovibrational state specific integral cross-sections (ICS) for the H_2 ($v = 0$) products have also been determined by integrating the DCS data in figure 34 and are shown in figure 37.

The experimental results show that all H_2 products are more backward and sideways scattered relative to the H-atom beam direction. In addition to the backward and sideways scattering, there is a narrow forward scattering peak for the $v = 0$ H_2 product.

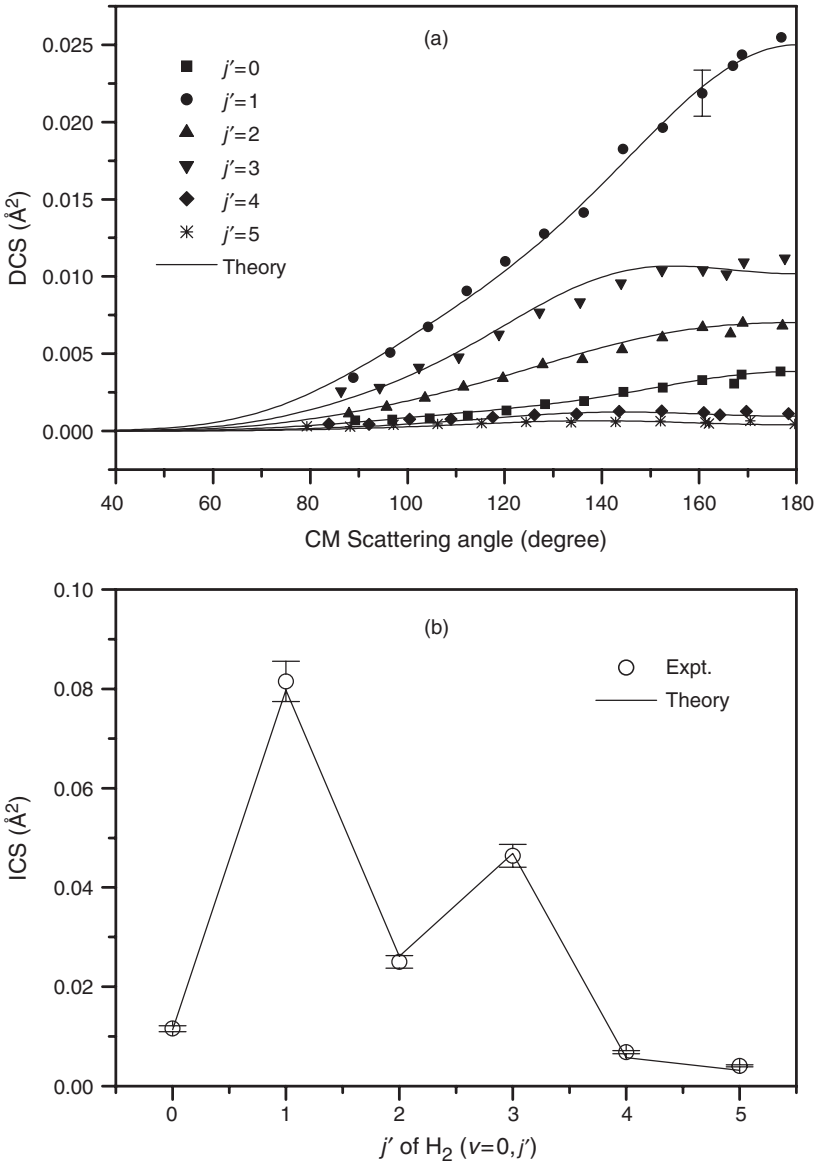

Figure 33. The differential cross-sections and the state-specific integral cross-sections for the $H + HD \rightarrow H_2 + D$ reaction at the collision energy of 0.5 eV.

The simulations show that the $v = 0$ H_2 forward peak is attributed to predominantly low rotationally excited H_2 products ($j' = 0$, 1 and 2). This is in contrast to the backward and sideways scattering products which are significantly more rotationally excited with averaged rotational quantum number $j' \sim 5$. This observation is rather peculiar because the product state distributions in the forward and backward scattering directions are significantly different from each other, indicating that the reaction dynamics

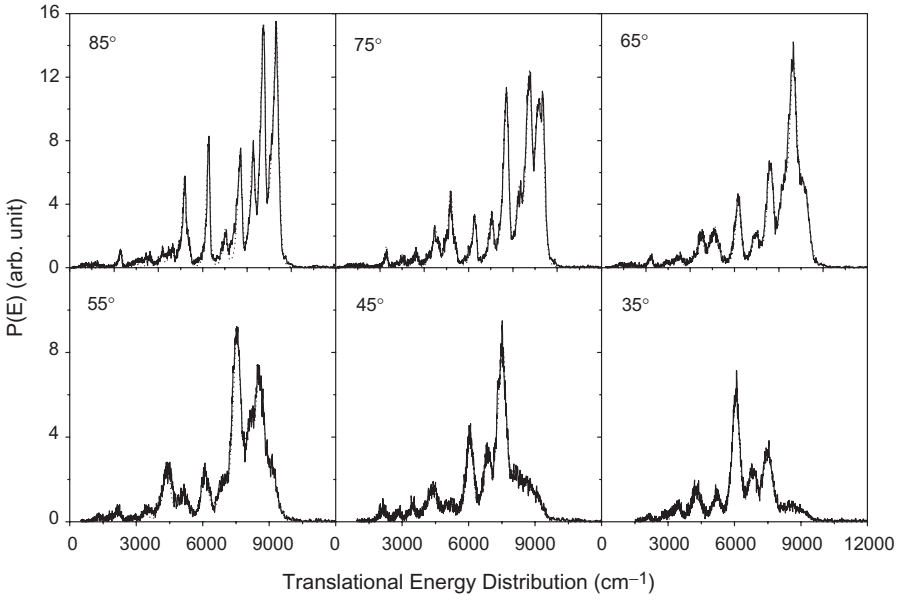

Figure 34. The product translational energy distributions measured at different laboratory angles for the $H + HD \rightarrow H_2 + D$ reaction at the collision energy of 0.5 eV.

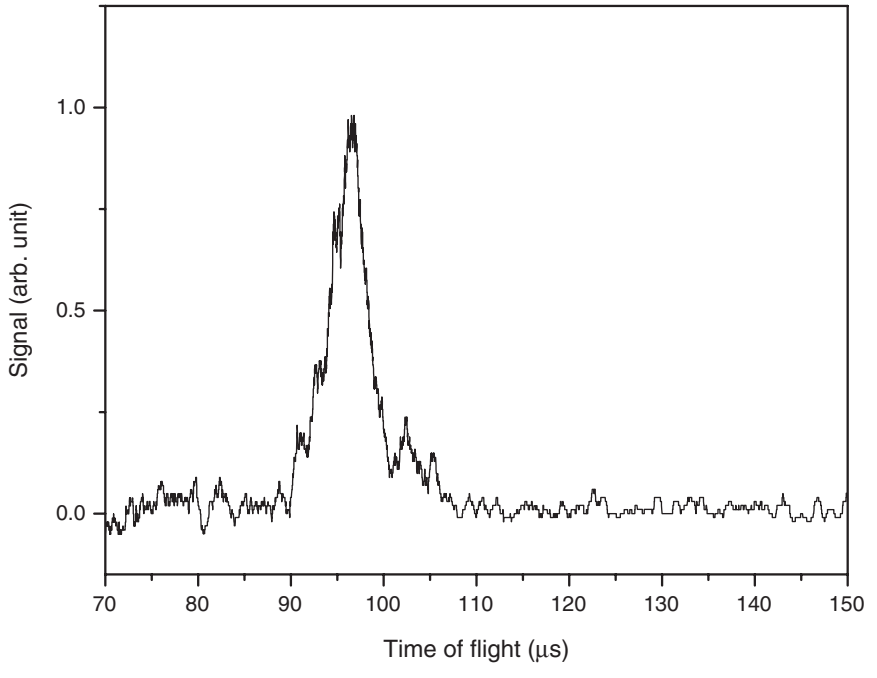

Figure 35. The D atom TOF spectrum at the forward scattering direction ($\Theta_L = -58°$) for the $H + HD \rightarrow H_2 + D$ reaction at the collision energy of 1.200 eV.

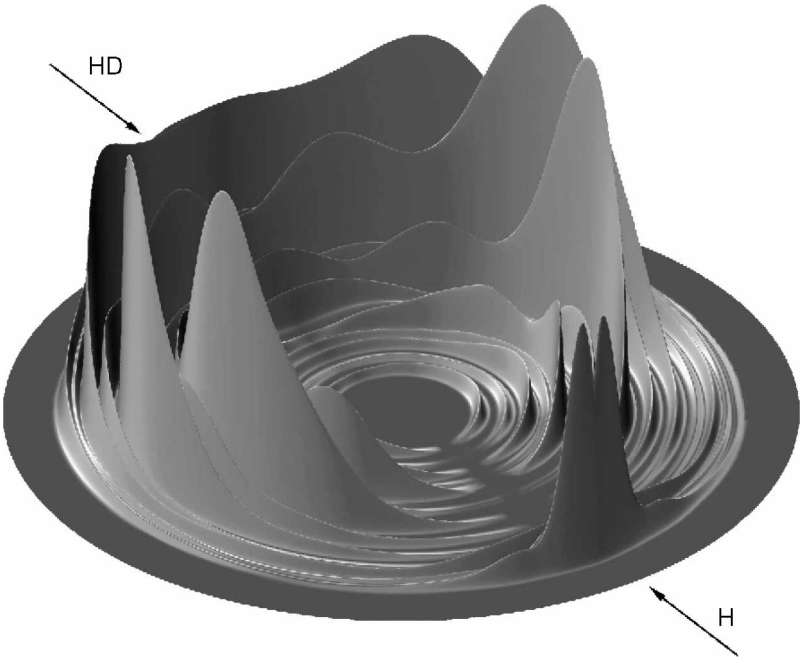

Figure 36. The three-dimensional plot of the differential cross-sections for the $H + HD \rightarrow H_2 + D$ reaction at the collision energy of 1.200 eV (detecting the D atom product).

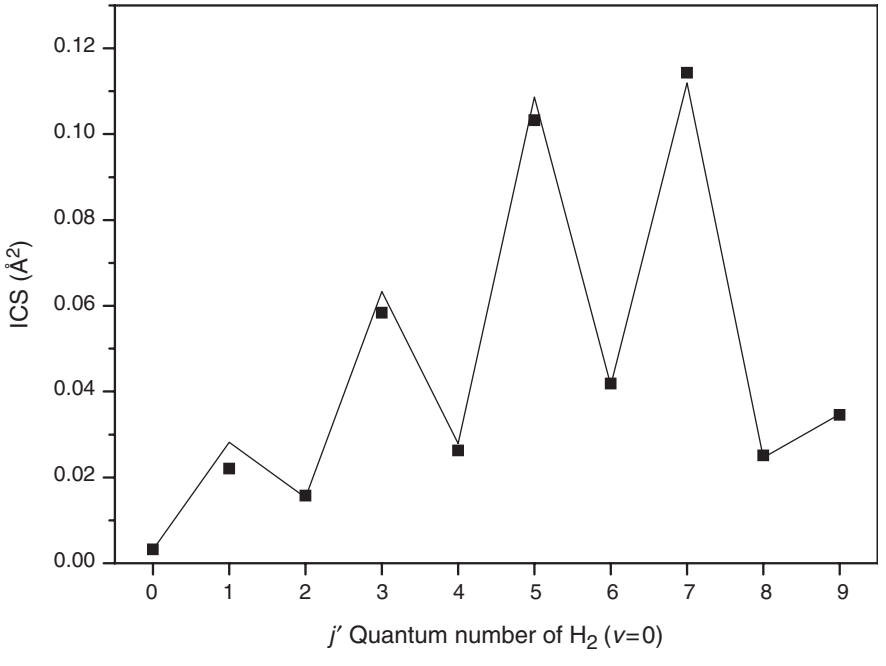

Figure 37. The state-specific integral cross-sections for the H_2 ($v = 0$) product from the $H + HD \rightarrow H_2 + D$ reaction at the collision energy of 1.200 eV.

responsible for the forward scattering products are unique. In figure 36, state-specific DCSs for high j' H_2 products show some significant angular oscillations. As j' increases, there are actually multiple oscillations. This phenomenon has also been observed in the $H + D_2$ reaction by Schnieder *et al.* [11]. However, the nature of these angular oscillations has not been clearly addressed in previous theoretical investigations. Furthermore, state-specific integral cross-sections (figure 37) of H_2 ($v = 0, 1, j'$) at this collision energy oscillate more dramatically than that at the lower collision energy, which is attributed to the nuclear spin statistics.

One of the most interesting observations in this experiment is the forward scattering, similar to the forward scattering observed in the $H + D_2$ reaction at higher collision energies [95]. The characteristics of the forward scattering H_2 products are unique. Firstly, it is clear that the forward scattering H_2 products are significantly colder rotationally, with mainly H_2 ($j = 1$) populated, than the backward and sideways scattering products. Secondly, the angular range of the observed forward scattering peak is extremely narrow. Experimental characteristics of the forward scattering peak including the rotational distribution and angular width can be readily reproduced by quantum calculations. However, to assign the forward peak to specific dynamical behaviour requires further theoretical analysis.

In order to understand the detailed dynamics observed for this reaction, especially the forward scattering, quantum reactive scattering calculations (QM) were carried out based on the BKMP2 PES [93] by Skodje. State-specific integral cross-sections and differential cross-sections were obtained from these calculations. From the scattering calculation, the state and angle resolved integrated opacity function is computed, i.e. $d\sigma J_{max}(0,\ 0 \rightarrow 0,\ 0;\ \theta = 0)/d\Omega$ versus J_{max}, where the DCS is the partial sum of waves with $J \leq J_{max}$, J being the total angular momentum. This analysis shows that the forward peak in the H_2 ($v' = 0$) product for $E_c = 1.200$ eV is dominated by the contribution from just several partial waves near $J = 25$, while for the H_2 ($v' = 1$) product the dominant contribution occurs near $J = 21$. The narrow ranged, high J collisions responsible for the forward scattering implies that the reaction intermediate is formed at very high impact parameter and should rotate quite rapidly. To further probe the dynamics associated with the forward peak, a time-delay analysis was carried out using the concept of the angle-resolved scattering time-delay proposed by Goldberger and Watson [94]. An extra $\sim$20 fs of time-delay in the forward direction, similar to the result obtained by Althorpe *et al.* [95] is clearly seen compared to other scattering angles. This clearly shows that the forward scattering product results from a time-delayed mechanism.

Since the forward peak is clearly from high J collisions, it is clearly produced via a rapidly rotating intermediate exhibiting an enhanced time-delay. Further insight into the associated dynamics is provided by a classical trajectory simulation by Skodje. The forward peak results from collisions that the H atom attacks on the HD-diatom sideways (see figure 38). At the point where the transition state region is first reached, the collision complex is already oriented about 70° relative to the centre-of-mass collision axis. The intermediate then rotates rapidly with an angular frequency of $\omega \sim J/I$, where I is the moment of inertia of the intermediate. If the intermediate with a time-delay of the order of the lifetime τ, the intermediate can rotate an additional amount $\Delta\theta = \omega\tau$, or about 50° for a 20 fs time-delay. Since the intermediate is expected

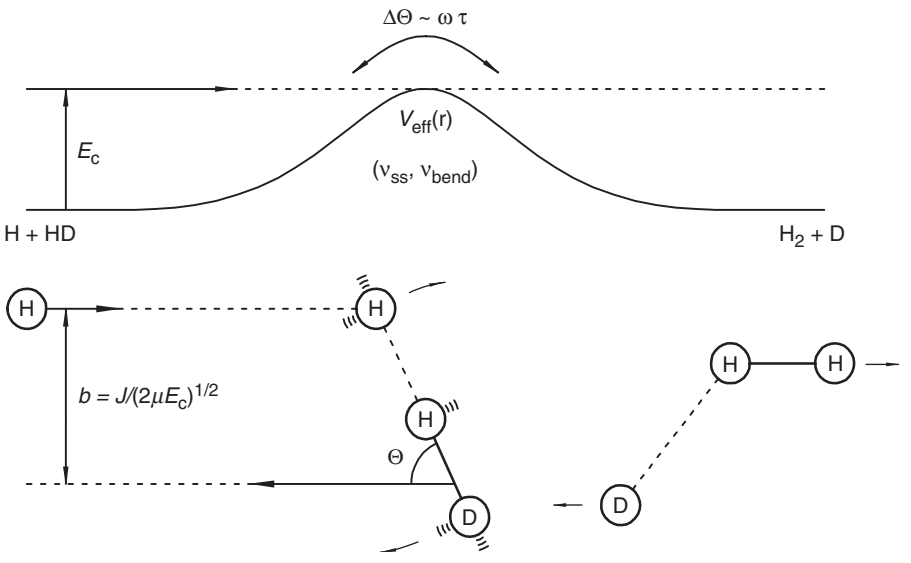

Figure 38. Reaction mechanism for the forward scattering product from the $H + HD \rightarrow H_2 + D$ reaction at the collision energy of 1.200 eV.

to decay exponentially, $e^{-t/\tau}$, there will still be a significant probability density at $t = 2.2\,\tau$ which can take the product into the forward direction. Consistent with this simple picture, we have found that the smallest scattering angles consistently show the longest time-delays, both classically and quantum mechanically.

The next interesting question, of course, is the physical origin of the time-delay in the transition state region for the forward scattering products. Using the centrifugally shifted Hamiltonian, $H(J) = H(0) + \hbar^2 \hat{J}^2 / 2\mu R^2$, with R being the H–HD distance, the theoretical spectra of quantized bottleneck states and the wavefunctions of the bottleneck states [96–99] have been obtained using the spectral quantization technique. A quantized bottleneck state is clearly identified at exactly the collision energy ($E_c = 1.200$ eV) of this experiment.

In the above analysis, we have shown that the forward scattering in the $H + HD \rightarrow H_2 + D$ reaction is clearly produced via a time-delayed mechanism, similar to that for the $H + D_2$ reaction, that is somehow related to a quantized bottleneck state. Generally, a time-delay in the transition state region could be caused by different mechanisms, i.e. (a) via a Feshbach resonance state trapped in an adiabatic potential well as in the $F + HD \rightarrow HF + D$ reaction, or (b) via a quantized bottleneck state in which the time-delay results from the slow-down of the motion of the intermediate near the top of the adiabatic reaction barrier rather than trapping, during which a few vibrations take place in the coordinates perpendicular to the reaction coordinate. The distinction between these two types of mechanisms and, in fact, the existence of quantized bottleneck states as a distinct category of quasi-bound state has only become clear in recent years [99, 100]. The spectral quantization method shows that no clear Feshbach resonance state is present in the centrifugally shifted vibrationally adiabatic potentials in the $H + HD \rightarrow H_2 + D$ system near the energy of the experiment;

on the other hand our results show clearly that the collision energy ($E_c = 1.200$ eV) in this experiment is nearly resonant with the energy of a quantized bottleneck state for the $J = 25$ collisions predominantly responsible for the forward scattering. Therefore all analyses indicates that the time-delay mechanism observed in the forward scattering is produced via the slow-down of the intermediate's motion near the top of the barrier of the specific quantized bottleneck state at about $E_c = 1.2$ eV. It is obvious that this mechanism is significantly different from the Feshbach resonance mechanism in which trapping occurs in an effective potential well. However, there are also similarities between the two mechanisms. In the Feshbach resonance mechanism, the collision energy (E_c) has to be resonant with the trapped resonance state. Similarly, in the time-delayed mechanism via a quantized bottleneck state, the collision energy (E_c) has also to be resonant with the quantized bottleneck state, i.e. the barrier height. The quantized bottleneck state responsible for the time-delay is also an interesting issue. Theoretical analysis shows that the wavefunction of the quantized bottleneck state has one node in the symmetric stretch and two nodes along the bending coordinate, corresponding clearly to a quantized bottleneck state with one quantum of symmetric stretch excitation and two quanta of bending. This barrier state is a mixed state of two adiabatic barrier states with $(v_{ss},\ v_{bend}) = (1, 0)$ and $(0, 2)$. It is also interesting to point out here that a quantized bottleneck state could essentially affect the reaction dynamics in a similar way (producing forward scattering) to a trapped Feshbach resonance state as in the $F + HD \rightarrow HF + D$ reaction [104]. Such a mechanism should also play an important role in many chemical reactions with barriers at high collision energies.

5.2. *Probing the structures of quantized transition states in the H + D_2 reaction*

The concept of the transition state is essential to our view of the dynamics of chemical reactions as well as to chemical reaction rate theory. In a chemical reaction, the transition state acts as a bottleneck to reaction so that incident reagent flux below the transition state energy is reflected, while above the transition state energy it is transmitted to products. In practice, transition state theory is based on the existence of rovibrational quantum states of the collision complex lying near the maxima of effective potential barriers [98]. Despite the crucial importance of the quantum bottleneck state (QBS) to the framework of chemical reaction dynamics, they have proven quite elusive to direct experimental observation. Recently, the quantum dynamics near the transition state has been investigated in 'half-collision' experiments using the methods of transition state spectroscopy [101] and photodissociation spectroscopy [102]. In particular, the recent work of Moore and coworkers [102] on the laser photolysis of the ketene molecule in a cold jet environment revealed step-like structures in the rate for $C_2H_2O + h\nu \rightarrow CO + CH_2$ as the deposited energy passed through threshold values. However, the suggestion in that work that the steps were associated with the energies of the QBS was cast into doubt by strong disagreement with theoretical results [103]. In a full collision experiment, appropriate to bimolecular reactions, direct observation of quantized states in the transition state region is even more difficult. The core problem is that the impact parameter averaging in a crossed beam scattering experiment smears the bottleneck energies over a large range, making them very difficult to identify in

observables. In order to partly undo the effects of impact parameter averaging, it would be very helpful to carry out angle and state-resolved measurements [95, 104, 105] at different collision energies. In this section, the recent results of a new experiment on the $H + D_2 \rightarrow D + HD$ reaction [106–109] and the results of theoretical simulations are described here to demonstrates the influence of QBSs in a full collision environment.

In order to observe the effects of quantized transition states in a reactive collision on the reaction dynamics, it is essential to accurately measure the reactive cross-sections as a function of variable collision energy, E_c. In the previous part on the $H + HD \rightarrow H_2 + D$ reaction, we have measured the state-to-state differential cross-section at two isolated collision energies with a crossed molecular beam apparatus using a HI-photolysis source for the H-atom beam using fixed laser frequencies. In the experiment on the related $H + D_2 \rightarrow D + HD$ reaction [110], we have modified our previous experimental design to permit the use of a tunable photolysis laser to generate the H-atom beam with variable speed, which thus allows the continuous variation of E_c. Except for the photolysis source, the present experiment is similar to the experiment described in the last sections. Two parallel molecular beams (HI and *ortho*-D_2) are generated with pulsed valves. The *ortho*-D_2 beam was produced by an adiabatic expansion through a nozzle cooled to liquid nitrogen temperature, which ensures that almost all molecules in the beam are in the D_2 ($v = 0$, $j = 0$) state [111]. The H-atom beam is produced by HI-photolysis using a tunable, narrow-band doubled dye laser output. By varying the laser frequency, centre-of-mass (CM) collision energies in the range $E_c = 0.4$–$1.0\,\text{eV}$ were obtained with a spread estimated to be about $\Delta E_c = 10\,\text{meV}$. The reaction products were monitored using the same hydrogen Rydberg atom time-of-flight technique described above. The TOF spectra of D atoms at different E_c were measured using this method and then converted to the CM translational energy distribution. Sharp structures are observed in the TOF spectra at different E_c, which can be assigned to HD-product rovibrational states, which then yield relative quantum state-specific DCSs. Experimental error bars on the DCSs are about $\pm 10\%$ or less. The experimental design, which could monitor conveniently the H-atom beam intensity *in situ*, allows the measurement of absolute DCSs up to a single overall scaling factor for all energies and, thus, all product states. The D-atom TOF spectrum was measured at 19 energies in the same (nearly) backward scattering direction at the laboratory angle of 70°, corresponding to CM angles around 160° for $H + D_2$ ($v = 0$, $j = 0$) $\rightarrow$ HD ($v = 0$, $j' = 2$) + D. Eight typical translational energy distributions at different collision energies, obtained from the measured D-atom TOF spectra, are shown in figure 39. The measured DCS at $\Theta_{LAB} = 70°$ for the HD ($v = 0$, $j' = 2$) products at different collision energies, which were clearly resolved in the TOF spectra, are shown in figure 40. Three oscillations in the measured DCSs are clearly apparent over the energy range considered. Similar oscillations are also observed for other final states. The observation of this oscillation is very intriguing since the nature of such structures has not been clearly characterized theoretically despite their obvious importance in the understanding of fundamental reaction dynamics in this benchmark system.

In order to clarify the nature of these oscillations, the dynamics for $H + D_2 \rightarrow D + HD$ has been theoretically modelled using a fully converged coupled channel scattering calculation that employed the highly accurate BKMP2-PES [112]. These computations produce the *S*-matrix from a coupled-channel calculation

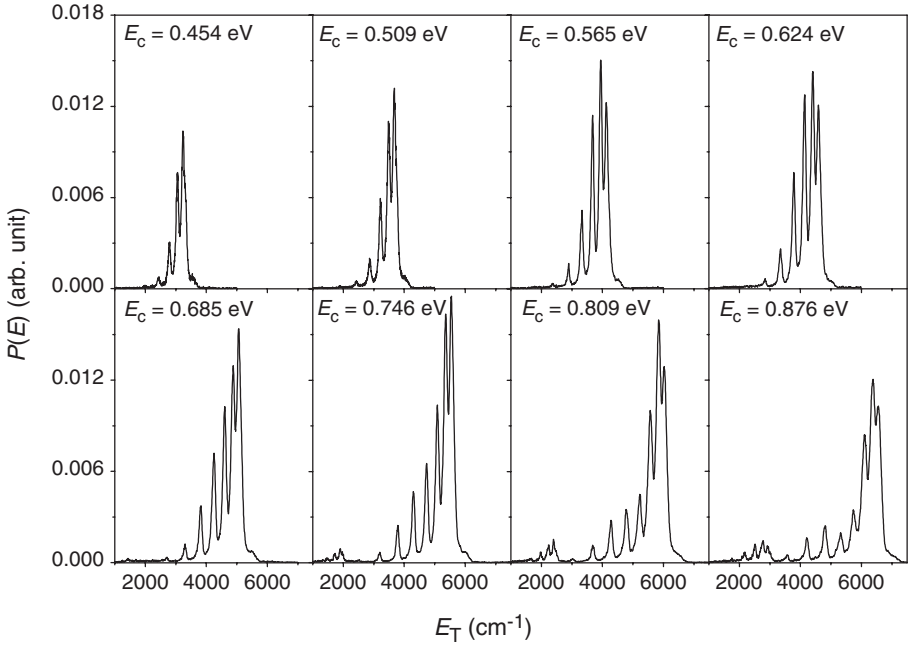

Figure 39. Typical translational energy distributions for $H + D_2$ ($v = 0$, $j = 0$) $\rightarrow$ $D + HD$ (v', $j' = 2$), which were obtained from the measured D-atom TOF spectra, at nine different collision energies.

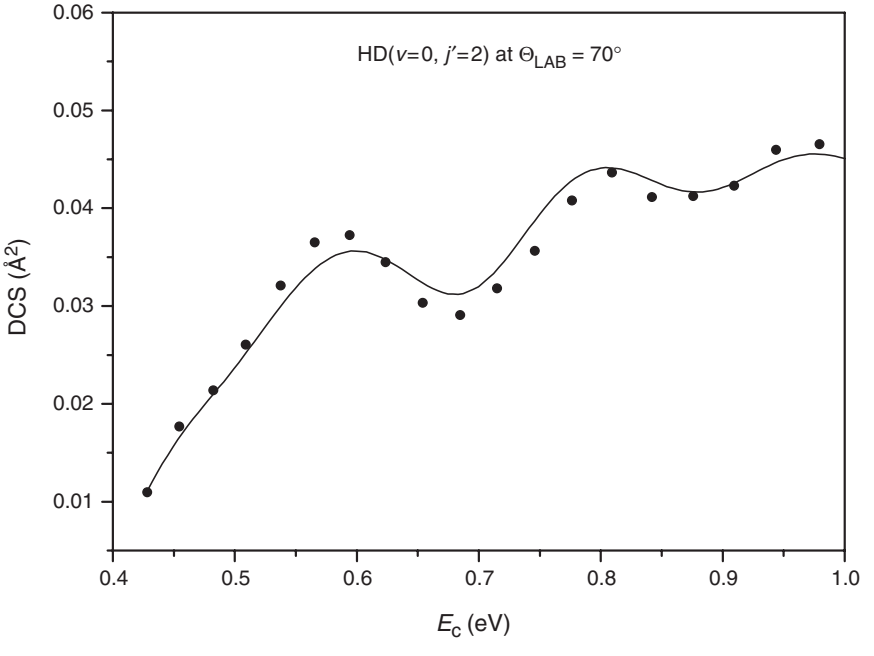

Figure 40. The experimental differential cross-section (dots) for $H + D_2$ ($v = 0, j = 0$) $\rightarrow$ $D + HD$ ($v' = 0, j' = 2$), measured at the laboratory angle of 70°, versus CM collision energy, E_c. The curve is the result of the quantum scattering calculation.

in a hyperspherical coordinate system [113–117] using a partial wave expansion up to total angular momentum $J = 32$ on a grid of 90 total energies (including zero-point) from $E = 0.5$ to 1.6 eV. The details of the calculations have been presented elsewhere, and it is sufficient to note that the state-to-state DCS and ICS converge with respect to basis set size and propagation steps. As seen in figure 40, the experimental DCS at $\Theta_{LAB} = 70^\circ$ ($\Theta_{CM} \approx 160^\circ$) for $H + D_2\ (0,0) \rightarrow HD\ (0,2) + D$ is well reproduced by theory. The agreement between theory and experiment provides an excellent check that the theoretical model used is accurate and reliable as the basis for further analysis.

Using the accurate theoretical model, the physical origin of the intriguing oscillatory structure of the DCS can be traced. One striking feature that emerges from the scattering calculations is the occurrence of very strong oscillations in the *S*-matrix elements versus *E*. A similar oscillation in $P_R(v, j \rightarrow v', j'; E)$ has been computed for other isotopic combinations of this reaction [118], but it is most pronounced in the present case. The oscillatory structure taken as a function of *J* reveals that the 'peak' positions progressively shift to higher energy with increasing *J*. This '*J*-shifting' of features in P_R versus *J* is a well-known manifestation of impact parameter averaging and leads to the energy smearing of features, such as resonance energies, in collision experiments. Indeed, when the partial waves are combined to form the cross-sections, $\sigma_R(v, j \rightarrow v', j'; E)$, the oscillations are generally averaged out. The situation is clearly different for the DCS. As shown in figure 40, the oscillatory structures in the backward (i.e. rebound) direction appear much more strongly than the corresponding structures in the ICS. The reason is that the angle selection suppresses the impact parameter averaging allowing the strong oscillation of the individual *S*-matrix elements to persist in the final observable. Therefore, detecting backward scattering products at low rotational excitation is 'selectively' probing reactive products from collisions with a reduced range of small impact parameters.

While it is now clear that the oscillation in the DCS is the result of an underlying oscillation in P_R, it still remains to explain why P_R oscillates in the first place. In previous discussions of the $H + H_2$ reaction family, there is occasional reference to such structures as resonance peaks, although a systematic assignment has not appeared. However it does not appear that this simple identification is tenable. Using the spectral quantization method [119] we computed all the localized quantum states for $E_c < 1.2$ eV, and we have found that all the relevant lowest energy states can be assigned to the QBSs: $E_c(0, 0^0) = 0.41$ eV, $E_c(0, 2^0) = 0.59$ eV, and $E_c(1, 0^0) = 0.71$ eV, all for $J = 0$. While the QBSs are sometimes referred to as 'barrier resonances', this nomenclature is controversial precisely because P_R does not show resonant peaks. Moreover, the peak positions [117] are out of phase for the various transitions ($v, j \rightarrow v', j'$), whereas resonance peaks should appear at nearly the resonance energy. Finally, the amount of *J*-shifting of the peaks is inconsistent with a progression of rotationally excited resonance states. Even though the oscillations are not resonance peaks *per se*, they are intimately connected to the QBSs. It appears that the energy-dependent oscillation observed in the experiment is an interference effect somewhat similar to Stuckelberg oscillations [120] familiar from atomic physics. The correlation diagram shown in figure 41(a) provides a simple view of the reaction dynamics. The QBSs near the saddle point are correlated along the reaction coordinate to the asymptotic rovibrational states through vibrationally adiabatic potential curves [103]. Significant coupling

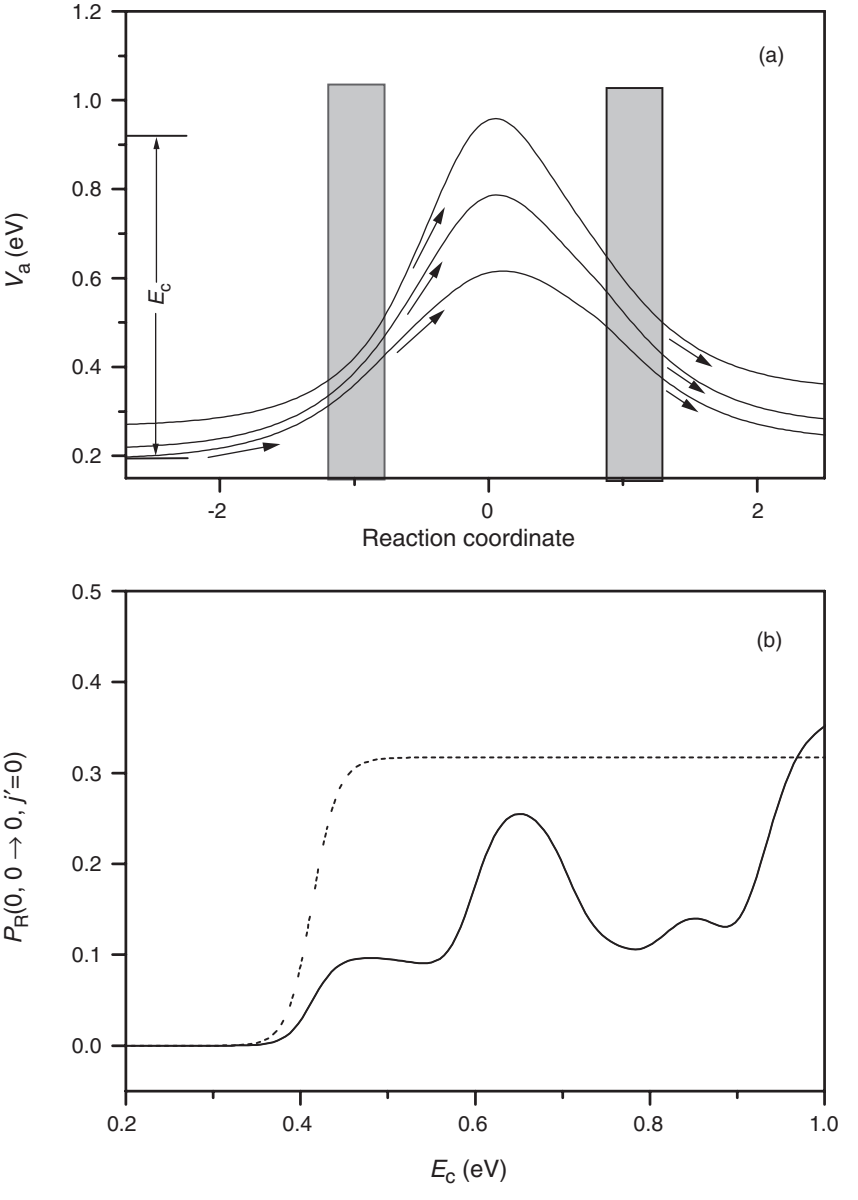

Figure 41. (a) Schematic correlation diagram illustrating the role of quantized bottlenecks on the reaction dynamics. Because of non-adiabatic coupling in the entrance channel (shaded area), flux in a given initial state will pass the transition state through several bottleneck states. Non-adiabatic coupling in the exit channel (shaded area) will further mix the reactive flux into the final product states. (b) The state-to-state reaction probabilities, $P_R(0, 0 \rightarrow 0, j'; E)$ versus E_c for $j' = 0$. The solid lines show that the full model, with coupling in both the entrance and exit channels, exhibits the out of phase oscillations observed in the exact dynamics. The dashed lines show the results when the coupling in the exit channel is switched off, which then show only simple threshold behaviour. The essential point is that all physically reasonable models of this form show oscillations qualitatively similar to those observed in the exact calculation.

between the curves occurs in the entrance and exit channels due to, e.g. avoided crossings. Near the saddle point, where the levels are further apart, the dynamics is more uncoupled. As illustrated in the figure, the incident flux in a particular reagent channel, $H + D_2$ (v, j), is redistributed among several neighbouring states due to vibrationally non-adiabatic coupling in the entrance channel. Thus, several QBS thresholds control the reactive flux as it passes the transition state. Similar coupling again scrambles the flux in the exit channel of the reaction. Hence, one expects that each state-to-state reaction probability is affected by a number of QBS pathways, and is formed from the coherent sum of amplitudes corresponding to a variety of pathways as depicted schematically in figure 41(a).

Based on this physical view of the reaction dynamics, a very broad class of models can be constructed that yield qualitatively similar oscillations of the reaction probabilities. As shown in figure 41(b), a model based on Eckart barriers and constant non-adiabatic coupling to mimic $H + D_2$, yields out-of-phase oscillations in $P_R(0, 0 \rightarrow 0, j'; E)$ analogous to those observed in the full quantum scattering calculation. Note, however, that if the re-coupling in the exit channel is omitted (as shown in figure 41(b) with dashed lines) then oscillations disappear and P_R exhibits simple steps at the QBS energies. As the occurrence of the oscillation is quite insensitive to the details of the model, the interference of pathways through the network of QBSs seems to provide a robust mechanism for the oscillating reaction probabilities.

In summary, we have demonstrated that the DCS for the $H + D_2 \rightarrow HD + H$ reaction exhibits pronounced oscillatory structures in the backward scattering direction both in experimental and in theory. The physical origin of these structures can be traced to the opening of a sequence of quantized transition state thresholds.

6. Summary

In this review, we have presented a few examples of quantum state-resolved reactive scattering studies of both unimolecular and bimolecular reactions using the elegant H-atom Rydberg tagging TOF technique. Detailed dynamical information can be gained from these well-controlled experimental investigations. Photodissociation of H_2O at both 157 nm and 121.6 nm has been studied in great detail. From the studies of H_2O at 157 nm, the OH vibrational state distribution was measured. Experimental results here also pointed out the inaccuracies in using the LIF technique to measure the OH vibrational state distributions. Photodissociation of H_2O at 121.6 nm has provided an excellent dynamical case of a complicated, yet direct dissociation process through conical intersections. These experimental investigations have provided a solid ground to test the accuracy of the currently available H_2O potential energy surfaces and to improve these surfaces. The $O(^1D) + H_2 \rightarrow OH + H$ reaction has also been investigated using the Rydberg tagging TOF method. Rotational state-resolved differential cross-sections have been measured for this reaction for the first time. The effect of the reagent rotational excitation on the dynamics of this reaction has also been investigated. The $O(^1D) + D_2 \rightarrow OD + D$ reaction at two collision energies has been studied in order to clarify the nature of the abstraction mechanism. The $O(^1D) + HD \rightarrow OH(OD) + D(H)$ reaction has also been investigated to demonstrate

the interesting isotope effect in the insertion reaction. These measurements provided the most detailed experimental results for this prototype insertion reaction. The simplest neutral chemical reaction in nature, the H_3 system, has also been studied using the H-atom Rydberg tagging method in an effort to clarify some of the important basic concepts involved in this reaction. Through extensive collaboration between theory and experiments, the mechanism for the forward scattering product at high collision energies for the $H + HD$ reaction was clarified, which is attributed to a slow-down mechanism on the top of a quantized barrier transition state. Oscillations in the product quantum state-resolved different cross-sections have also been observed in the $H + D_2$ reaction, which is due to the interference of vibrationally adiabatic transition state pathways. Studies on this simple yet important system have provided clarifications of many important concepts on the structures and dynamics of the quantized state states in chemical reactions. It is important to note that all experimental investigations on these different systems described here are in extensive collaboration with theoretical studies from different research groups in the world. Only through these close collaborations can a clear physical picture of these benchmark systems emerge. The work described here clearly demonstrates the importance of close collaboration between experiment and theory in this field.

Acknowledgements

Most of the research work described here is in extensive collaboration with many outstanding scientists in the field of reaction dynamics. I had extensive collaborations with Prof. Richard N. Dixon, Prof. Xuefeng Yang, and Prof. Marc van Hemert on H_2O photodissociation. Prof. George C. Schatz, Prof. F. Javier Aoiz and Prof. Jean-Michel Launay have provided important insights into the research work on the $O(^1D) + H_2$ reaction. Prof. Rex T. Skodje provided great theoretical support on the $H + HD(D_2)$ work, which clearly takes our understanding of this system to a different level. The experimental work described here was carried out by many students and postdocs in my research group over the last seven years. Here, I want to especially thank Drs. Xianghong Liu, Steve A. Harich, Dennis W. Huang, Jim J. Lin, Dongxu Dai, Mrs. Chia C. Wang and many others who have contributed to the research work described here. This work was supported by the Academia Sinica and the NSC in Taiwan previously, and currently by the Chinese Academy of Sciences and the Ministry of Science of China.

References

[1] E. H. Taylor and S. Datz, J. Chem. Phys. **23,** 1711 (1955).
[2] Y. T. Lee, J. D. MacDonald, P. R. Lebreton, and D. R. Herschbach, Rev. Sci. Instrum. **40,** 1402 (1969).
[3] Y. T. Lee, Science **236,** 793 (1987).
[4] P. Casavecchia, Rep. Prog. Phys. **63,** 355 (2000).
[5] P. Casavecchia, N. Balucani, M. Alagia, L. Cartechini, and G. G. Volpi, Acc. Chem. Res. **32,** 503 (1999).
[6] K. Liu, Ann. Rev. Phys. Chem. **52,** 139 (2001).
[7] D. W. Chandler and P. L. Houston, J. Chem. Phys. **87,** 1445 (1987).
[8] D. H. Parker and A. T. J. B. Eppink, J. Chem. Phys. **107,** 2357 (1997).

[9] L. Schnieder, W. Meier, K. H. Welge, M. N. R. Ashfold, and C. M. Western, J. Chem. Phys. **92,** 7027 (1990).
[10] L.-H. Lai, J.-H. Wang, D.-C. Che, and K. Liu, J. Chem. Phys. **105,** 3332 (1996).
[11] L. Schnieder, K. Seekamp-Rahn, J. Borkowski, E. Wrede, K. H. Welge, F. J. Aoiz, L. Banares, M. J. D'Mello, V. J. Herrero, V. Saez Rabanos, and R. E. Wyatt, Science **269,** 207 (1995); L. Schnieder, K. Seekamp-Rahn, E. Wrede, and K. H. Welge, J. Chem. Phys. **107,** 6175 (1997).
[12] M. N. R. Ashfold, D. H. Mordaunt, and S. H. S. Wilson, in *Advances in Photochemistry*, edited by D. C. Neckers, D. H. Volman, and G. V. Bunau (John Wiley, New York, 1996), Vol. 21, p. 217.
[13] R. N. Dixon, D. W. Huang, X. F. Yang, S. Harich, J. J. Lin, and X. Yang, Science **285,** 1249 (1999).
[14] X. Liu, J. J. Lin, S. A. Harich, G. C. Schatz, and X. Yang, Science **289,** 1536 (2000).
[15] B. R. Strazisar, C. Lin, and H. F. Davis, Science **290,** 958 (2000).
[16] W. A. Chupka, J. Chem. Phys. **98,** 4520 (1993).
[17] A. Ten Wolde, L. D. Noordam, A. Lagendij, and H. B. van Linden van den Heuvell, Phys. Rev. A **40,** 485 (1989).
[18] J. P. Marangos, N. Shen, H. Ma, M. H. R. Hutchinson, and J. P. Connerade, J. Opt. Soc. Am. B **7,** 1254 (1990).
[19] P. Andresen and R. Schinke, in *Molecular Photodissociation Dynamics*, edited by M. N. R. Ashfold, and N. R. Baggott (Royal Society of Chemistry, London, 1987), Chap. 3.
[20] E. Segev and M. Shapiro, J. Chem. Phys. **77,** 5604 (1982).
[21] R. N. Dixon, Mol. Phys. **85,** 333 (1985).
[22] K. Weide and R. Schinke, J. Chem. Phys. **87,** 4627 (1987).
[23] M. P. Docker, A. Hodgson, and J. P. Simons, in *Molecular Photodissociation Dynamics*, edited by M. N. R. Ashfold and J. E. Baggott (Royal Society of Chemistry, London, 1987), Chap. 4.
[24] H. J. Krautwald, L. Schnieder, K. H. Welge, and M. N. R. Ashfold, Faraday Discuss. Chem. Soc. **82,** 99 (1986).
[25] A. Hodgson, Faraday Discuss. Chem. Soc. **82,** 190 (1986); L. J. Dunne, Faraday Discuss. Chem. Soc. **82,** 190 (1986); J. N. Murrell, Faraday Discuss. Chem. Soc. **82,** 191 (1986); M. N. R. Ashfold and R. N. Dixon, Faraday Discuss. Chem. Soc. **82,** 193 (1986).
[26] G. C. Schatz, J. Chem. Phys. **83,** 5677 (1985).
[27] D. H. Mordaunt, M. N. R. Ashfold, and R. N. Dixon, J. Chem. Phys. **100,** 7360 (1994).
[28] X. F. Yang, D. W. Hwang, J. J. Lin, and X. Yang, J. Chem. Phys. **113,** 10597 (2000).
[29] P. Andresen, G. S. Ondrey, B. Titze, and E. W. Rothe, J. Chem. Phys. **80,** 2548 (1984).
[30] K. Mikulecky, K.-H. Gericke, and F. J. Comes, Chem. Phys. Lett. **182,** 290 (1991).
[31] H. Guo and J. N. Murrel, Mol. Phys. **65,** 821 (1988).
[32] V. Engel, R. Schinke, and V. Staemmler, Chem. Phys. Lett. **130,** 413 (1986); J. Chem. Phys. **88,** 129 (1988).
[33] R. Van Harrevelt and M. C. van Hemert, J. Chem. Phys. **114,** 9453 (2001).
[34] D. W. Hwang, X. F. Yang, S. Harich, J. J. Lin, and X. Yang, J. Chem. Phys. **110,** 4123 (1999).
[35] S. A. Harich, X. F. Yang, D. W. Hwang, J. J. Lin, X. Yang, and R. N. Dixon, J. Chem. Phys. **113,** 10073 (2000).
[36] R. N. Dixon, D. W. Huang, X. F. Yang, S. Harich, J. J. Lin, and X. Yang, Science **285,** 1249 (1999).
[37] G. Theodorakopoulos, I. D. Petsalakis, and R. J. Buenker, Chem. Phys. **96,** 217 (1985).
[38] R. Van Harrevelt and M. C. van Hemert, J. Chem. Phys. **112,** 5787 (2000).
[39] A. J. Dobbyn and P. J. Knowles, Mol. Phys. **91,** 1107 (1997).
[40] K. Weide and R. Schinke, J. Chem. Phys. **90,** 7150 (1989).
[41] H. Guo and J. N. Murrell, J. Chem. Soc. Farad. Trans. 2 **84,** 949 (1988).
[42] J. N. Murrell, S. Carter, S. C. Farantos, P. Huxley, and A. J. C. Varandas, *Molecular Potential Energy Functions* (Wiley-Interscience, New York, 1984).
[43] S. A. Harich, X. F. Yang, R. N. Dixon, and X. Yang, Phys. Rev. Lett. **87,** 253201 (2001).
[44] S. A. Harich, X. F. Yang, X. Yang, and R. N. Dixon, J. Chem. Phys. **114,** 7830 (2001).
[45] R. J. Le Roy and W. K. Lui, J. Chem. Phys. **69,** 3622 (1978).
[46] C. H. Lineweaver, Science **284,** 1503 (1999).
[47] R. van Harrevelt, M. van Hemert, S. A. Harich, X. F. Yang, and X. Yang, Phys. Rev. Lett. **87,** 263001 (2001).
[48] G. Anderson, Ann. Rev. Phys. Chem. **38,** 489 (1987), and references therein.
[49] G. Dixon-Lewis and D. J. Williams, Comprehensive Chem. Kinet. **17,** 1 (1977).
[50] P. A. Whitlock, J. T. Muckerman, and E. R. Fisher, J .Chem. Phys. **76,** 4468 (1982).
[51] R. Schinke and W. A. Lester Jr, J. Chem. Phys. **72,** 3754 (1980).
[52] S. W. Ransome and J. S. Wright, J .Chem. Phys. **77,** 6346 (1982).
[53] P. J. Kuntz, B. I. Niefer, and J. J. Sloan, J .Chem. Phys. **88,** 3629 (1988).
[54] G. C. Schatz, A. Papaioannou, L. A. Pederson, L. B. Harding, T. Hollebeer, T.-S. Ho, and H. Kabitz, J .Chem. Phys. **107,** 2340 (1997).
[55] J. E. Butler, R. G. Macdonald, D. J. Donalson, and J. J. Sloan, Chem. Phys. Lett. **95,** 183 (1983).

[56] J. E. Butler, G. M. Jursich, I. A. Watson, and J. R. Wiesenfeld, J. Chem. Phys. **84,** 5365 (1986).
[57] R. J. Buss, P. Casavecchia, T. Hirooka, S. J. Sibener, and Y. T. Lee, Chem. Phys. Lett. **82,** 386 (1981).
[58] K. Tsukiyama, B. Katz, and R. Bersohn, J. Chem. Phys. **83,** 2889 (1985).
[59] Y. Matsumi, K. Tonokura, M. Kawasaki, and H. L. Kim, J. Phys. Chem. **96,** 10622 (1992).
[60] M. S. Fritzcharles, and G. C. Schatz, J. Phys. Chem. **90,** 3634 (1986).
[61] L. J. Dunne, Chem. Phys. Lett. **158,** 535 (1989).
[62] A. J. Alexander, F. J. Aoiz, M. Brouard, and J. P. Simons, Chem. Phys. Lett. **256,** 561 (1996).
[63] K. Badenhoop, K. Koizumi, and G. C. Schatz, J. Chem. Phys. **91,** 142 (1989).
[64] T. Peng, D. M. Zhang, J. Z. H. Zhang, and R. Schinke, Chem. Phys. Lett. **248,** 37 (1996).
[65] M. Alagia, N. Balucani, L. Cartechini, P. Casavecchia, E. H. van Kleef, G. G. Volpi, P. J. Kuntz, and J. J. Sloan, J. Chem. Phys. **108,** 6698 (1998).
[66] M. Ahmed, D. S. Peterka, and A. G. Suits, Chem. Phys. Lett. **310,** 372 (1999).
[67] D.-C. Che and K. Liu, J. Chem. Phys. **103,** 5164 (1995).
[68] Y.-T. Hsu and K. Liu, J. Chem. Phys. **107,** 1664 (1997).
[69] Y.-T. Hsu, J. H. Wang, and K. Liu, J. Chem. Phys. **107,** 2351 (1997).
[70] Y.-T. Hsu, K. Liu, L. A. Pederson, and G. C. Schatz, J. Chem. Phys. **111,** 7921 (1999).
[71] Y.-T. Hsu, K. Liu, L. A. Pederson, and G. C. Schatz, J. Chem. Phys. **111,** 7931 (1999).
[72] D. W. Hwang, X. F. Yang, and X. Yang, J. Chem. Phys. **110,** 4119 (1999).
[73] S. K. Gray, G. G. Balint-Kurti, G. C. Schatz, J. J. Lin, X. Liu, S. Harich, and X. Yang, J. Chem. Phys. **113,** 7330 (2000).
[74] X. Liu, C. C. Wang, S. A. Harich, and X. Yang, Phys. Rev. Lett. **89,** 133201 (2002).
[75] X. Liu, J. J. Lin, S. A. Harich, and X. Yang, Phys. Rev. Lett. **86,** 408 (2001).
[76] X. Liu, J. J. Lin, S. A. Harich, and X. Yang, J. Chem. Phys. **113,** 1325 (2000).
[77] S. A. Buntin, C. F. Giese, and W. R. Gentry, J. Chem. Phys. **87,** 1443 (1987).
[78] D. A. Kliner, D. E. Adelman, and R. N. Zare, J. Chem. Phys. **95,** 1648 (1991).
[79] T. N. Kitsopoulos, M. A. Buntine, D. P. Balwin, R. N. Zare, and D. W. Chandler, Science **260,** 1605 (1993).
[80] J. Z. H. Zhang and W. H. Miller, J. Chem. Phys. **91,** 1528 (1991).
[81] M. Zhao, D. G. Truhlar, D.W. Schwenke, and D. J. Kouri, J. Phys. Chem. **94,** 7074 (1990).
[82] M. Zhao, M. Mladenovic, D. G. Truhlar, D. W. Schwenke, O. Sharafeddin, Y. Sun, and D. J. Kouri, J. Chem. Phys. **91,** 5302 (1989).
[83] M. J. D'Mello, D. E. Manolopoulos, and R. E. Wyatt, J. Chem. Phys. **94,** 5985 (1991).
[84] R. T. Pack and G. A. Parker, J. Chem. Phys. **87,** 3888 (1987).
[85] D. M. Skouteris, J. F. Castillo, and D. E. Manolopoulos, Comput. Phys. Commun. **133,** 128 (2000).
[86] S. D. Chao and R. T. Skodje, Chem. Phys. Lett. **336,** 364 (2001).
[87] X. Liu, J. J. Lin, S. A. Harich, G. C. Schatz, and X. Yang, Science **289,** 1536 (2000).
[88] X. Liu, J. J. Lin, S. A. Harich, and X. Yang, Phys. Rev. Lett. **86,** 408 (2001).
[89] S. A. Harich, D. Dai, X. Yang, S. D. Chao, and R. T. Skodje, J. Chem. Phys. **116,** 4769 (2002).
[90] K. D. Rinnen, D. A. V. Kliner, M. A. Buntine, and R. N. Zare, Chem. Phys. Lett. **169,** 365 (1990).
[91] S. A. Harich, D. Dai, C. C. Wang, X. Yang, S. D. Chao, and R. T. Skodje, Nature **419,** 281 (2002).
[92] S. A. Harich, D. Dai, C. C. Wang, X. Yang, S. D. Chao, and R. T. Skodje, J. Chem. Phys. **117,** 8341 (2002).
[93] A. I. Boothroyd, W. J. Keogh, P. G. Martin, and M. R. Peterson, J. Chem. Phys. **104,** 7139 (1996).
[94] M. L. Goldberger, K. M. Watson, *Collision Theory* (Wiley, New York, 1964).
[95] S. C. Althorpe, F. Fernandez-Alonso, B. D. Bean, J. D. Ayers, A. E. Pemerantz, R. N. Zare, and E. Wrede, Nature **416,** 67 (2002); F. Fernández-Alonso, B. D. Bean, J. D. Ayers, A. E. Pomerantz, R. N. Zare, L. Bañares, and F. J. Aoiz, Ang. Chemie. **39,** 2748 (2000).
[96] S. A. Cuccaro, P. G. Hipes, and A. Kuppermann, Chem. Phys. Lett. **157,** 440 (1989).
[97] R. T. Skodje, R. Sadeghi, H. Koppel, and J. L. Krause, J. Chem. Phys. **101,** 1725 (1994).
[98] D. C. Chatfield, S. L. Mielke, T. C. Allison, and D. G. Truhlar, J. Chem. Phys. **112,** 8387 (2000).
[99] R. Sadeghi and R. T. Skodje, J. Chem. Phys. **102,** 193 (1995).
[100] D. C. Chatfield, R. S. Friedman, D. W. Schwenke, and D. G. Truhlar, J. Phys. Chem. **96,** 2414 (1992).
[101] D. E. Manolopoulos, K. Stark, H.-J. Werner, D. W. Arnold, S. E. Bradforth, and D. M. Neumark, Science **262,** 1852 (1993).
[102] E. R. Lovejoy, S. K. Kim, and C. B. Moore, Science **256,** 1541 (1992); S. K. Kim, E. R. Lovejoy, and C. B. Moore, J. Chem. Phys. **102,** 3202 (1995).
[103] W. H. Miller, N. C. Handy, and J. E. Adams, J. Chem. Phys. **72,** 99 (1980).
[104] R. T. Skodje, D. Skouteris, D. E. Manolopoulos, S.-H. Lee, F. Dong, and K. Liu, Phys. Rev. Lett. **85,** 1206 (2000).
[105] D. M. Neumark, A. M. Wodtke, G. N. Robinson, C. C. Hayden, and Y. T. Lee, Phys. Rev. Lett. **53,** 226 (1984).

[106] T. N. Kitsopoulos, M. A. Buntine, D. P. Baldwin, R. N. Zare, and D. W. Chandler, Science **260,** 1605 (1993).
[107] M. J. D'Mello, D. E. Manolopoulos, and R. E. Wyatt, J. Chem. Phys. **94,** 5985 (1991).
[108] Y. S. M. Wu and A. Kuppermann, Chem. Phys. Lett. **235,** 105 (1995).
[109] B. K. Kendrick, J. Chem. Phys. **114,** 8796 (2001).
[110] D. Dai, C. C. Wang, S. A. Harich, X. Wang, X. Yang, S. D. Chao, and R. T. Skodje, Science **300,** 1730 (2003).
[111] L. Schnieder, K. Seekamp-Rahn, F. Liedeker, H. Steuwe, and K. H. Welge, Faraday Discuss. **91,** 259 (1991).
[112] A. I. Boothroyd, W. J. Keogh, P. G. Martin, and M. R. Peterson, J. Chem. Phys. **104,** 7139 (1996).
[113] R. T. Pack and G. A. Parker, J. Chem. Phys. **87,** 3888 (1987).
[114] G. C. Schatz, Chem. Phys. Lett. **150,** 92 (1988).
[115] J. M. Launay and M. Le Dourneuf, Chem. Phys. Lett. **163,** 178 (1989).
[116] D. M. Skouteris, J. F. Castillo, and D. E. Manolopolous, Comput. Phys. Commun. **113,** 128 (2000).
[117] S. D. Chao and R. T. Skodje, Chem. Phys. Lett. **336,** 364 (2001).
[118] W. H. Miller, Ann. Rev. Phys. Chem. **41,** 245 (1990).
[119] R. Sadeghi and R. T. Skodje, J. Chem. Phys. **102,** 193 (1995); R. T. Skodje, R. Sadeghi, H. Koppel, and J. L. Krause, J. Chem. Phys. **101,** 1725 (1994).
[120] M. S. Child, *Molecular Collision Theory* (Dover, New York, 1996), p. 167.